TEMPORAL VARIATIONS IN SLIP-RATE ALONG THE LONE MOUNTAIN FAULT, WESTERN NEVADA

A Thesis
Presented to
The Academic Faculty

by

Jeffrey S. Hoeft

In Partial Fulfillment
of the Requirements for the Degree
Master of Science in the
School of Earth and Atmospheric Sciences

Georgia Institute of Technology
May 2010

TEMPORAL VARIATIONS IN SLIP-RATE ALONG THE LONE MOUNTAIN FAULT, WESTERN NEVADA

Approved by:

Dr. Kurt Frankel, Advisor
School of Earth and Atmospheric Sciences
Georgia Institute of Technology

Dr. Andrew Newman
School of Earth and Atmospheric Sciences
Georgia Institute of Technology

Dr. Zhigang Peng
School of Earth and Atmospheric Sciences
Georgia Institute of Technology

Date Approved: April 02, 2010

ACKNOWLEDGEMENTS

Five years ago, when I was finishing my bachelor's degree at USC and Kurt was still a PhD candidate, I made an off-the-cuff remark saying that if he got a faculty position in the near future, I would come and be his first student. True to my word, when Kurt started at Georgia Tech, I made plans to come work with him, and I am very glad I did. While at Tech, Kurt has helped foster my intellect, continued to hone my skills as a scientist, and been an effective advisor, making sure I finished my degree on-time. I am more than thankful to have had the opportunity to work with Kurt, and appreciate all the advice and encouragement he has provided to me over the years. In addition, there are several other people who I would like to recognize for their role in bringing this project to fruition. I thank Jaime Convers and Zach Lifton for their assistance in the field; Tina Colbert for her aid with TCN sample preparation; and Dylan Rood at Lawrence Livermore National Lab for his assistance with TCN sample analysis. Additionally, my thesis reading committee of Andrew Newman and Zhigang Peng provided thoughtful reviews that helped improve the manuscript.

On the more personal side, I would like to thank Angela Fritz for her continued support and friendship; Justin Burns, Jake Leech and Morris Jones who provided the occasional distraction to catch a beer after a long day at the office; and my co-workers from William Lettis and Associates who encouraged me to go back to school to get my master's degree - I look forward to rejoining them this summer. I am also very thankful for my parents and family who are ever supportive and helped me get through the stressful parts of my

thesis. Additionally, I would like to thank my Great Uncle Bernard who sparked my interest in Geology and helped me realize I wanted to pursue it as a career.

This research was funded by National Science Foundation grants EAR-0929960 and EAR-0948570, the Geological Society of America, and the Georgia Institute of Technology School of Earth and Atmospheric Sciences.

TABLE OF CONTENTS

LIST OF TABLES

LIST OF FIGURES

LIST OF ABBREVIATIONS

DVFLV	Death Valley-Fish Lake Valley
ECSZ	eastern California shear zone
SPLM	Silver Peak-Lone Mountain
TCN	terrestrial cosmogenic nuclide

SUMMARY

Late Pleistocene displacement along the Lone Mountain fault suggests the Silver Peak-Lone Mountain (SPLM) extensional complex is an important structure in accommodating and transferring strain within the eastern California shear zone (ECSZ) and Walker Lane. Using geologic and geomorphic mapping, differential global positioning system surveys, and terrestrial cosmogenic nuclide (TCN) geochronology, we determined rates of extension across the Lone Mountain fault in western Nevada. The Lone Mountain fault is the northeastern component of the SPLM extensional complex, and is characterized by a series of down-to-the-northwest normal faults that offset the northwestern Lone Mountain and Weepah Hills piedmonts. We mapped eight distinct alluvial fan deposits and dated three of the surfaces using ^{10}Be TCN geochronology, yielding ages of 16.5 ± 1.2 ka, 92.3 ± 8.6 ka, and 142.2 ± 19.5 ka for the Q3b, Q2c, and Q2b deposits, respectively. The ages were combined with scarp profile measurements across the displaced fans to obtain minimum rates of extension; the Q2b and Q2c surfaces yield an extension rate between 0.1 ± 0.1 and 0.2 ± 01 mm/yr and the Q3b surface yields a rate of 0.2 ± 0.1 to 0.4 ± 0.1 mm/yr, depending on the dip of the fault. Active extension on the Lone Mountain fault suggests that it helps partition strain off of the major strike-slip faults in the northern ECSZ and transfers deformation around the Mina Deflection northward into the Walker Lane. Combining our results with estimates from other faults accommodating dextral shear in the northern ECSZ reveals an apparent discrepancy between short- and long-term rates of strain accumulation and release. If strain rates have remained constant since the late Pleistocene, this could reflect transient strain accumulation, similar to the Mojave segment of the ECSZ. However, our data also suggest an increase in strain rates between

~92 ka and ~17 ka, and possibly to present day, which may also help explain the mismatch between long- and short-term rates of deformation in the region.

CHAPTER 1. INTRODUCTION

Understanding temporal and spatial constancy of strain accumulation and release rates is a critical component to deciphering how deformation is accommodated in the lithosphere. For most plate boundaries, comparisons of short-term (decadal) geodetic and long-term (e.g., 10^3-10^6 years) geologic plate motion data indicate that rates of strain storage and release are relatively constant over a wide variety of time scales (e.g., Sella et al., 2002). The Pacific-North America plate boundary has been the subject of extensive investigation and different sections of the plate boundary record different spatial and temporal patterns of strain accumulation and release (e.g., Lee et al., 2001, 2006, 2009a,b; Kylander-Clark et al., 2005; Kirby et al., 2006, 2008; Le et al., 2006; Oskin et al., 2008; Andrew and Walker, 2009; Frankel et al., 2009a,b; Ganev et al., 2010). Differential plate motion across the Pacific North America boundary is primarily accommodated along the dextral San Andreas fault system, and much of the remainder of motion is thought to be taken up by structures in the eastern California shear zone (ECSZ) and Walker Lane belt (e.g., Burchfiel et al., 1979; Brogan et al., 1991; Reheis and Sawyer, 1996, 1997; Berry, 1997; Hearn and Humphreys, 1998; Dixon et al., 2000; Oldow et al., 2001; Petronis, 2005; Kirby et al., 2006; Frankel et al., 2007a, b; Lee et al., 2009b).

The transtensional ECSZ and Walker Lane accommodate ~20% of the cumulative Pacific North America plate boundary deformation, and recent geodetic studies show that across the ECSZ, strain is accumulating at a rate of 9-14 mm/yr over the past ~20 years (Fig. 1; e.g., Stewart, 1988; Dokka and Travis, 1990; Humphreys and Weldon, 1994; Hearn and Humphreys, 1998; Thatcher et al., 1999; Dixon et al., 2000, 2003; Flesch et al., 2000;

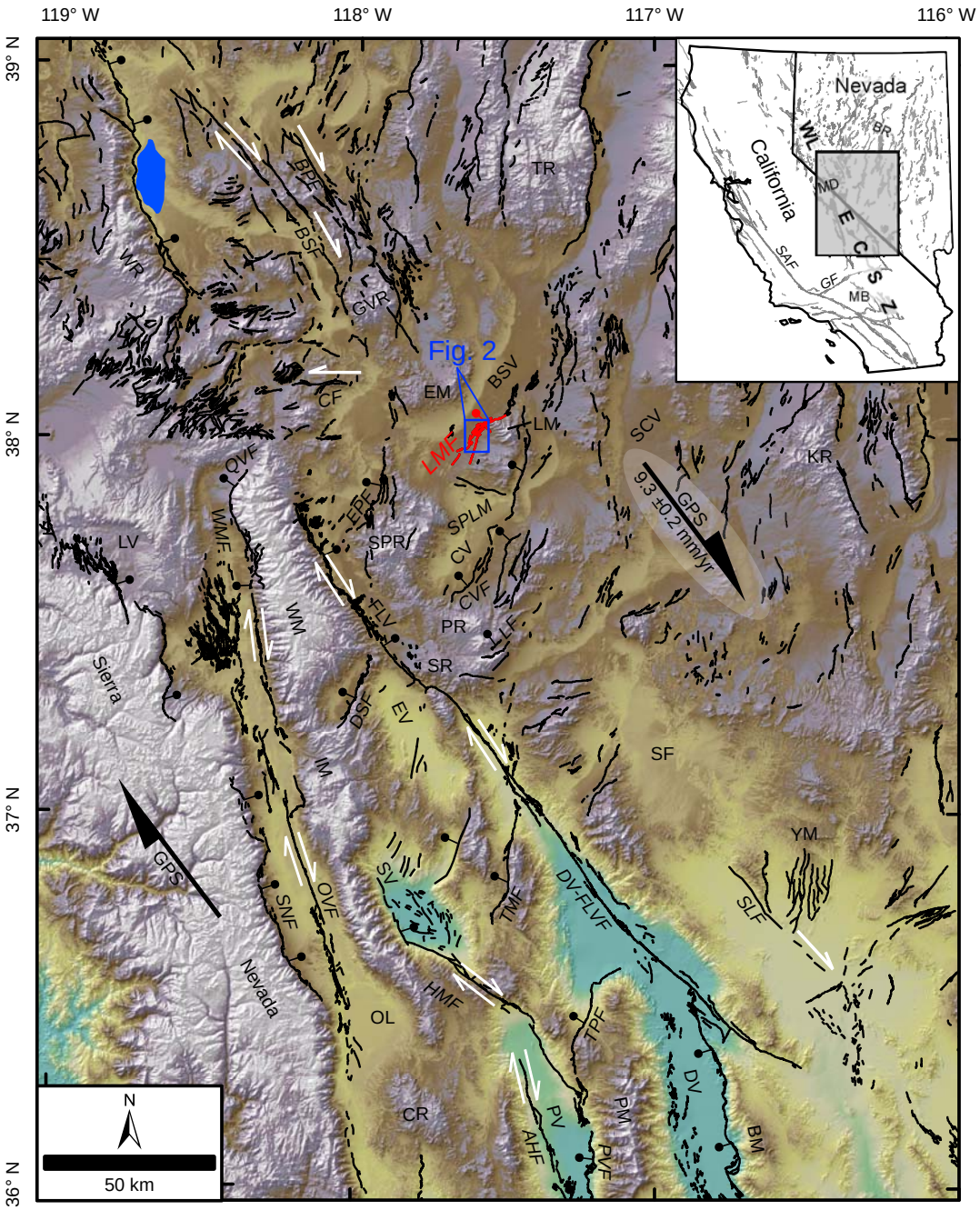

Figure 1. Index map of the Walker Lane region showing topography and major strike-slip and normal faults. Faults are labled in italics, and are from the USGS Quaternary fault and fold database. AHF - Ash Hill Fault; BM - Black Mountains, BPF - Bettles Well-Petrified Springs Fault, BR - Basin and Range, BSF - Benton Springs Fault, BSV - Big Smoky Valley, CF - Coaldale Fault, CV - Clayton Valley, CVF - Clayton Valley Fault, CR - Coso Range, DSF - Deep Springs fault, DV - Death Valley, DV-FLVF - Death Valley-Fish Lake Valley fault, ECSZ - eastern California shear zone, EPF - Emigrant Peak fault, EV - Eureka Valley, FLV - Fish Lake Valley, GF - Garlock fault, GVR - Gabbs Valley Range, HMF - Hunter Mountain-Saline Valley fault, IM - Inyo Mountains, KR - Kawich Range, LF - Lida Fault, LM - Lone Mountain, LM - Lone Mountain Fault, LV - Long Valley Caldera, MB - Mojave Block, MD - Mina Deflection, NV - Nevada, OL - Owens Lake, OVF - Owens Valley fault, PM - Panamint Mountains, PR - Palmetto Range, PV - Panamint Valley, PVF - Panamint Valley Fault, QVF - Queen Valley Fault, SAF - San Andreas Fault, SCV - Stone Cabin Valley, SF - Sarcobotus Flat, SLF - Stateline fault, SR - Sylvania Range, SNF - Sierra Nevada fault, SPLM - Silver Peak-Lone Mountain extensional complex, SPR - Silver Peak Range, SV - Saline Valley, TMF - Tin Mountain fault, TPF - Townes Pass fault, TR - Toiyabe Range, WH - Weepah Hills, WL - Walker Lane, WM - White Mountains, WMF - White Mountains fault, WR - Wassuk Range, YM - Yucca Mountain, The Lone Mountain fault zone is highlighted in red, the areal extent of Figure 2 is shown in blue, and white arrows show kinematic motion for select faults. Regionally averaged GPS-derived tectonic motion from Bennett et al. (2003).

McClusky et al., 2001; Miller et al., 2001; Bennett et al., 2003). However, at different latitudes in the ECSZ, previous work documents a match between long-term geologic and short-term geodetic rates in some regions (Sieh and Jahns, 1984; McClusky et al., 2000; Argus and Gordon, 2001; Bennett et al., 2003; Lee and Stokli, 2006; Frankel et al., 2007a, in review; Owen et al., in review), while other areas are characterized by apparent transient strain accumulation (Peltzer et al., 2001; Oskin and Iriondo, 2004; Oskin et al., 2007, 2008; Frankel et al., 2007 b).

Across the southern portion of the ECSZ, in the Mojave Desert, the geologic record of right-lateral slip shows an apparent disparity with the geodetic strain data (Oskin et al., 2008). At this latitude, a summation of dextral slip since the late Pleistocene provides a cumulative right-lateral deformation rate of ≤ 6.2 ± 1.9 mm/yr, representing approximately half of the short-term rate of 12.2 ± 2 mm/yr (Dokka, 1983; Dokka and Travis, 1990; Sauber et al., 1994; Oskin et al., 2008). However, north of the Garlock fault, at latitude ~37ºN, the late Pleistocene and short-term strain rate agree; a summation of slip rates across the main right-lateral fault structures show a cumulative strain release rate of ~9-10 mm/yr which is comparable to the region-wide 9.3 ± 0.2 mm/yr of dextral shear determined with GPS data (Lee et al., 2009b; Bennett et al., 2003; Frankel et al., 2007a).

Geodetic studies suggest a majority of differential plate motion between latitude 37°N and 38°N is accommodated as right-lateral shear oriented ~323° ± 2° at a rate of 9.3 ± 0.2 mm/yr, and the remainder as extension with ~1 mm/yr accumulating normal to the right-

lateral motion (e.g., Savage et al., 2001; Bennett et al., 2003; Wesnousky, 2005a). The two major faults at this latitude are the north-northwest-trending dextral-oblique White Mountain and Death Valley-Fish Lake Valley (DVFLV) faults (Fig 1). A summation of slip-rates across the Fish Lake Valley and White Mountains faults at latitude ~37.5ºN suggest that <3.5 mm/yr of the region-wide rate of right-lateral shear is accommodated on these structures (Frankel et al., 2007b; Kirby et al., 2006; Bennett et al., 2003). Geodetic models predict that right-lateral shear rates should increase toward the northern end of the DVFLV fault, but geologic data indicate the opposite (Dixon et al., 2003; Frankel et al., 2007b). Together, these observations suggest that only ~1/3 of the short-term rate of dextral shear in this region can be accounted for in the geologic record on strike-slip faults.

At the northern termination of the White Mountains and Fish Lake Valley faults there is an eastward (right) step and the belt of active faults extends an additional ~80 km to the east before continuing northward into the central Walker Lane (Nielsen, 1965; Stewart, 1985, 1988; Oldow et al., 2001). This eastward step, known as the Mina Deflection, connects the predominantly dextral northern ECSZ and central Walker Lane fault systems. Lee et al. (2009a) show that strain is transferred from the White Mountain fault into the Mina Deflection via the Queen Valley fault; the Emigrant Peak fault also helps transition strain away from the DVFLV fault zone north and east to the Mina Deflection and central Walker Lane (e.g., Reheis and Sawyer, 1997; Ganev et al., 2010). Faults within the Mina Deflection are predominantly east-west trending and are thought to

accommodate left-lateral strike-slip motion and clockwise block rotation (Stewart, 1985; Cashman and Fontaine, 2000; Faulds et al., 2005; Wesnousky, 2005b).

In this study, we address the apparent discrepancy between short- and long-term rates of deformation at the eastern California shear zone-Walker Lane transition. We investigate the Lone Mountain fault, a prominent down-to-the-northwest normal fault within the Silver Peak-Lone Mountain (SPLM) extensional complex located to the south of the Mina deflection and east of the DVFLV and Emigrant Peak fault systems (Fig. 1). We document the amount of extension on fault scarps cutting alluvial fans, and calculate late Pleistocene extension rates for this fault by dating offset alluvial fans using ^{10}Be terrestrial cosmogenic nuclide geochronology. Our results show temporal variation in strain release rates in the late Pleistocene along the Lone Mountain fault, and have important implications for understanding the dynamics and evolution of the Pacific-North America plate boundary deformation within the ECSZ-Walker Lane.

CHAPTER 2. GEOLOGIC SETTING

Deciphering the ECSZ-Walker Lane fault transfer system requires interpretation of earlier structures as well as currently active faults. Transform displacement initiated along the Pacific-North America plate boundary and northeast-southwest extension in the Basin and Range was underway by the Early Miocene (Atwater, 1970; Atwater and Molnar; 1973; Snyder et al., 1976; Burchfiel, 1979). As the transform plate boundary evolved, some faults along the western margin of the Basin and Range began accommodating part of the transform motion, now manifest as the ECSZ and Walker Lane (Burchfiel, 1979; Stewart, 1988). By Late Miocene to early Pliocene time, the ECSZ and Walker Lane played a significant role in plate boundary dynamics, and displacement was primarily taken up on a series of right-stepping, northwest-southeast oriented, right-lateral faults (Atwater, 1970; Atwater and Stock, 1998; Stokli et al., 2003; Kylander-Clark et al., 2005; Bartley et al., 2008).

During the Late-Miocene, the northwest-oriented SPLM extensional complex accommodated the structural eastward step between the north end of the DVFLV fault system and the Benton Springs and Bettles Well-Petrified Springs faults of the central Walker Lane (Stewart, 1988; Oldow et al., 1994, 2001, 2008; Oldow, 2003). This region of extension was bounded to the north by a structural boundary in the Excelsior Mountains and to the south by the Sylvania and Palmetto Ranges (Fig. 1; Oldow et al., 2008). The extensional complex accommodated motion on a low-angle detachment, the core of which is exposed today in Lone Mountain, the Weepah Hills, and Silver Peak (Kirsch, 1971). The lower plate exhibits highly metamorphosed amphibolite facies rocks

that record a complex history of metamorphism and intrusive deformation (Oldow, 2008). Based on paleomagnetic analysis of volcanic rocks, Petronis et al. (2002, 2007, and 2009) suggest that Silver Peak and Lone Mountain rotated between 20° and 30° since the Oligocene. It is thought that this gradual rotation throughout the Miocene helped lock these detachment faults by the middle Pliocene, shifting the locus of strain transfer to the Mina deflection further to the west and north (Oldow et al., 2008, 2009).

Today, the Silver Peak-Lone Mountain extensional complex is a series of northeast-striking down-to-the-northwest normal fault bounded basins, including the Lone Mountain, Clayton Valley, and Lida faults (Fig 1). The Lone Mountain fault is located at the northeast end of this zone along the southern edge of Big Smoky Valley, and expressed as a series of prominent synthetic and antithetic scarps cutting across the northwest Weepah Hills and Lone Mountain piedmonts (Dohrenwend et al., 1992; dePolo, 2008). We mapped and dated these offset fans to determine late Pleistocene rates of extension across the Lone Mountain fault.

2.1 Alluvial Fan Stratigiraphy

Geologic mapping of Quaternary alluvial fan deposits and fault related features was completed at a scale of 1:10,000 using color orthorectified aerial photographs (Figs. 2, 3, and 4; Appendix A). Alluvial fan deposits were identified and correlated across the field area based on standard criteria such as surface morphology, including amplitude of bar and swale, soil development, desert pavement development, rubification and varnish hues, height above active channels, and degree of fan dissection (e.g., Bull, 1968, 1991;

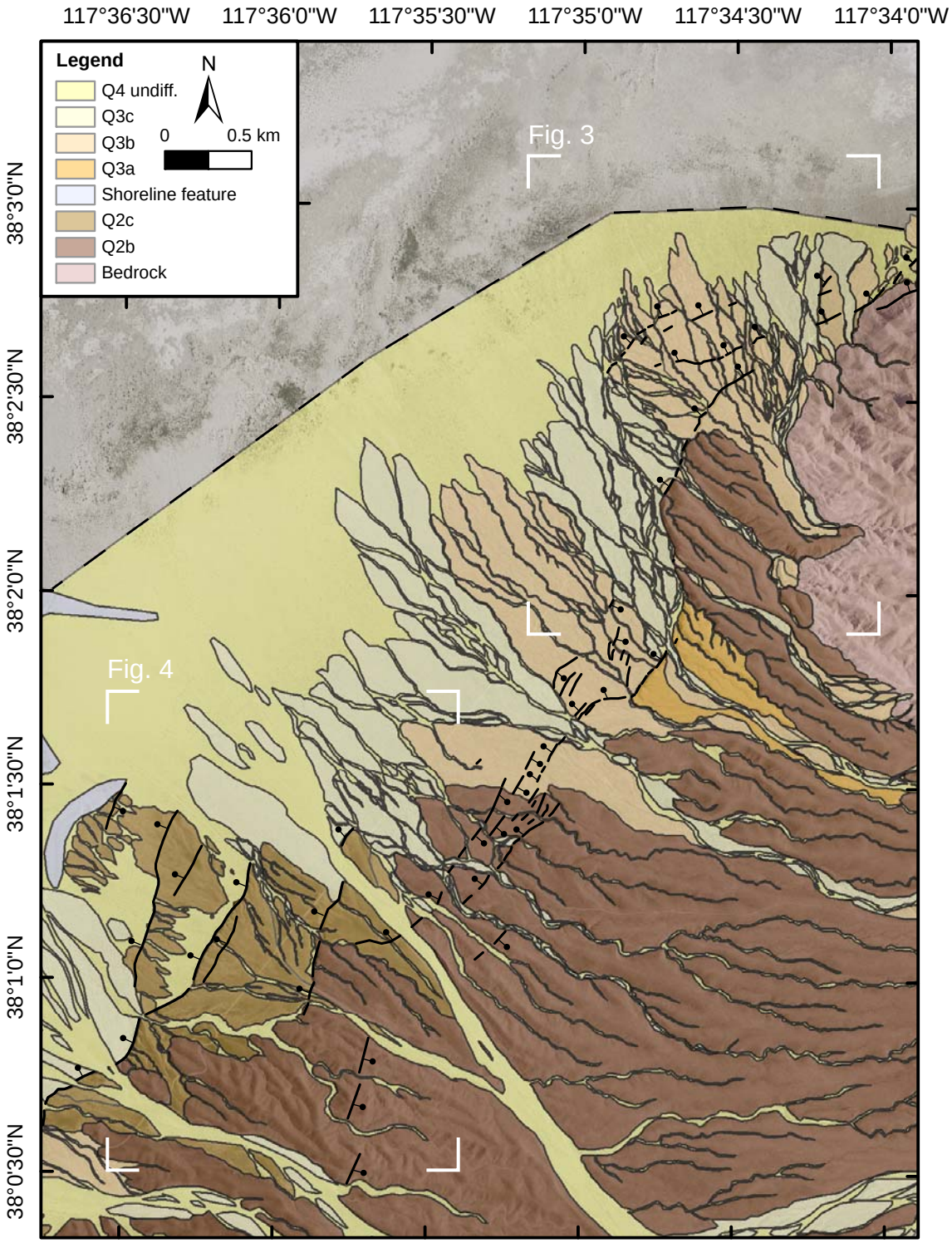

Figure 2. Detailed map showing results of geomorphic and geologic mapping along the part of the Lone Mountain fault. Fault strands are shown as solid black lines with tick-marks indicating direction of motion. The extent of Figures 3 and 4 are shown by white corners.

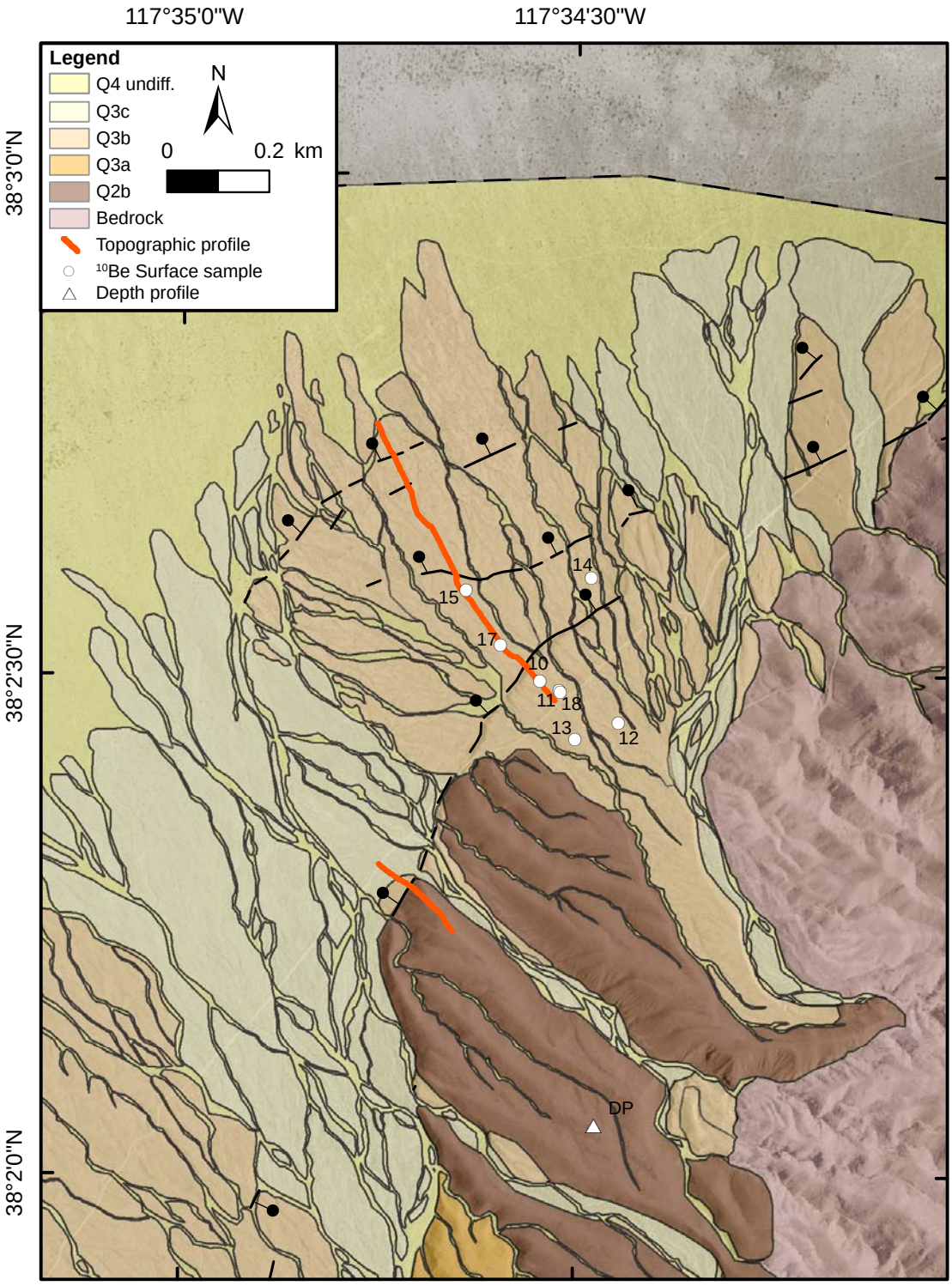

Figure 3. Detailed geologic map showing locations of topographic profiles, location of Q3b surface samples, and location of Q2b depth profile.

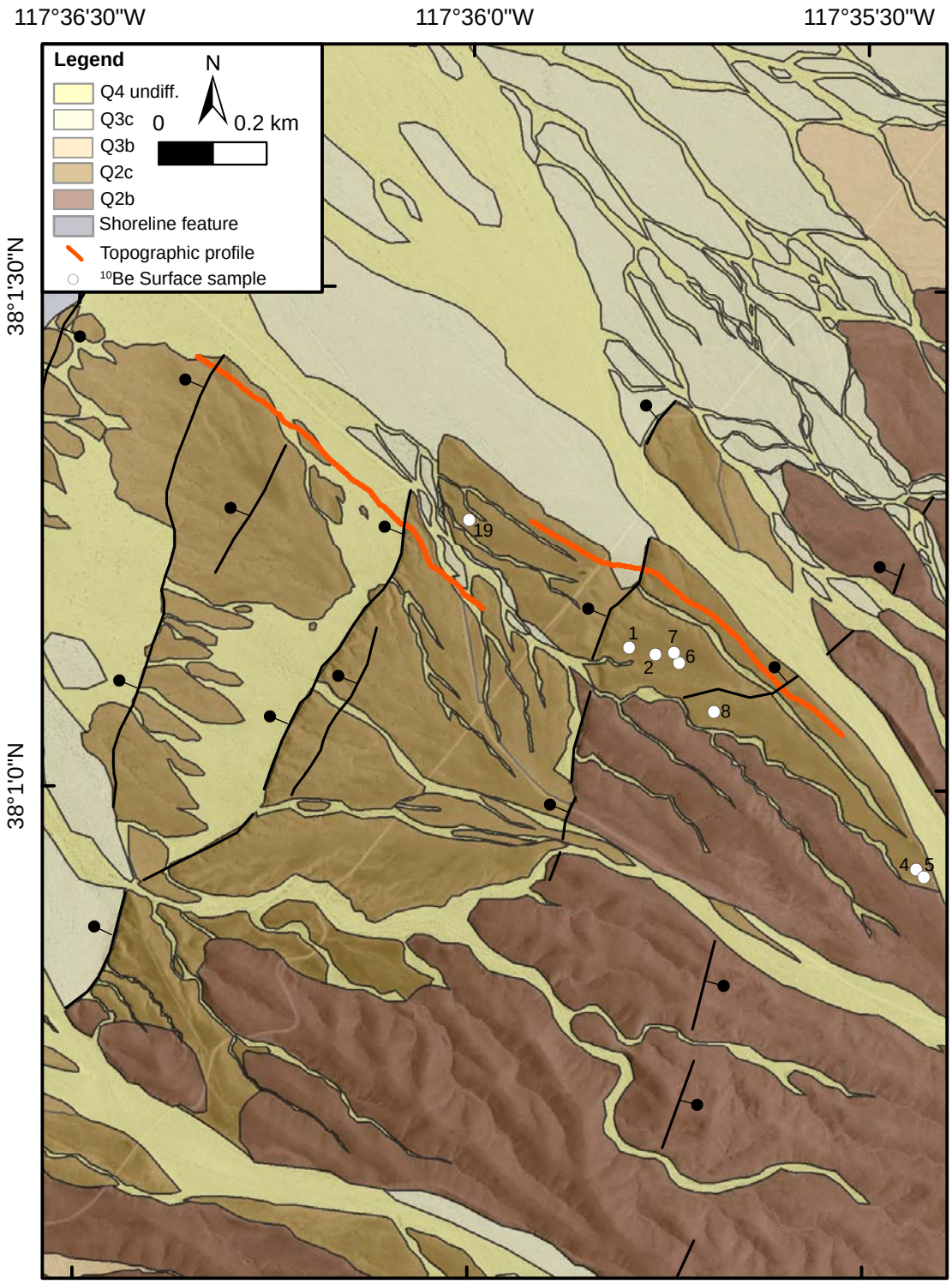

Figure 4. Detailed geologic map showing locations of Q2c topographic profile, and location of Q2c surface samples.

Ritter et al., 1993; Frankel and Dolan, 2007). The alluvial fan deposits found in Big Smoky Valley are consistent with the regional desert piedmont surfaces (Q2, Q3, and Q4) correlated throughout southwestern North America and described in detail by Bull (1968; 1991).

The alluvial fan deposits identified along the northwest Lone Mountain piedmont are consistent with the previously-defined North American lithostratigraphic framework (Bull, 1991), and include eight distinctive units: Q4b, Q4a, Q3c, Q3b, Q3a, Q2c, Q2b, and Q2a. The active channels are represented by Q4b, and occupy the lowest topographic position in the landscape. All older surfaces are progressively higher in elevation relative to Q4b; a brief description of each is included in Table 1. Although we identified and correlated eight alluvial fan surfaces, here we focus on three of them, Q3b, Q2c, and Q2b, (Fig.5), because these surfaces preserve the best expression of late Pleistocene deformation.

2.2 Late Pleistocene Fault Displacement

The Lone Mountain fault is characterized by numerous down-to-the-northwest and several antithetic down-to-the-southeast fault strands striking between 210° and 235° that prominently displace the Q3b, Q2c, and Q2b alluvial fan deposits. Fault scarps were surveyed with differential Global Positioning System (GPS) equipment to document the amount of vertical separation in the various fan units. A total of 83 profiles were collected using a Trimble GeoXH GPS unit to measure fault perpendicular topographic profiles, and post-processing of data resulted in decimeter accuracy (Appendix B).

Table 1. Characteristics of Quaternary alluvial fan surfaces along the Lone Mountain and Weepah Hills piedmont

Fan Deposit	Surface Morphology	Soil Description
Q4 undifferentiated	Active stream channel and most recently abandoned channel. No pavement development or soil development. Surfaces are up to 1.5 m above active channel. Youngest surface in field area.	No soil development.
Q3c	Undissected,bouldery bar-and-swale pavements 0 to 2 m above stream channels. Small patches of moderate to immature desert pavement developed, with immature to moderate rubification on clasts.	Immature soil development with <5 cm thick Av horizon, and <15 cm thick B horizon. Slight salt and carbonate accumulations (stage 1).
Q3b	Moderate to intermediate desert pavement, with subdued bar and swale relief of 0.25 to 0.75 m. Surfaces are 0.5 to1.5 m above the active channel, and surface clasts are generally interlocking with moderate rubification and varnish, varying in size from pebbles to moderately sized cobbles.	Immature soil development shows a ~10-cm-thick Av horizon, and a ~20-cm-thick B horizon with small amounts of salt and carbonate accumulations (stage I+) and moderate clay film development.
Q3a	Undissected,bouldery bar-and-swale pavements 0 to >3 m above stream channels	
Q2c	Well-developed mature desert pavement, with negligible bar and swale and slight dissection. Surfaces are 1 to 3 m above the active channel, and clasts are interlocking, dominated by pebbles with occasional cobbles. The tops of surface clasts have distinctive well-developed varnish, while clast undersides are highly rubified.	A 30- to 50-cm soil is developed. The soil is characterized by a 10- to 20-cm-thick Av horizon with clay film accumulations in the lower half; a distinctive middle Bt horizon with clay and moderate carbonate and salt development; and a lower Bk horizon with moderate carbonate accumulations (Stage III).
Q2b	The Q2b surface is >3 m above the active channel and characterized by smooth pavements, rounded hillslopes, moderate dissection, and subdued bar and swale morphology of <0.25 m. Clasts are interlocking, with pebbles to cobbles, and occasional boulders are exposed at the surface. Varnish and rubification development are generally moderate to high, and is underlain by a well-developed soil.	Well developed soils have a 10- to 20-cm-thick Av horizon, a 20- to 50-cm-thick Bt horizon, and a 50- to100-cm-thick Bk horizon with Stage III carbonate development.
Q2a	Disected remnants of pavements 4 to 10 m above stream channels	

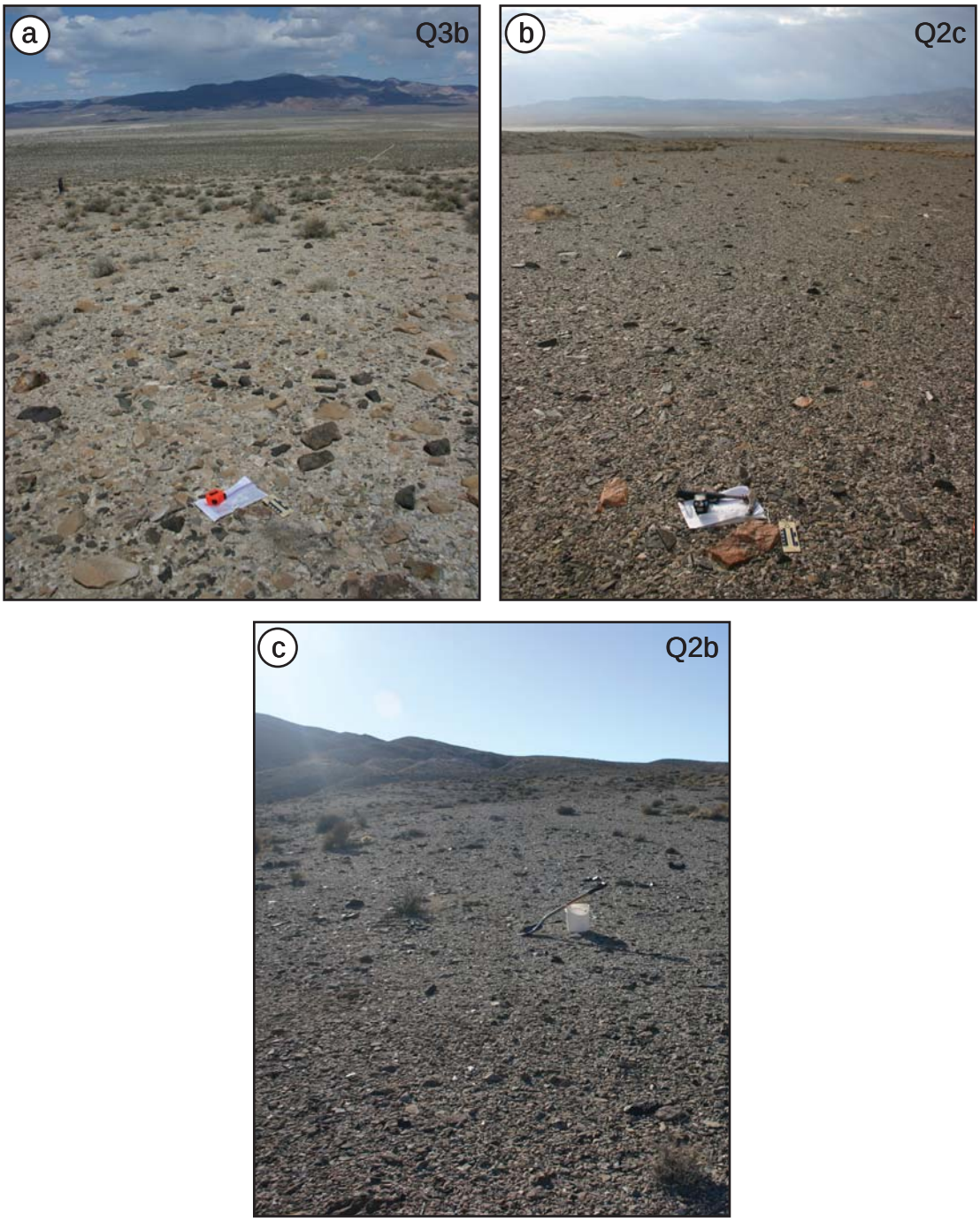

Figure 5. Photographs showing alluvial fan surfaces where cosmogenic radionuclide samples were collected. Surface samples were collected from Q3b (a), and Q2c (b), while depth profile samples were collected from Q2b (c). Locations of each sampling surface are noted on Figures 3 and 4. See text and Table 1 for more detailed descriptions of each fan surface.

Following a surface rupturing earthquake, normal fault scarps typically have free faces that rapidly reach a stable angle of repose. Scarp slopes are then thought to degrade into the landscape via diffusive processes, including rain splash and soil creep (e.g., Hanks et al., 1984; Arrowsmith et al., 1998; Bucknam and Anderson, 1979; Wallace, 1977). We measured scarp height at the scarp center-point, as illustrated in Figure 6, and also measured the scarp-angle (Appendix C). Errors associated with these measurements include variations in surface roughness (e.g., amplitude of bar and swale; ≤ 25 cm), and uncertainty with GPS equipment measurements, but do not reflect the possibility for off-scarp deformation.

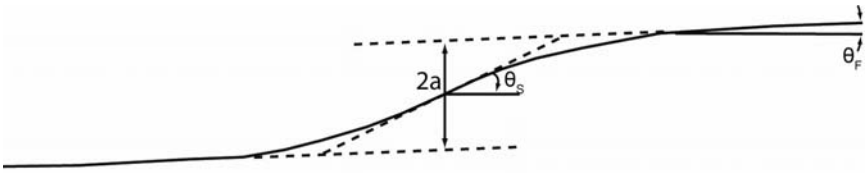

Figure 6. Geometry of an idealized fault scarp after Hanks et al. (1984). 2a represents the scarp offset distance; θ_S is the scarp slope angle; and θ_F is the far field slope angle.

Accurately determining the total vertical offset across the Q3b, Q2c and Q2b alluvial fan surfaces is critical to determining extension rates. To document the total vertical displacement of the Q3b, Q2c, and Q2b alluvial fan surfaces, locations with well-preserved fan surfaces and fault scarps with the largest surface displacement were selected. Figures 3 and 4 show aerial views of profile locations, and Figures 7, 8, and 9c show the resulting topographic profiles with cumulative vertical offset. Figure 10 shows photographs of scarps displacing the different alluvial fan surfaces. The Q3b topographic profile records a cumulative vertical offset of 6.0 ± 1.2 m with a maximum single scarp height of 4.0 ± 0.3 m (Figs. 7 and 9a). The Q2c topographic profile yields a total vertical offset of 14.3 ± 1.2 m and a maximum single scarp height of 7.2 ± 0.3 m (figs. 8, and 9b).

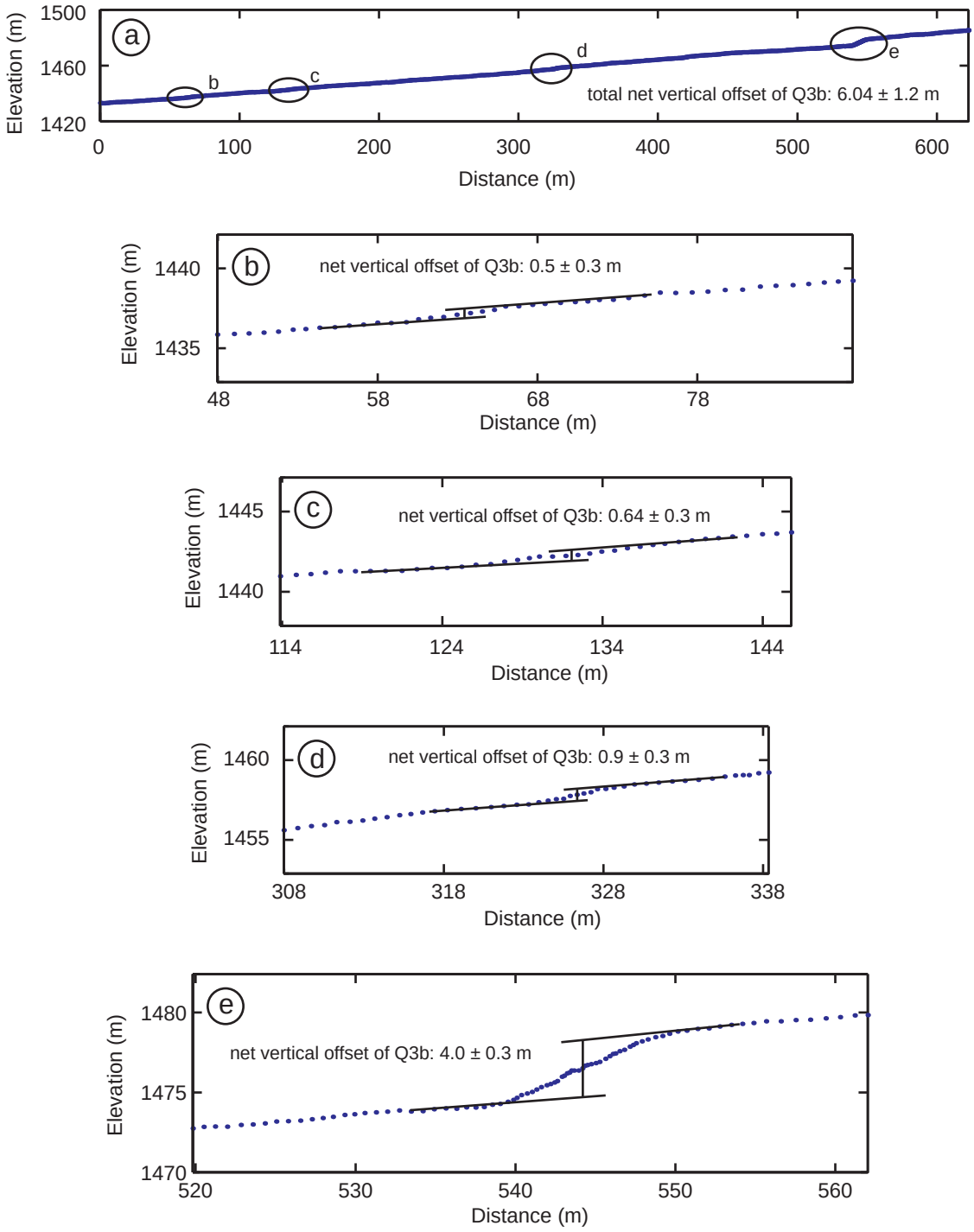

Figure 7. Topographic profile across Q3b fan surface at cosmogenic sampling locale with calculated vertical offsets. The etire profile section is shown in (a), and individual scarps along the profile are included as (b), (c), (d), and (e). Calculated scarp height is measured at the center of the scarp, see Figure 3 for aerial view showing profile location, and Figure 6 for idealized fault scarp morphology.

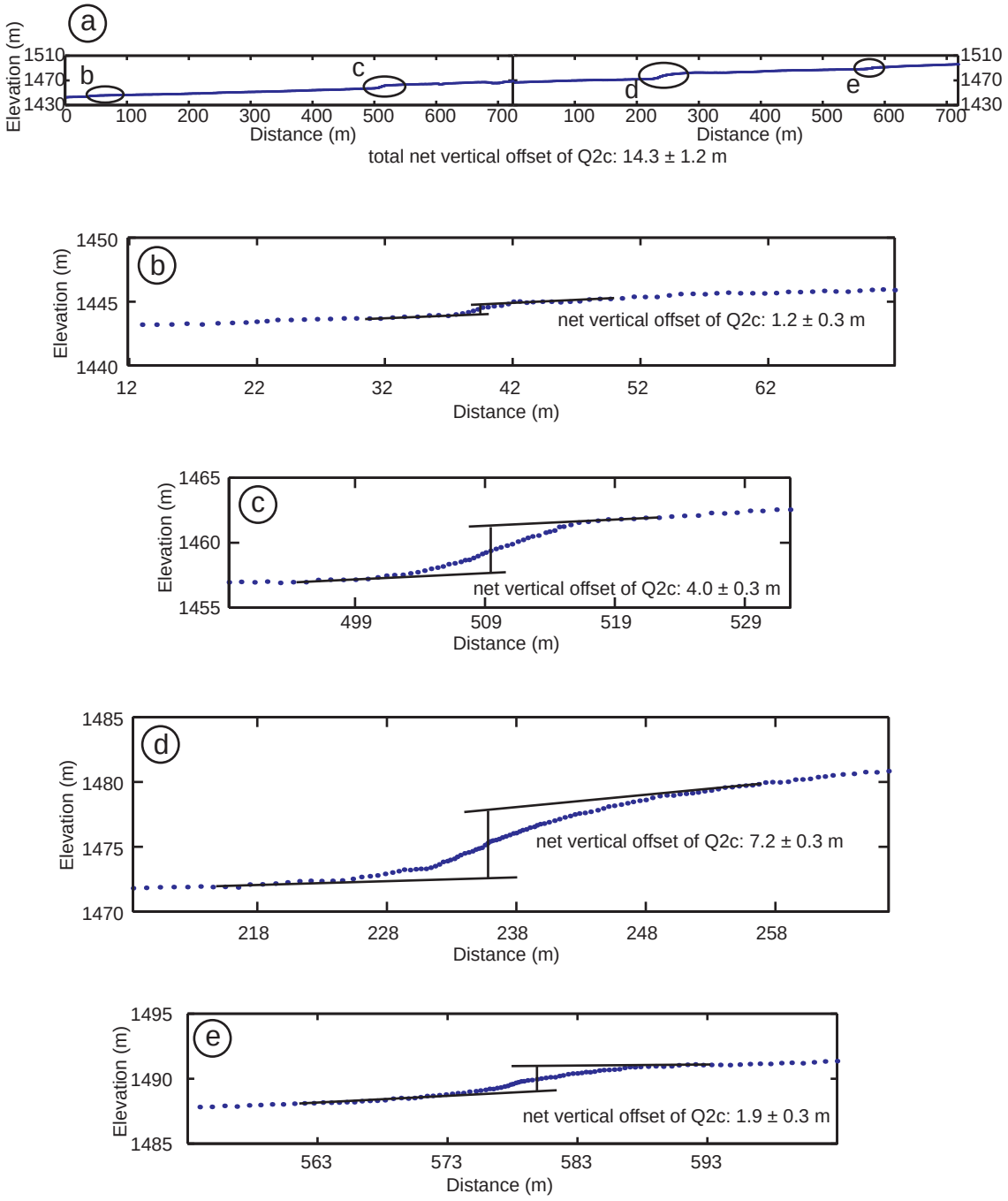

Figure 8. Topographic profile across Q2c fan surface at cosmogenic sampling locale with calculated vertical offsets. The entire profile section is shown in (a), and individual scarps along the profile are included as (b), (c), (d), and (e). Calculated scarp height is measured at the center of the scarp, see Figure 4 for aerial view showing profile location, and Figure 6 for idealized fault scarp morphology.

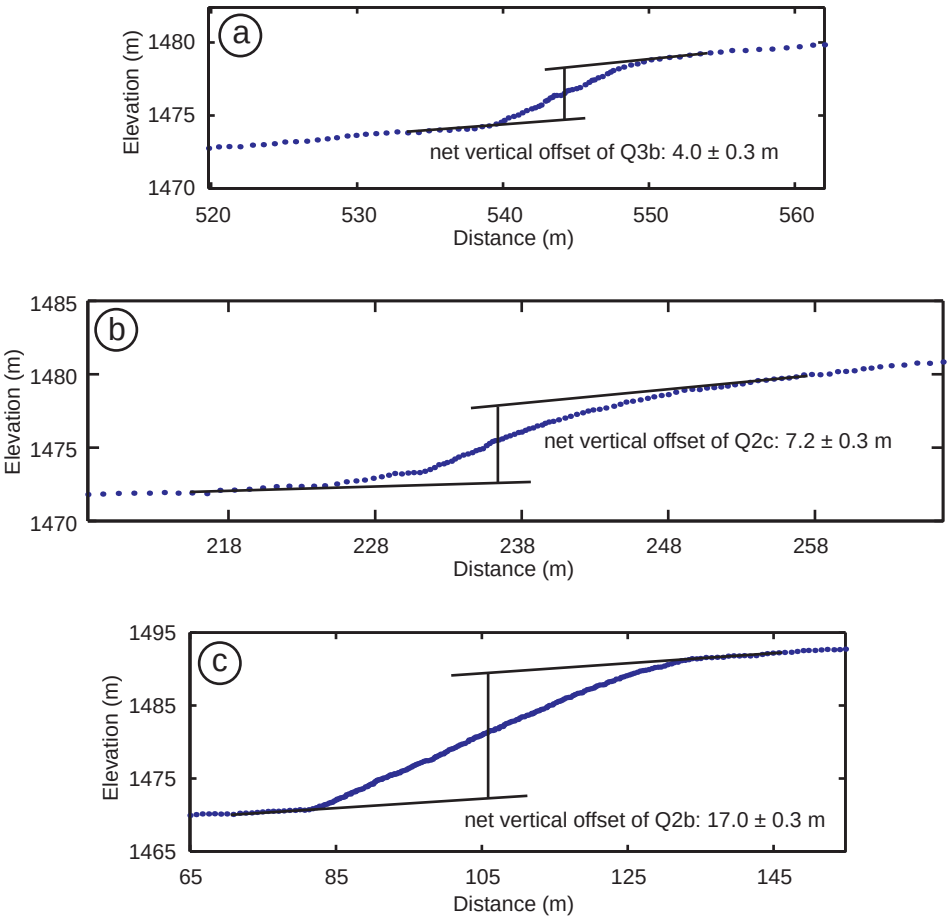

Figure 9. Comparison of largest scarps on Q3b (a), Q2c (b) and Q2b (c) alluvial fan surfaces. See Figure 6 for idealized fault scarp morphology explanation.

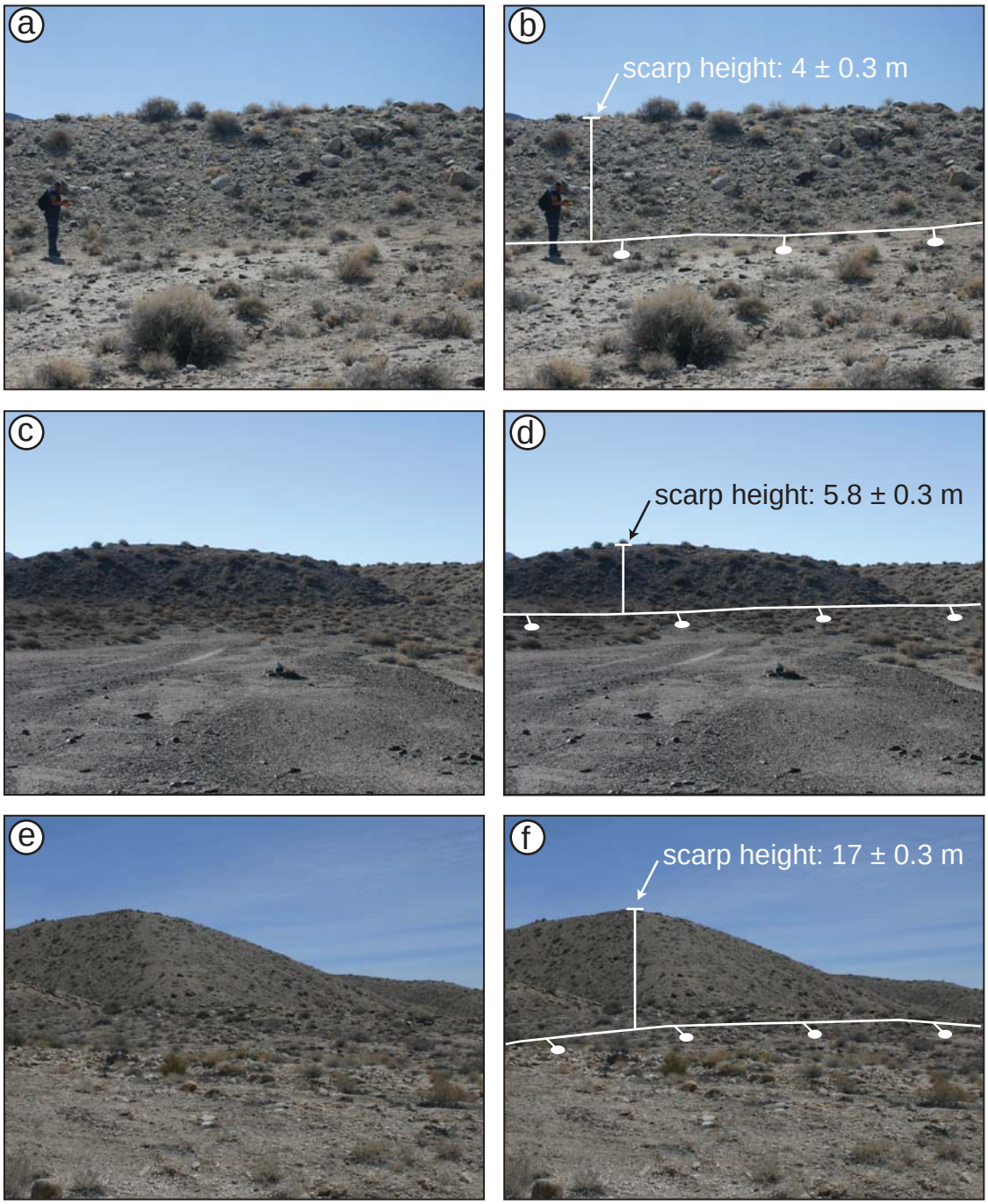

Figure 10. Photographs showing typical fault scarp morphology on different alluvial fan surfaces. (a) Field photograph of the Q3b alluvial fan surface looking south-east. (b) Annotated field photograph showing fault trace location and scarp height. (c) Field photograph of the Q2c alluvial fan surface looking south-east. (d) Annotated field photograph showing fault trace location and scarp height. (e) Field photograph of the Q2b alluvial fan surface looking due south. (f) Annotated field photograph showing fault trace location and scarp height.

Vertical displacements of Q2b were measured along the largest identified fault scarp and result in a displacement of 17 ± 0.3 m (Fig. 9c). It should be noted that all scarp measurements are minimum estimates; while we are confident that we captured all measurable displacement across these fan units, we cannot completely rule out off-fault deformation or the potential for unidentified fault strands. For example, the hanging wall of Q2b is not preserved, so it is possible there was more displacement that is no longer reflected in the surface geology. To determine extension rates we dated the three displaced fan surfaces using terrestrial cosmogenic nuclide geochronology.

CHAPTER 3. TERRESTRIAL COSMOGENIC NUCLIDE GEOCHRONOLOGY

The accumulation of terrestrial cosmogenic nuclides (TCN), produced through the interaction of cosmic rays and minerals at the earth's surface, can be used to determine the age of alluvial landforms (Lal, 1991; Gosse and Phillips, 2001). TCN methods provide distinct advantages when determining surface exposure ages where datable organic materials are scarce or nonexistent, or where deposits are beyond the age limit of radiocarbon dating (~40 ka). Here, we use cosmogenic nuclide ^{10}Be geochronology to determine the age of the offset Q3b, Q2c, and Q2b alluvial fans.

Beryllium-10 is produced through spallation and muon-induced reactions with Si and O in quartz (Gosse and Phillips, 2001). Quartz is the preferred sample material due to the relative stoichiometric simplicity and propensity to retain ^{10}Be, as well as its resistance to weathering. A total of 21 samples were collected, eight surface samples each on the Q3b and Q2c surfaces, and five samples from a single depth profile on the Q2b surface. We selected surface samples that appeared to be in their original depositional geometry, remaining exposed at the surface since emplacement. Two potential problems that can be encountered with surface sampling include inheritance and erosion. Samples ideally have no prior exposure history (inheritance), which could yield an artificially old surface age. Conversely, the effects from erosion or exhumation can provide artificially young ages; following surface abandonment, a clast that has been recently exhumed from beneath the surface or a clast that has had extensive surface erosion will have a lower TCN concentration.

For sample collection on the Q3b and Q2c surfaces we targeted flat-lying quartzite cobbles with well-developed varnish and rubification, located along flat, stable portions of fan surfaces (Figs. 3 and 4; Appendix D). All samples were surrounded by moderately- to well-developed desert pavements, with at least 20% of the cobble height exposed above the fan surface. Cobbles with obvious weathering or evidence of disturbance or recent exhumation were avoided. The upper 3 to 5 cm of each sample was used (Table 2). Sample locations are shown on Figures 3 and 4, and photographs of samples are included in Appendix D.

There were no suitably large, undisturbed cobble-size or larger clasts located on the Q2b fan surface. As a result, this surface was dated using a depth profile. We dug a 2-m-deep pit in a stable portion of the fan surface (Fig. 3), and collected approximately 1,500 g of 0.25 to 1 mm sized clasts at the following depth intervals: 25 cm, 55 cm, 85 cm, 125 cm, and 195 cm (Appendix D). The concentration of TCNs diminishes quasi-exponentially as a function of depth beneath ground surface (e.g., Anderson et al., 1996; Gosse and Phillips, 2001), so by projecting the depth verses ^{10}Be concentration accumulation curve to the surface, a model surface age can be determined (e.g., Anderson et al., 1996; Hancock et al., 1999). Additionally, one advantage of using a depth profile is that levels of inheritance can be quantified. At depths exceeding ~2 m in alluvium the accumulation of TCNs is negligible, so extrapolating the depth vs. TCN accumulation curve to >2 m we can determine the level of inheritance (e.g., Anderson et al., 1996).

Table 2. Analytical results of terrestrial cosmogenic nuclide ^{10}Be geochronology for the northwest Lone Mountain and Weepah Hills piedmont: surface samples.

Sample name	Latitude	Longitude	Elevation	Thickness[a]	Production rate		Shielding	Denudation	Quartz[d]	Be carrier	^{10}Be/^{9}Be[e,f]	^{10}Be concentration[f,g,h]	Age[f,i,j]
					spallation[b]	muons[c]	factor	rate					
	(°N)	(°E)	(m)	(cm)	(atoms g^{-1} yr^{-1})	(atoms g^{-1} yr^{-1})		(mm yr^{-1})	(g)	(g)	(x 10^{-13})	(10^{5} atoms g^{-1} SiO_2)	(ka)
Q3b													
LM-0509-10	38.04141667	-117.57533	1504	4	12.93	0.290	1	0	69.2954	0.2933	21.7 ± 0.49	7.07 ± 0.18	54.2 ± 5.0
LM-0509-11	38.04088889	-117.57408	1517	5	12.95	0.290	1	0	77.5810	0.2942	39.0 ± 0.60	11.40 ± 0.21	88.1 ± 8.0
LM-0509-12	38.04061111	-117.575	1514	4	13.03	0.291	1	0	79.9709	0.3020	7.6 ± 0.18	2.22 ± 0.06	16.7 ± 1.5
LM-0509-13	38.04330556	-117.57467	1485	4.5	12.71	0.288	1	0	80.3913	0.2948	6.8 ± 0.16	1.91 ± 0.05	14.7 ± 1.3
LM-0509-14	38.04308333	-117.57731	1480	4	12.71	0.288	1	0	62.5879	0.2940	11.7 ± 0.27	4.22 ± 0.11	32.7 ± 3.0
LM-0509-15	38.04216667	-117.57658	1488	4.5	12.73	0.288	1	0	80.1825	0.3025	8.4 ± 0.19	2.43 ± 0.06	18.7 ± 1.7
LM-0509-17	38.04138889	-117.57531	1506	4.5	12.9	0.290	1	0	79.9149	0.3048	15.8 ± 0.28	4.63 ± 0.10	35.4 ± 3.2
LM-0509-18	38.02113889	-117.60003	1484	4	12.74	0.288	1	0	80.0501	0.3036	7.6 ± 0.16	2.20 ± 0.05	17.0 ± 1.5
Q2c													
LM-0509-01	38.01902778	-117.59664	1500	4	12.89	0.290	1	0	20.1060	0.3048	23.0 ± 0.42	26.90 ± 0.56	215.5 ± 20.3
LM-0509-02	38.01891667	-117.59608	1506	4	12.95	0.290	1	0	20.5545	0.2997	33.9 ± 0.60	38.08 ± 0.77	311.1 ± 30.1
LM-0509-04	38.01536111	-117.59056	1519	5	12.96	0.291	1	0	20.3220	0.3058	27.3 ± 0.64	31.71 ± 0.81	255.2 ± 24.7
LM-0509-05	38.01522222	-117.59039	1530	3.25	13.26	0.293	1	0	19.9992	0.3063	14.7 ± 0.28	17.32 ± 0.37	132.2 ± 12.2
LM-0509-06	38.01877778	-117.59558	1503	4	12.92	0.290	1	0	20.2235	0.3102	23.2 ± 0.43	27.39 ± 0.58	219.2 ± 20.7
LM-0509-07	38.01894444	-117.59569	1505	5	12.83	0.289	1	0	19.9835	0.3062	17.2 ± 0.32	20.24 ± 0.43	160.7 ± 15.0
LM-0509-08	38.01797222	-117.59483	1508	5	12.86	0.290	1	0	20.5090	0.3042	10.1 ± 0.23	11.50 ± 0.29	89.5 ± 8.3
LM-0509-19	38.04158333	-117.57575	1506	5	12.85	0.289	1	0	79.9897	0.3058	41.5 ± 0.86	12.24 ± 0.28	95.4 ± 8.8

[a]The tops of all samples were exposed at the surface.

[b]Constant (time-invariant) local production rate based on Lal (1991) and Stone (2000).

[c]Constant (time-invariant) local production rate based on Heisinger *et al.* (2002a, b).

[d]A density of 2.7 g cm^{-3} was used based on the quartzite composition of the surface samples.

[e]Isotope ratios were normalized to ^{10}Be standards prepared by Nishiizumi *et al.* (2007) with a value of 2.85 x 10^{12} andusing a ^{10}Be half-life of 1.36 x 10^{6} years.

[f]Uncertainties are reported at the 1σ confidence level.

[g]A mean blank value of 77,345 ± 16,385 ^{10}Be atoms (^{10}Be/^{9}Be = 3.27 x 10^{-15} ± 7.1 x 10^{-16}) was used to correct for background.

[h]Propagated uncertainties include error in the blank, carrier mass (1%), and counting statistics.

[i]Propagated error in the model ages include a 6% uncertainty in the production rate of ^{10}Be and a 4% uncertainty in the ^{10}Be decay constant.

[j]Beryllium-10 model ages were calculated with the CRONUS-Earth online calculator version 2.2 (Balco et al., 2008; http://hess.washington.edu/math/).

Following collection, samples were processed at the Georgia Institute of Technology Cosmogenic Nuclide Geochronology Laboratory. Depth profile and surface samples were first crushed, ground, and sieved to a range of 250 to 500 μm and quartz was isolated using procedures described in Kohl and Nishiizumi (1992). Beryllium was then extracted from the quartz by ion exchange chromatography, precipitated as $Be(OH)_2$, and oxidized to BeO (e.g., Bierman et al., 2002). The beryllium oxide was ignited and mixed with niobium powder during packing in stainless steel cathodes. Samples were analyzed by accelerator mass spectrometry at the Lawrence Livermore National Laboratory Center for Accelerator Mass Spectrometry. Measured $^{10}Be/^{9}Be$ ratios were converted to ^{10}Be concentrations and model ages were calculated with the CRONUS-Earth online calculator, version 2.2 (http://hess.ess.washington.edu/; Balco et al., 2008; Table 2).

Currently there is no consensus regarding the best way to model time-variable TCN production rates. (e.g., Lal, 1991; Stone, 2000; Dunai 2001; Desilets & Zreda, 2003; Pigati and Lifton, 2004; Desilets et al. 2006; Lifton et al. 2005; Balco et al. 2008; Staiger et al., 2008). Because of this, we use a time-invariant production model to determine our fan ages (Lal, 1991; Stone, 2000). For comparison, ages based on time-variable production rates are included as Appendix E. Regardless, age variability between different production rate models is low for the range of ages reported in this study. For a given sample, ages from the different production rate models are within ~10% of each other (Appendix E).

3.1 TCN Results and Interpretation

3.1.1 Q3b

Exposure ages for the Q3b surface show a range of ~73 ka, from ~15 to 88 ka (Table 2). A probability density plot (Fig. 11a) of the sample distribution shows that the largest peak is around 17 ka, where four of the eight samples are tightly clustered; to the right of this peak there is a tail, which signifies longer exposure histories for the remaining samples. The higher ^{10}Be concentrations in the four oldest samples are likely due to inheritance generated from prolonged exposure on hillslopes or older fan units prior to erosion or due to extended residence time in channels or floodplains during transport from the source area to depocenter. Based on these observations, we feel the four youngest samples likely represent a maximum age for the Q3b surface.

The highest peak within the probability density function (PDF) in Figure 11a is used to represent the ^{10}Be age of the offset Q3b surface. The tight range of ages within this clustering suggest diminished influence of inheritance, and a weighted mean of these samples results in an age of 16.5 ka ± 1.2 ka. This age is slightly younger than the mean utilizing all eight samples, but the uncertainty is substantially smaller. When compared to equivalent fan deposits in the region, there is good agreement and recent investigations in Death Valley yield similar Q3 surface ages (Sohn et al., 2007; Frankel et al., in review; Owen et al., in review).

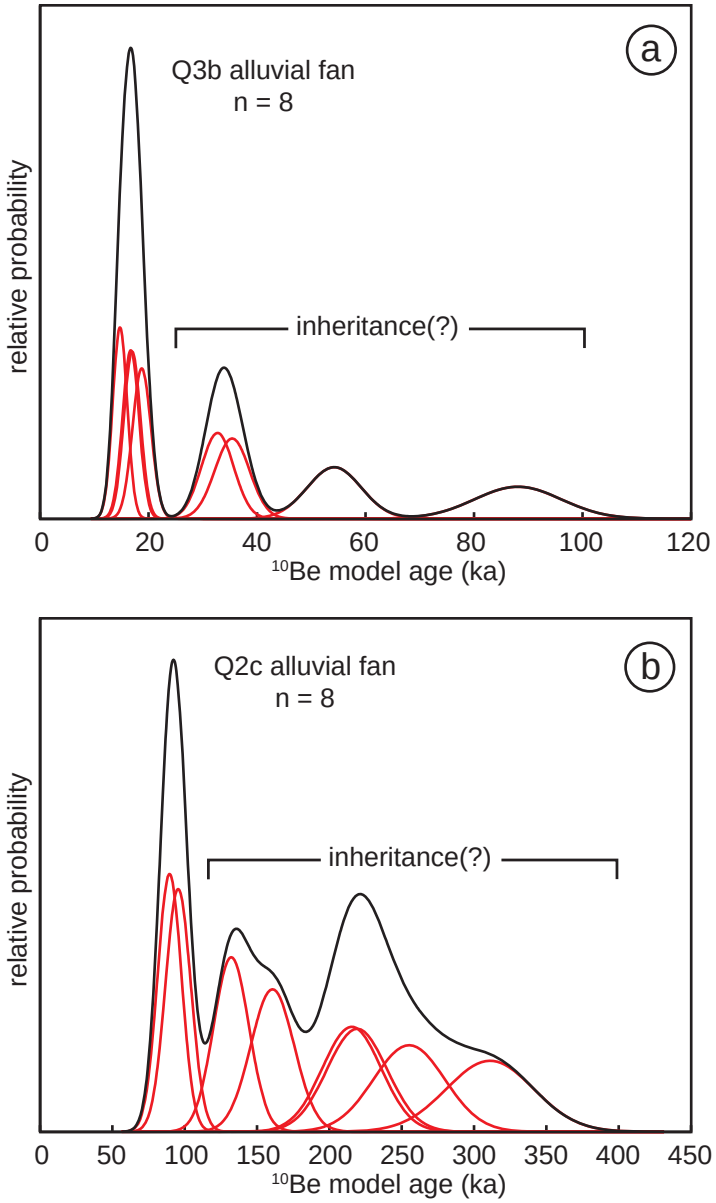

Figure 11. Probability distribution functions of cosmogenic ^{10}Be ages from the Lone Mountain Q3b (a) and Q2c (b) alluvial fans. Red curves indicate relative probability of individual samples from the fan surfaces. Solid black curves show cumulative probability distributions for all samples from fan surface.

3.1.2 Q2c

The samples collected from the displaced Q2c surface have a large age variance, ranging from ~89 to 311 ka (Table 2). Upon inspection of the PDF in Figure 11b, it is apparent that at least six of the samples have some level of inheritance. There is a tight cluster of two samples around ~92 ka with a large tail extending to the right of this peak. Because there is such a range of values older than ~92 ka, we think it appropriate to exclude the six oldest samples from surface age determination. Assessment based on the samples composing the primary peak of the PDF yields a mean of 92.3 ± 8.6 ka (Fig. 11b).

We chose the Q2c sampling site because the fan surfaces are the best expressed gemorphically, and have the most fault displacement across them. However, it should be noted that the source area for this Q2c fan is very large, with numerous drainages coming off both Lone Mountain and the Weepah Hills (Appendix A). A detailed investigation of these areas is beyond the scope of this study, but the likelihood of prolonged exposure in older sedimentary sequences prior to deposition during Q2c time is likely. This observation helps to explain the broad range of ^{10}Be concentrations observed in the Q2c surface samples and is common in arid and semi-arid environments (e.g., Owen et al., in review; Armstrong et al., 2010).

When the Q2c dates are compared to correlative fan deposits across the region, the 92.3 ± 8.6 ka age is similar to those reported in previous studies. In Fish lake Valley equivalent surfaces have ^{10}Be ages of 94 ± 11 ka (Furnace Creek fan) and 71 ± 8 ka (Indian Creek fan) (Frankel et al., 2007b); similar fan deposits in Death Valley also have ^{10}Be and ^{36}Cl

ages of approximately 70 to 90 ka (Frankel et al., 2007a; Machette et al., 2008). Based on the close proximity of these valleys, it is probable that climatic events controlling alluvial fan deposition are similar. Given the relative agreement between surface ages, we feel the exclusion of the six oldest samples to determine the Q2c surface age is reasonable. We therefore take the offset Q2c surface age to be 92.3 ± 8.6 ka, but recognize that if the samples used for this age also have an inherited component, the fan could be slightly younger.

3.1.3 Q2b

The ^{10}Be model age determined from the depth profile on the offset Q2b surface provides an age of 142.2 ± 19.5 ka. When compared to equivalent surfaces in Death Valley, our surface age falls within the middle of the ~130-180 ka age range (Machette et al., 2008). Individual sample concentrations from the Q2b depth profile are indicated in Table 3, and as shown in Figure 12, levels of inheritance are negligible. This low level of inheritance is supported by the close proximity of the deposit to its source area on the southwest flank of Lone Mountain (Fig. 3).

Table 3. Analytical results of terrestrial cosmogenic nuclide ^{10}Be geochronology for the northwest Lone Mountain and Weepah Hills piedmont: depth profile.

Sample name	Latitude (°N)	Longitude (°E)	Elevation (m)	Depth[a] (cm)	Shielding factor	Denudation rate (mm yr^{-1})	Quartz[b] (g)	Be carrier (g)	^{10}Be/^{9}Be[c,d] (x 10^{-13})	^{10}Be concentration[e,f,g] (10^{5} atoms g^{-1} SiO_2)
Q2b										
LM-0909-DP2-01	38.03416667	-117.574556	1554	25 ± 5	1	0	20.0111	0.3023	11.5 ± 0.23	13.36 ± 0.30
LM-0909-DP2-02	38.03416667	-117.574556	1554	55 ± 5	1	0	21.4998	0.3043	9.7 ± 0.22	10.57 ± 0.27
LM-0909-DP2-03	38.03416667	-117.574556	1554	85 ± 5	1	0	32.4352	0.3025	12.6 ± 0.23	9.07 ± 0.19
LM-0909-DP2-04	38.03416667	-117.574556	1554	125 ± 5	1	0	41.4923	0.3009	13.5 ± 0.31	7.54 ± 0.19
LM-0909-DP2-05	38.03416667	-117.574556	1554	195 ± 5	1	0	100.4489	0.3052	12.4 ± 0.24	2.90 ± 0.06

[a] For depth profile, collected clast sizes ranged between 250µm and 1mm. All clasts larger than 500µm were reduced to the 250-500µm grain size.

[b] A density of 2.7 g cm^{-3} was used based on the quartzite composition of the surface samples.

[c] Isotope ratios were normalized to ^{10}Be standards prepared by Nishiizumi *et al.* (2007) with a value of 2.85 x 10^{12} andusing a ^{10}Be half-life of 1.36 x 10^{6} years.

[d] Uncertainties are reported at the 1σ confidence level.

[e] A mean blank value of 77,345 ± 16,385 ^{10}Be atoms (^{10}Be/^{9}Be = 3.27 x 10^{-15} ± 7.1 x 10^{-16}) was used to correct for background.

[f] Propagated uncertainties include error in the blank, carrier mass (1%), and counting statistics.

[g] Propagated error in the model ages include a 6% uncertainty in the production rate of ^{10}Be and a 4% uncertainty in the ^{10}Be decay constant.

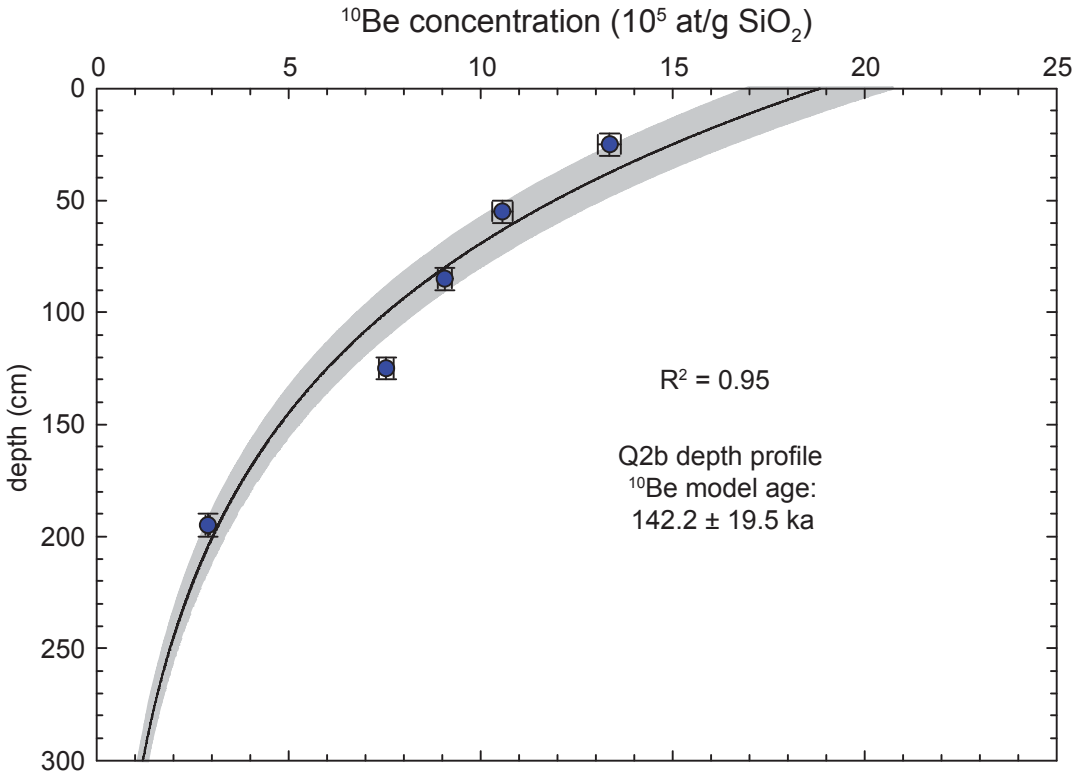

Figure 12. Sample depth verses beryllium concentration results from Q2b cosmogenic radionuclide depth profile samples. Gray shading represents ±10% confidence, and error bars represent 1σ. See Figure 3 for depth profile location, Table 3 for complete test result values, and text for further discussion.

CHAPTER 4 LATE PLEISTOCENE EXTENSION RATES

4.1 Extension

Critical to our assessment of extension is accurately determining fault dip. At the northern end of our field area, we identified an exposed fault plane cutting alluvium in a channel wall incised orthogonal to the fault (Fig. 13). We measured a dip of 40° toward 300º at this location (Figure 13b). As an upper bound for dip, we utilize 60°, which is a commonly assumed normal fault angle based on Andersonian mechanics (e.g., Twiss and Moores, 2007). We calculate two values of extension for each surface offset using the observed 40° dip and the more conservative 60° dip; the extensional displacements are reported in Table 4. To illustrate the effect of dip on extension, we plotted extension versus dip angle in Figure 14a. As the dip angle becomes shallower, the extension rapidly increases as the inverse to the tangent of the dip.

Figure 13. Field photograph showing an exposed fault plane in alluvium (a), view to the west. (b) Annotated photograph showing interpreted fault plane location. Field mesurments on the fault plane show a dip of 40° towards 300°.

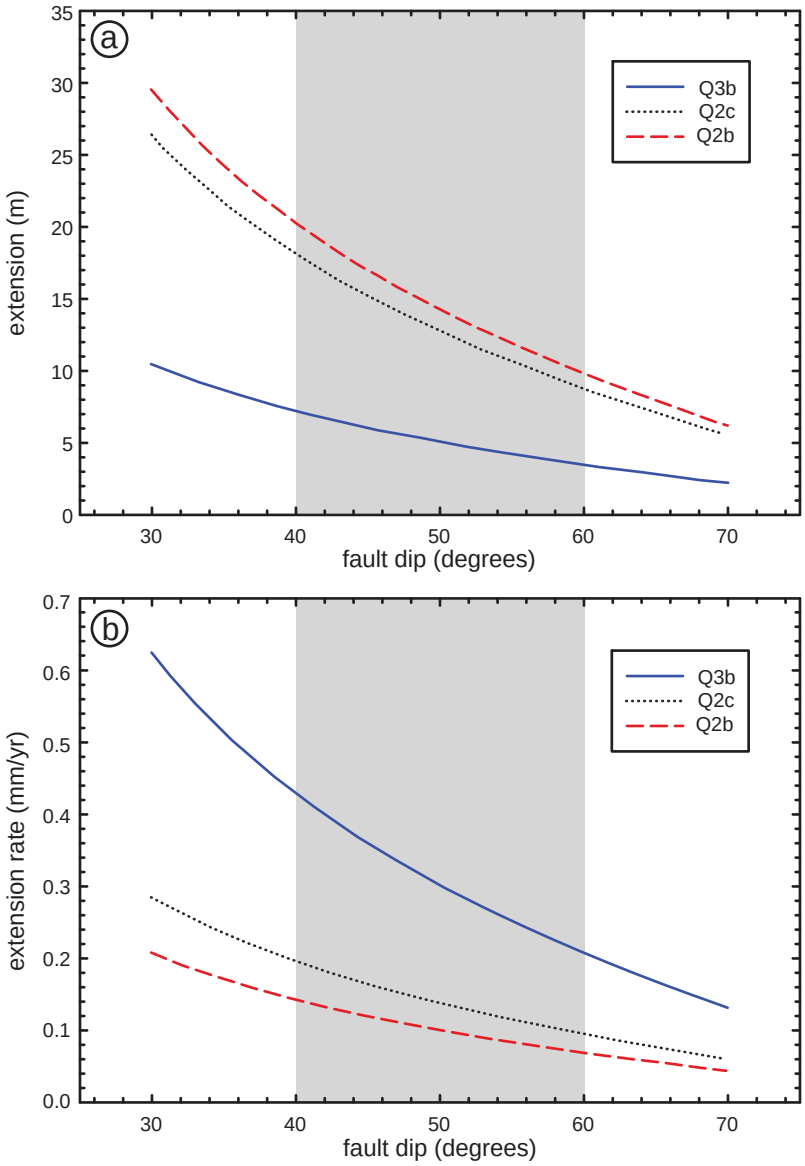

Figure 14. Graphs illustrating the influence of dip angle on (a) extension and (b) extension rate for the Q3b, Q2c and Q2b alluvial fan offsets. Q3b is shown as a solid blue line, Q2c is shown as a dotted black line, and Q2b is shown as a dashed red line. Gray shading between a fault dip of 40° and 60° indicate the range of likely values.

4.1.1 Q3b and Q2c

The vertical displacements across the Q3b and Q2c surfaces are 6.0 m ± 1.2 m and 14.3 ± 1.2 m, respectively. In both cases, several fault strands offset the alluvial surfaces, but the fan surfaces are continuous and identifiable in both the hanging wall and footwall (Figs. 3 and 4). We cannot account for any off-fault deformation, but it is likely a majority of this displacement is represented in the profiles. We therefore take the profile measurements to represent minimum offset distances, and these vertical offsets translate to extension ranging between 3.5 m and 7.2 m for Q3b, and 8.8 m and 18.1 m for Q2c, using dips of 40° and 60°, respectively (Table 4).

Table 4. Extension and extension rates along the Lone-Mountain fault

Fan Unit	Preferred Fan Surface age (ka)	Vertical Offset (m)	Extension with 40° dip (m)	Extension with 60° dip (m)	Extension Rate 40° dip (mm/yr)	Extension Rate 60° dip (mm/yr)
Q3b	16.5 ± 1.2	6.0	7.2	3.5	0.4 ± 0.1	0.2 ± 0.1
Q2c	92.3 ± 8.6	15.2	18.1	8.8	0.2 ± 0.1	0.1 ± 0.1
Q2b	142.2 ± 19.5	17	20.3	9.8	0.1 ± 0.1	0.1 ± 0.1

4.1.2 Q2b

Measurements across the Q2b surface yield a vertical offset of 17 ± 0.3 m. This distance is a minimum because Q2b is not preserved in the hanging wall. Using the observed dip of 40° and assumed dip of 60°, minimum extension values across Q2b range from 9.8 m to 20.3 m (Table 4). Although the full displacement across this unit cannot be measured, we can look at the nearby distribution of fault strands cutting the younger Q3b surface and infer the amount of displacement that may be missing across the Q2b surface. The topographic profile across Q3b shows several scarps of varying size (Fig. 7); the primary

offset is approximately 2/3 of the total displacement, and three smaller synthetic offsets comprise the remainder (Figs. 3 and 7). If ruptures occur in the same location, and rates have remained constant, then approximately one third to one half of the total displacement across Q2b may have been on secondary fault strands and not preserved in the hanging wall. This would suggest extension across the Q2b surface could be as much as 12.4 m (assuming a 60º dip) or 40.5 m (assuming a 40º dip) since deposition.

4.2 Rates of Extension

We utilize a probabilistic approach to calculate rates of extension by combining our results from TCN dating and the two horizontal displacement (extension) distances calculated using dip angles of 40° and 60° (e.g., Bird, 2007; McGill et al., 2009; Zechar and Frankel, 2009). The results of these calculations are reported in Table 4, and extension rate PDFs for each fan surface and the two dip angle scenarios are shown in Figure 15. The Q3b surface has an extension rate between 0.2 ± 0.1 mm/yr and 0.4 ± 0.1 mm/yr, while the Q2c surface suggests an extension rate of 0.1 ± 0.1 mm/yr to 0.2 ± 0.1 mm/yr. The Q2b extension rate is even lower at ≤0.1 ± 0.1 mm/yr. We show the range of possible extension rates as a function of dip angle in Figure 14b, and this illustrates the faster rate from the Q3b fans compared to the other two surfaces.

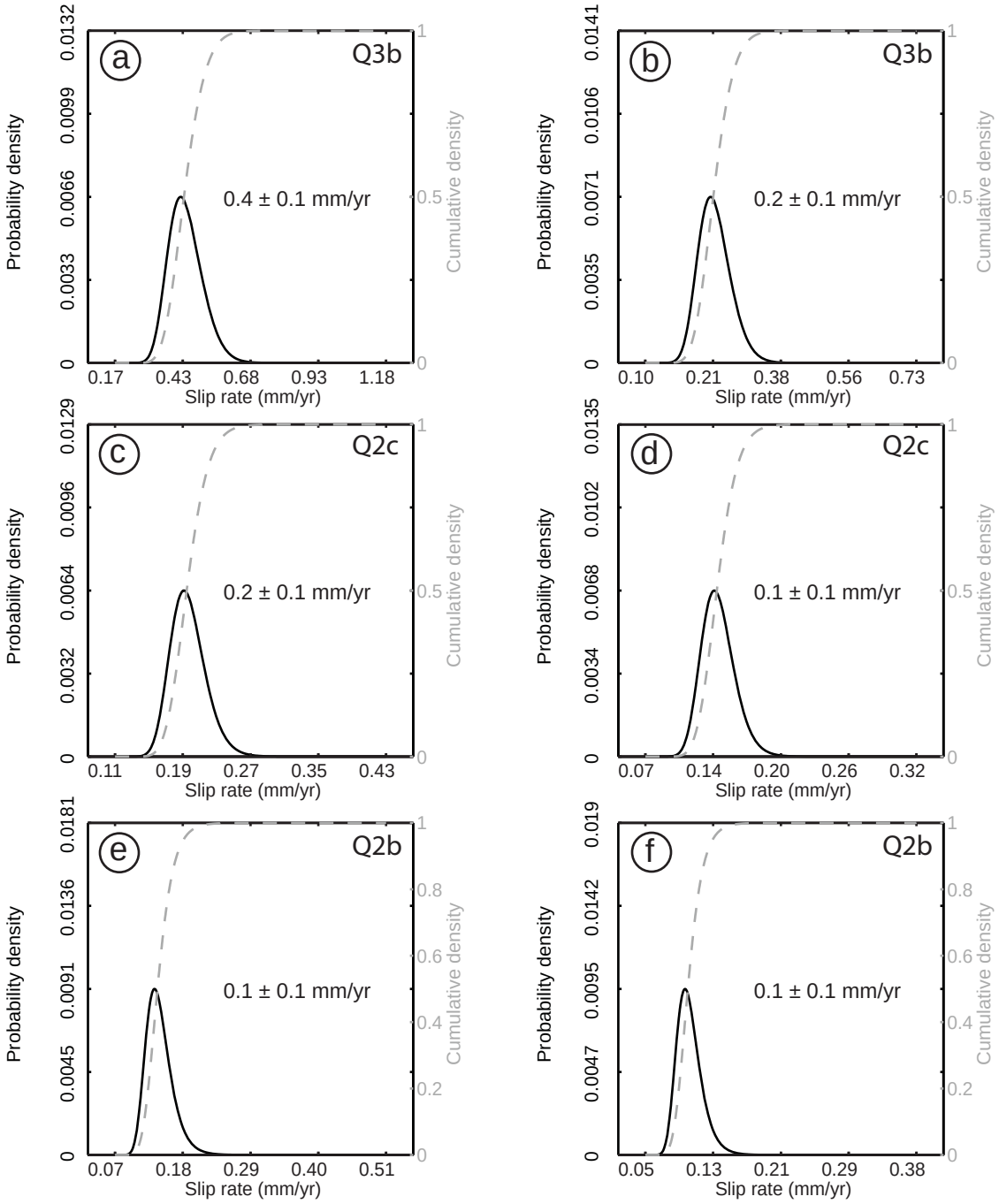

Figure 15. Probability distribution functions for extension rates based on total measured offset on each dated fan surface. (a) Extension rate based on preferred Q3b surface age and a fault dip angle of 40°, (b) extension rate based on preferred Q3b surface age and a fault dip angle of 60°, (c) extension rate based on preferred Q2c surface age and a fault dip angle of 40°, (d) extension rate based on preferred Q2c surface age and a fault dip angle of 60°, (e) extension rate based on Q2b depth profile age and a fault dip angle of 40°, (f) extension rate based on Q2b depth profile and a fault dip angle of 60°. Solid black line represents probability density function resulting from the convolution of TCN ages and offset measurements at each location. Dashed grey line is the cumulative distribution function for the same data (e.g., Zechar and Frankel, 2010).

CHAPTER 5. IMPLICATIONS FOR ECSZ STRAIN DISTRIBUTION

5.1 Strain Rates

At the northern extent of the ECSZ, there are relatively few structures accommodating right-lateral shear (Fig. 1). Individual faults along a transect drawn perpendicular to the azimuth of differential plate motion (~323° ± 2°; Bennett et al., 2003) including Lone Mountain at the northeast end, consist of the White Mountain fault, the DVFLV fault, the Emigrant Peak fault, and the Silver Peak-Lone Mountain extensional complex. Previous studies report late Pleistocene shear rates for the two main right-lateral strike-slip faults in the region to be 0.3 to 0.4 mm/yr on the White Mountain fault and ~2.5 to 3 mm/yr at the north end of the DVFLV fault (Kirby et al, 2006; Frankel et al., 2007b). Reheis and Sawyer (1997) report vertical slip rates across displaced Pleistocene fans on the Emigrant Peak fault, which correspond to an extension rate of ~1.2 to 3.4 mm/yr (fault dips used to calculate these rates are 45° and 70°, based on field observations; Reheis and Sawyer, 1997). Our results are the first to provide geologically-determined late Pleistocene rates for part of the SPLM.

The Silver Peak-Lone Mountain extensional complex is the most prominent tectonic feature east of the DVFLV and Emigrant Peak faults, and the Lone Mountain fault is the best geomorphically-expressed structure within it. We show the Lone Mountain fault accommodates right-lateral shear at a rate equal to or greater than 0.1 ± 0.1 to 0.2 ± 0.1 mm/yr since ~92 ka, and at a faster rate of 0.2 ± 0.1 to 0.4 ± 0.1 mm/yr, since ~17 ka. Based on preliminary field reconnaissance of the other faults within the SPLM extensional complex, it is likely the Lida and Clayton Valley faults have comparable

rates, although future work should address these regions. In consideration of these preliminary observations, the down-to-the-northwest faults in the SPLM extensional complex may be accommodating right-lateral shear at a rate as high as ~1 mm/yr.

When our results are combined with the right-lateral shear rates on nearby faults, they suggest a discrepancy between short- and long-term cumulative strain rates across the region. A summation of late Pleistocene rates of right-lateral shear across the White Mountain, DVFLV, Emigrant Peak, and Lone Mountain fault suggest a right-lateral shear rate of 4.1 to 7.3 mm/yr (fig.16), which is substantially slower than the regional geodetically-determined short-term rate of 9.3 ± 0.2 mm/yr (Bennett et al., 2003). Based on our preliminary observations, the Lida and Clayton Valley faults may contribute a similar amount of strain as the Lone Mountain fault, but are not likely to account for the >2 mm/yr.

The apparent mismatch between these rates can be resolved by three possibilities: 1) strain accumulation has been constant since the late Pleistocene, and there is a strain transient, whereby the present-day rate of strain accumulation is not reflected in the geologic record, 2) strain rates are increasing, and as a result the geodetic rates should not be expected to match the geologic rates, or 3) deformation rates have remained constant, there is no anomalous strain accumulation, and additional structures, such as the Lida and Clayton Valley faults, account for the apparent slip deficit .

Different sections of the ECSZ appear to behave differently. South of the Garlock fault

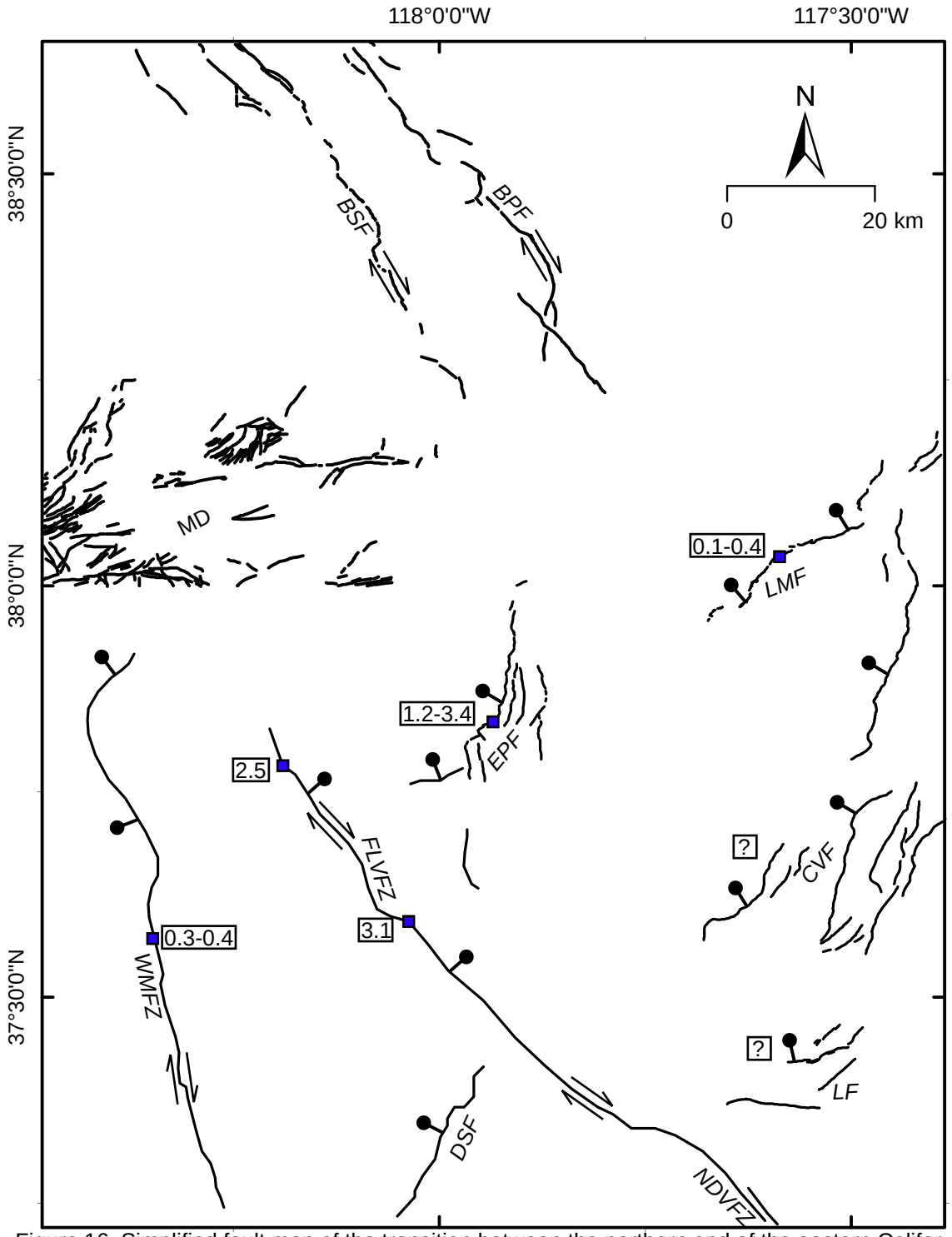

Figure 16. Simplified fault map of the transition between the northern end of the eastern California shear zone and the central Walker Lane, showing the major faults accommodating regional right-lateral shear. Geologically determined slip-rates are given in mm/yr, and blue squares indicate locations where slip rates were determined (Reheis and Sawyer, 1997; Kirby et al., 2006; Frankel et al., 2007b). BSF - Benton Springs Fault; BPF - Bettles Well-Petrified Springs fault; CVF - Clayton Valley fault; DSF- Deep Springs fault; EPF - Emigrant Peak fault; FLVFZ - Fish Lake Valley fault zone; LF - Lida Fault; LMF - Lone Mountain Fault; MD - Mina Deflection; NDVFZ - northern Death Valley fault zone; WMFZ - White Mountain fault zone.

studies have shown an apparent strain transient in the Mojave block, but at the latitude of northern Death Valley there is general agreement between geologic and geodetic records of deformation (e.g. Peltzer et al., 2001; Frankel et al., 2007a; Oskin et al., 2008; Lee et al., 2009b). The summation of strain rates at the north end of the ECSZ are at ends with the geodetic rate, and our observations suggest the Lone Mountain is helping accommodate strain across the ECSZ-central Walker Lane transition zone, but not responsible for the >2 mm/yr "missing" from the geologic rate. If the apparent mismatch in strain rates observed at this point of transition is similar to that of the Mojave block, a strain transient at this part of the plate boundary could reconcile deformation rates.

Our results are consistent with the idea of a strain transient, but also suggest the possibility for an increase in strain accumulation and release in this part of the plate-boundary. Detecting increases in strain rate can be difficult to identify because resolution of discretely datable intervals preserved in the geologic record that show changing rates of displacement are often scarce. Across the Lone Mountain fault, we identify variable rates of strain release over late Pleistocene timescales, which suggest deformation may become progressively faster from the late Pleistocene to the present.

The offset Q2b surface suggests a rate of ≥0.1 mm/yr over ~140 ka timescales. The uncertainty in this rate is high due to the fact that the Q2b surface is not preserved in the hanging wall. As a result, this rate could be ~0.2 mm/yr faster (using a 40° fault dip) if the total offset across Q2b is twice as much as is observed in the field. Rates of extension across the Q2c deposit range from ~0.1 to 0.2 mm/yr since ~92 ka, but if the surface is

younger, similar to the Fish Lake Valley and Death Valley fans with similar soil development and morphology, the rate could be as much as 0.1 mm/yr faster. The rate derived from the Q3b fan is ~0.2 to 0.4 mm/yr, which is faster than the rates from the Q2c or Q2b age offsets, even when we consider a younger Q2c fan age or additional displacement across the Q2b surface. If indeed the strain rates are increasing, as our data suggest, then the short-term strain accumulation rates do not necessarily need to match long-term strain release rates. In this case, the faster rates of right-lateral shear observed in the geodetic data may simply reflect an increase in strain accumulation over latest Pleistocene to recent timescales.

Alternatively, if rates are constant, and there is no strain transient, then it is possible nearby structures may be accommodating the remaining strain. Detailed studies on the Emigrant Peak fault, Clayton Valley fault, and Lida fault, among others, should be pursued to determine their role in accommodating strain along this part of the Pacific-North America plate boundary.

5.2 Strain Transfer

Strain transfer between the major right-lateral faults of the eastern California Shear zone and the central Walker Lane is thought to primarily be accommodated by the left-lateral oblique faults of the Mina Deflection and the normal faults of the Emigrant Peak and Silver Peak extensional complex (e.g., Oldow, 1994; Reheis and Sawyer, 1997; Frankel et al., 2007b; Lee et al., 2009a; Ganev et al., 2010;). Lee et al. (2009a) suggest that strain from the White Mountain fault is transferred to the Mina Deflection via the Queen Valley fault. Ganev et al. (2010) show that slip is “pulled” off the DVFLV fault system in a

northward progression via extension and transferred to the Emigrant Peak fault system and around the eastern end of the Mina Deflection. These structures, together with the faults of the Silver Peak-Lone Mountain extensional complex, transfer strain northward and ~80 km eastward to the southern end of the right-lateral oblique Benton Springs and Bettles Well-Petrified Springs faults that make up the southern end of the central Walker Lane (Fig. 1).

If strain is transferred eastward via distributed normal faulting to the Emigrant Peak fault at the north end of Fish Lake Valley, it is clear based on orientation and proximity, the faults of the SPLM extensional complex also must partition some of the right-lateral shear onto down-to-the-northwest faults. This helps explain the gradual northward decrease in right-lateral slip rates observed along the DVFLV fault (e.g., Frankel et al., 2007b; in review) and the northward transfer of strain along this important segment of the Pacific-North America plate boundary.

CHAPTER 6. CONCLUSIONS

New geologic and geomorphic mapping, together with TCN geochronology of three offset alluvial fans along the Lone Mountain and Weepah Hills piedmonts provide the first geologically-determined late Pleistocene extension rates for the Lone Mountain fault, an important component of the SPLM extensional complex. We document an extension rate ≤ 0.1 ± 0.1 mm/yr based on a Q2b surface with an age of 142 ± 19.5 ka; a rate of 0.1 ± 0.1 to 0.2 ±0.1 mm/yr since 92.3 ± 8.6 ka based on a displaced Q2c surface; and a rate of 0.2 ± 0.1 to 0.4 ± 0.1 mm/yr based on an offset Q3b fan with a ^{10}Be age of 16.5 ± 1.2 ka. These results show the Lone Mountain fault has been active since the late Pleistocene and extension rates have increased between ~92 ka (Q2c) and ~17 ka.

When late Pleistocene right-lateral shear rates from other faults at the north end of the ECSZ are combined with our extension rates, the cumulative long-term rate is apparently slower than geodetic observations. Based on our observations, this discrepancy implies either: 1) there is a strain transient; 2) strain rates are increasing, and geologic records should not match geodetic data; or 3) strain rates are constant, there is no transient, and strain is accommodated on yet-to-be documented structures. Furthermore, our results show that the Lone Mountain fault is an important structure that acts to partition strain off of the major strike-slip faults in the northern ECSZ and helps transfer deformation around the Mina Deflection northward into the Walker Lane.

APPENDIX A

GEOLOGIC MAP OF LONE MOUNTAIN FAULT ZONE

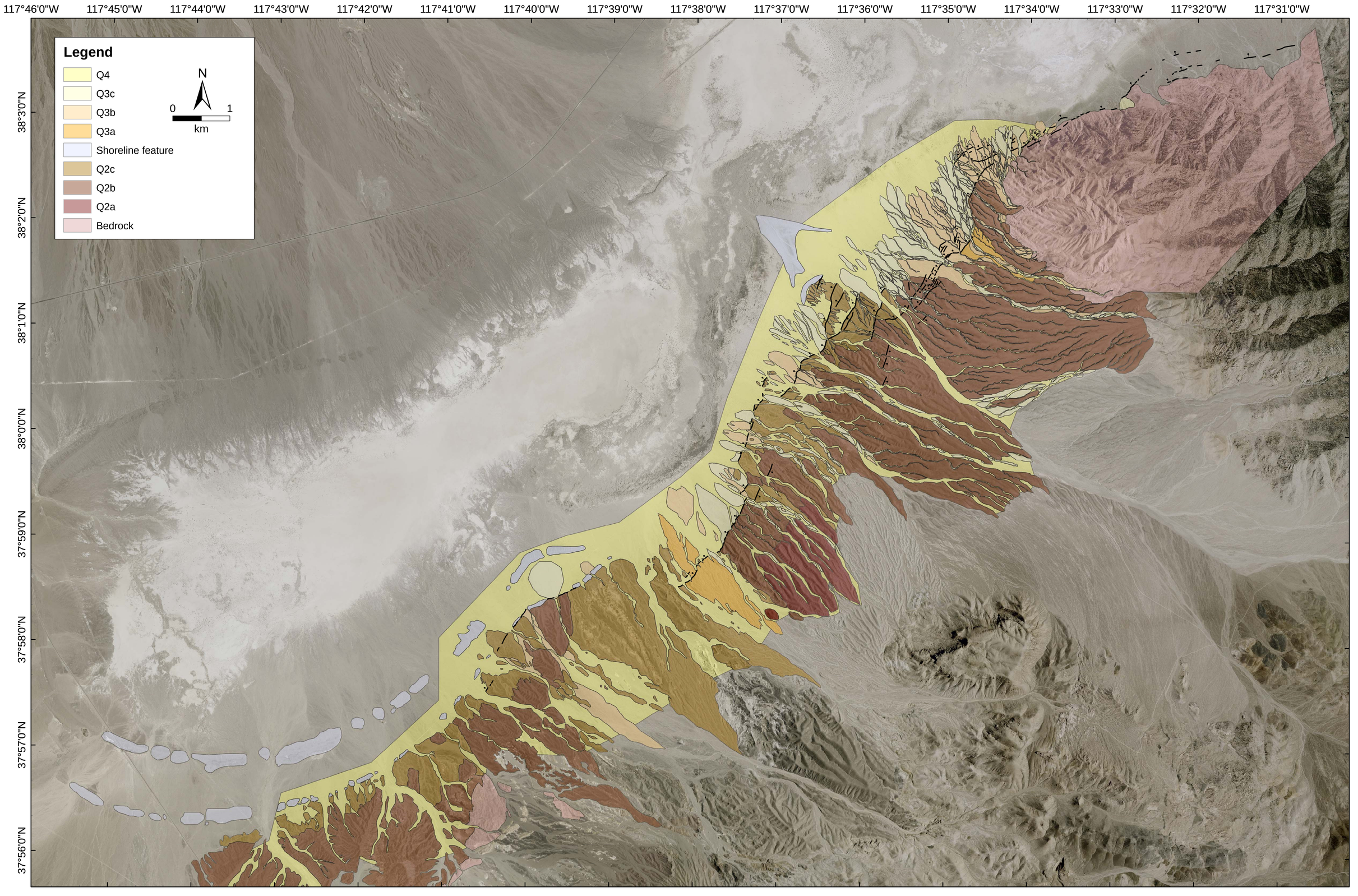
Legend
Q4
Q3c
Q3b
Q3a
Shoreline feature
Q2c
Q2b
Q2a
Bedrock
N
0
1
km
117°46'0"W
117°45'0"W
117°44'0"W
117°43'0"W
117°42'0"W
117°41'0"W
117°40'0"W
117°39'0"W
117°38'0"W
117°37'0"W
117°36'0"W
117°35'0"W
117°34'0"W
117°33'0"W
117°32'0"W
117°31'0"W
38°3'0"N
38°2'0"N
38°1'0"N
38°0'0"N
37°59'0"N
37°58'0"N
37°57'0"N
37°56'0"N

APPENDIX B

TOPOGRAPHIC SCARP PROFILES

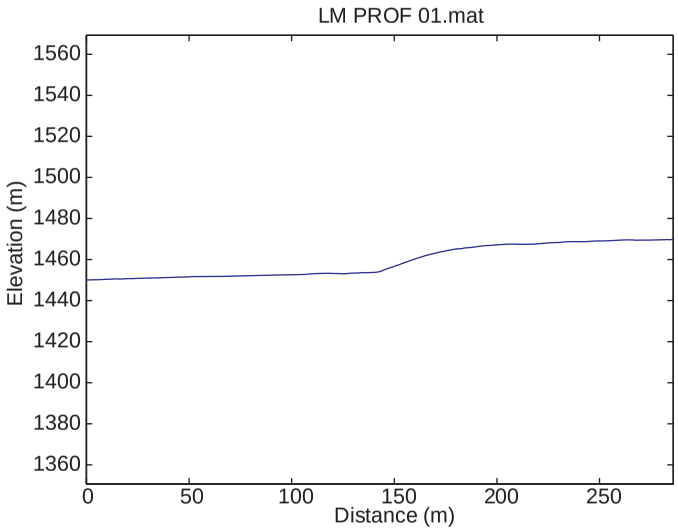
LM PROF 01.mat
Elevation (m)
1560
1540
1520
1500
1480
1460
1440
1420
1400
1380
1360
0
50
100
150
200
250
Distance (m)

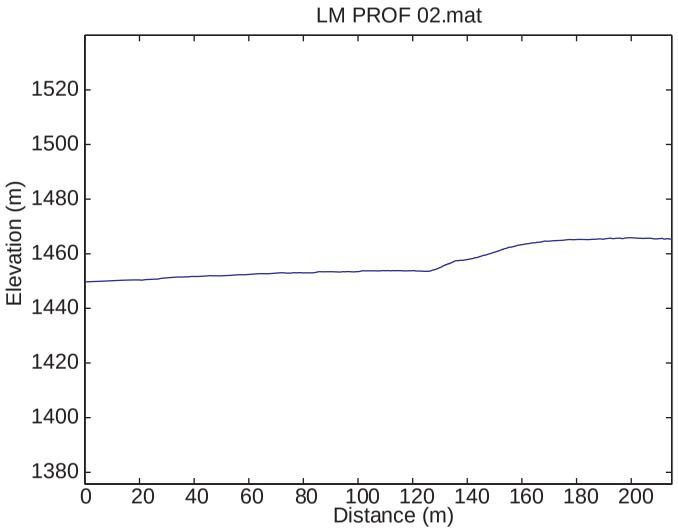
LM PROF 02.mat
Elevation (m)
1520
1500
1480
1460
1440
1420
1400
1380
0
20
40
60
80
100
120
140
160
180
200
Distance (m)

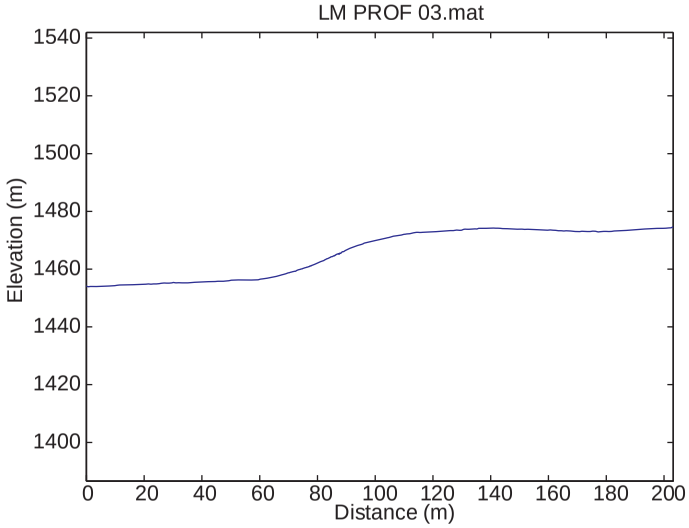
LM PROF 03.mat
Elevation (m)
1540
1520
1500
1480
1460
1440
1420
1400
0
20
40
60
80
100
120
140
160
180
200
Distance (m)

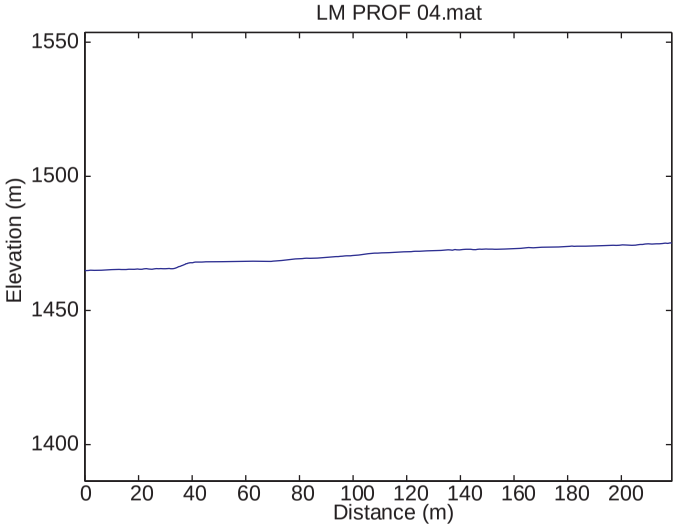
LM PROF 04.mat
Elevation (m)
1550
1500
1450
1400
0
20
40
60
80
100
120
140
160
180
200
Distance (m)

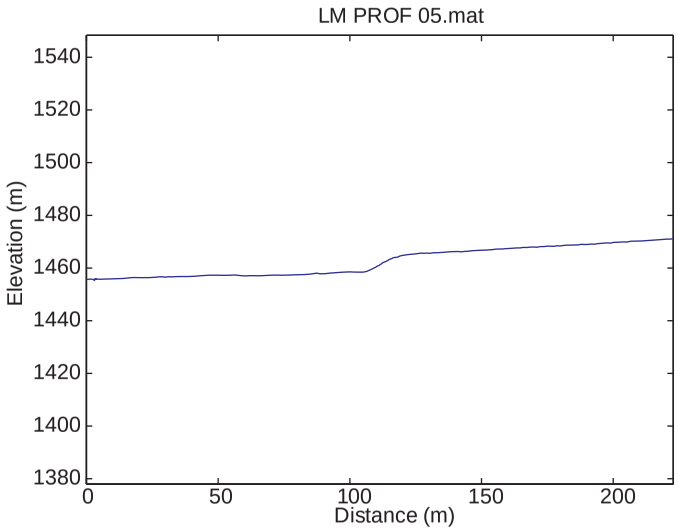
LM PROF 05.mat
Elevation (m)
Distance (m)
1540
1520
1500
1480
1460
1440
1420
1400
1380
0
50
100
150
200

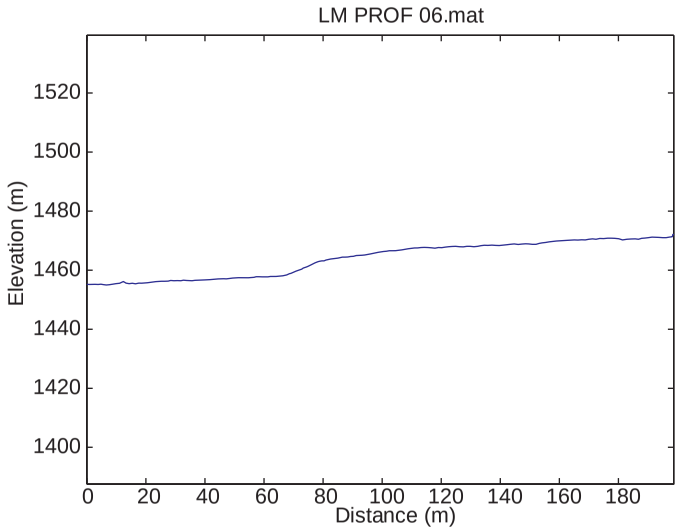
LM PROF 06.mat
Elevation (m)
Distance (m)
1520
1500
1480
1460
1440
1420
1400
0
20
40
60
80
100
120
140
160
180

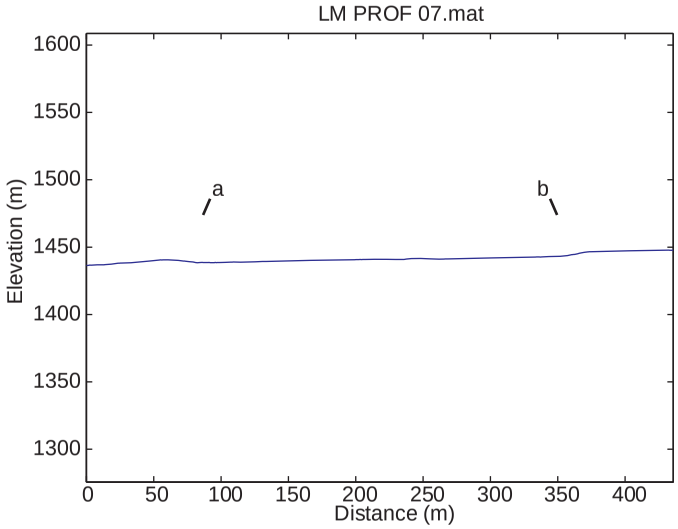
LM PROF 07.mat
Elevation (m)
Distance (m)
a
b
1600
1550
1500
1450
1400
1350
1300
0
50
100
150
200
250
300
350
400

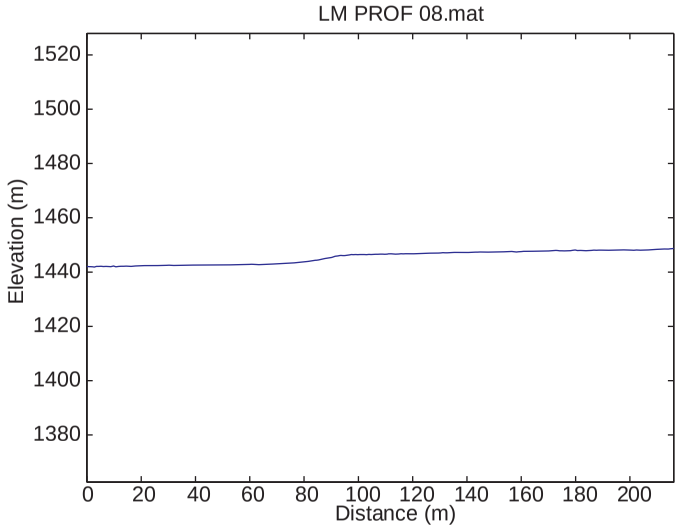
LM PROF 08.mat
Elevation (m)
Distance (m)
1520
1500
1480
1460
1440
1420
1400
1380
0
20
40
60
80
100
120
140
160
180
200

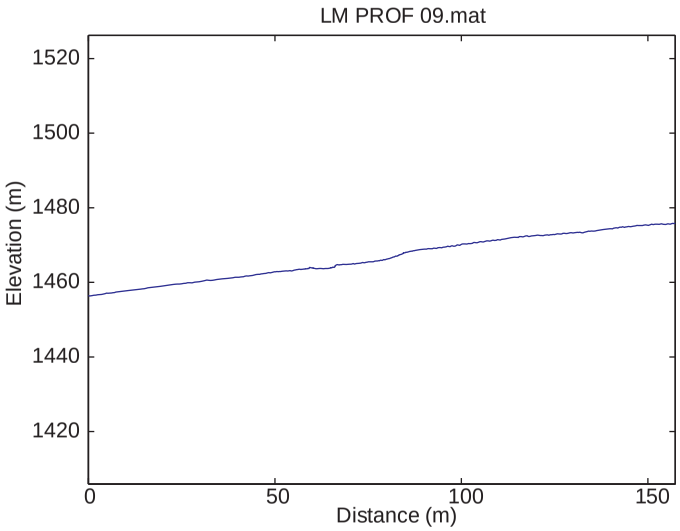
LM PROF 09.mat
Elevation (m)
1520
1500
1480
1460
1440
1420
0
50
100
150
Distance (m)

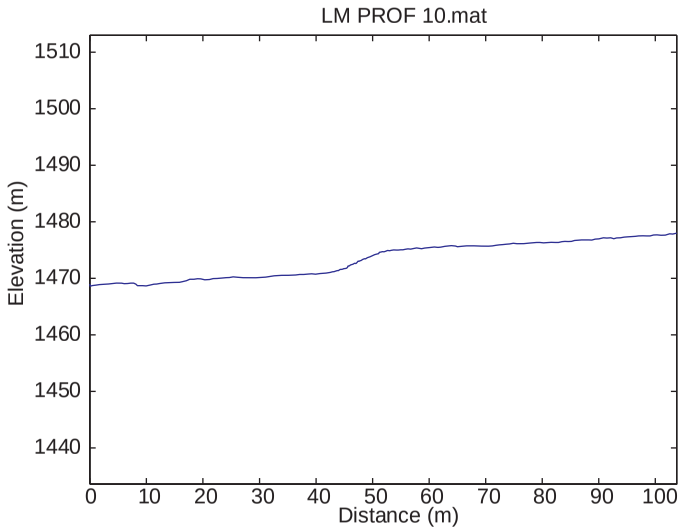
LM PROF 10.mat
Elevation (m)
1510
1500
1490
1480
1470
1460
1450
1440
0
10
20
30
40
50
60
70
80
90
100
Distance (m)

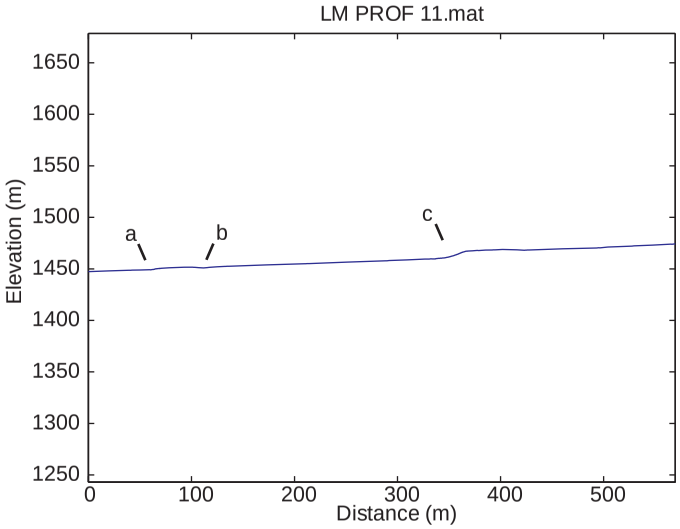
LM PROF 11.mat
Elevation (m)
1650
1600
1550
1500
1450
1400
1350
1300
1250
a
b
c
0
100
200
300
400
500
Distance (m)

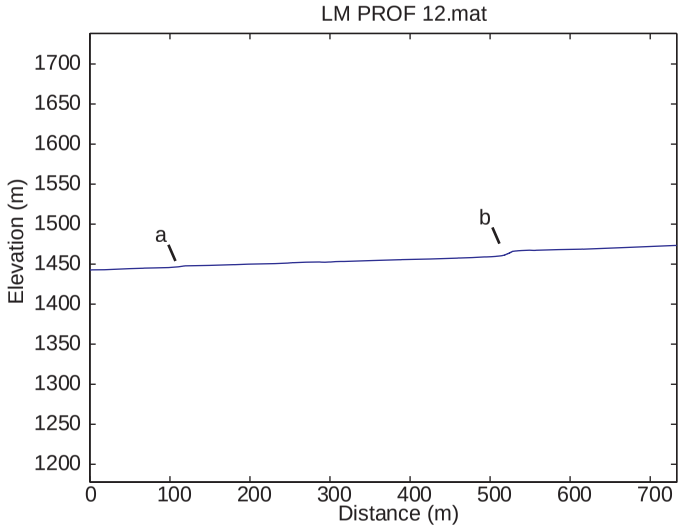
LM PROF 12.mat
Elevation (m)
1700
1650
1600
1550
1500
1450
1400
1350
1300
1250
1200
a
b
0
100
200
300
400
500
600
700
Distance (m)

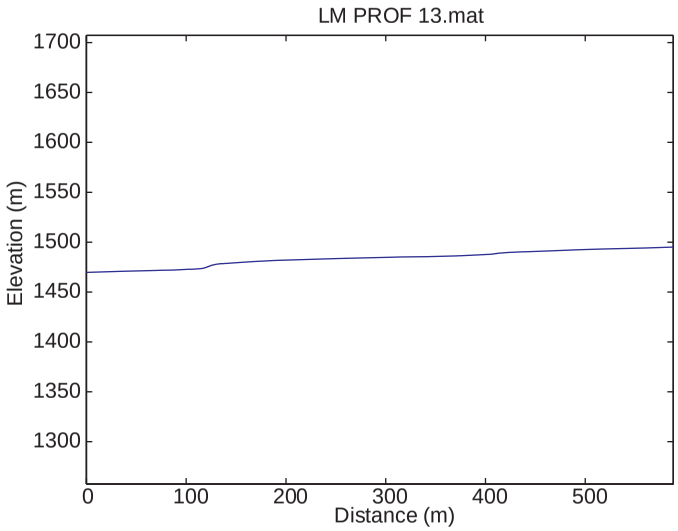
LM PROF 13.mat
Elevation (m)
Distance (m)
1700
1650
1600
1550
1500
1450
1400
1350
1300
0
100
200
300
400
500

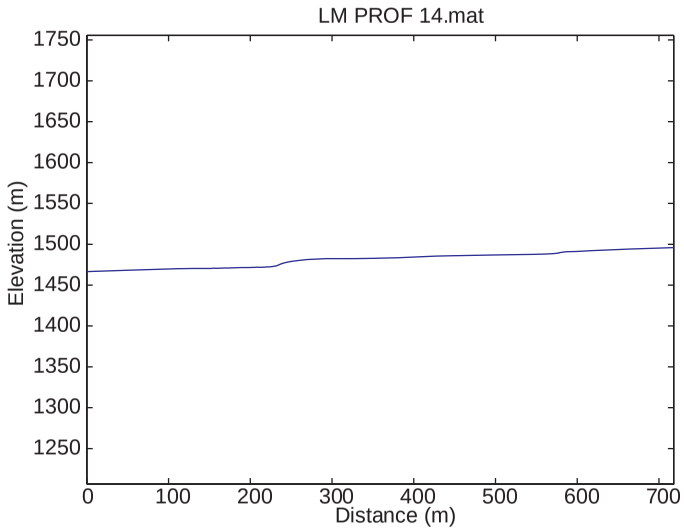
LM PROF 14.mat
Elevation (m)
Distance (m)
1750
1700
1650
1600
1550
1500
1450
1400
1350
1300
1250
0
100
200
300
400
500
600
700

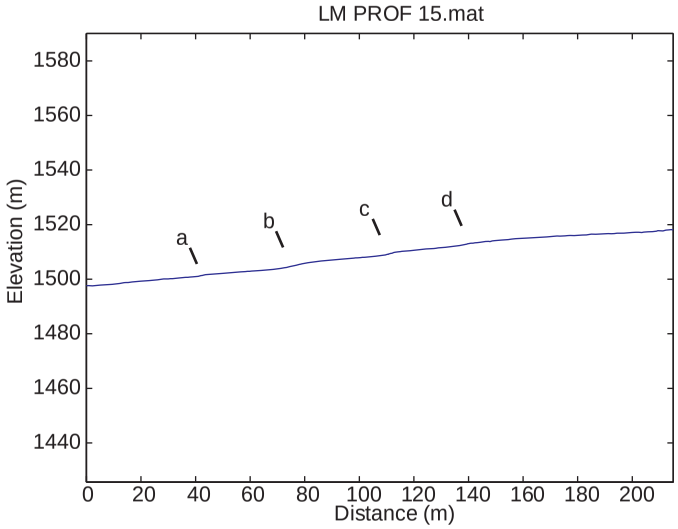
LM PROF 15.mat
Elevation (m)
Distance (m)
a
b
c
d
1580
1560
1540
1520
1500
1480
1460
1440
0
20
40
60
80
100
120
140
160
180
200

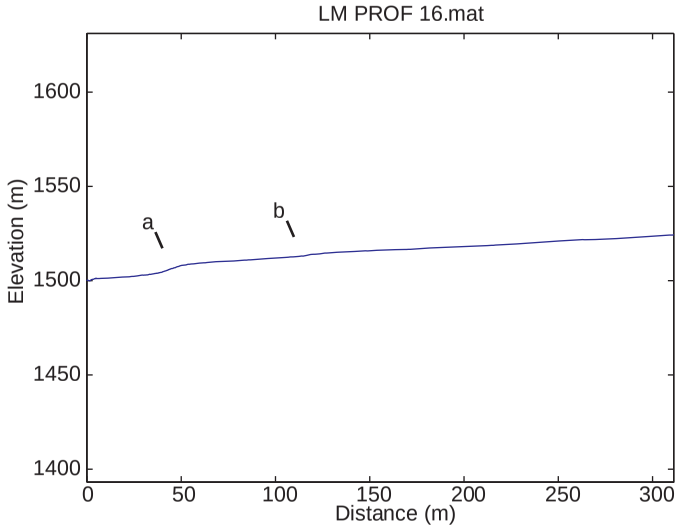
LM PROF 16.mat
Elevation (m)
Distance (m)
a
b
1600
1550
1500
1450
1400
0
50
100
150
200
250
300

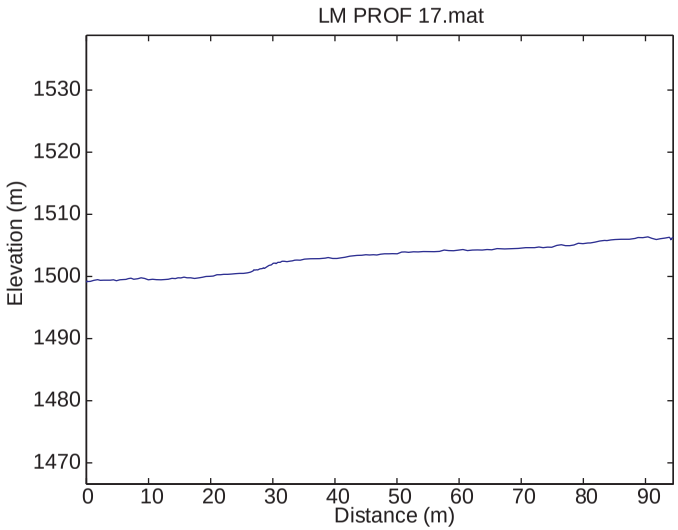
LM PROF 17.mat
Elevation (m)
1530
1520
1510
1500
1490
1480
1470
0
10
20
30
40
50
60
70
80
90
Distance (m)

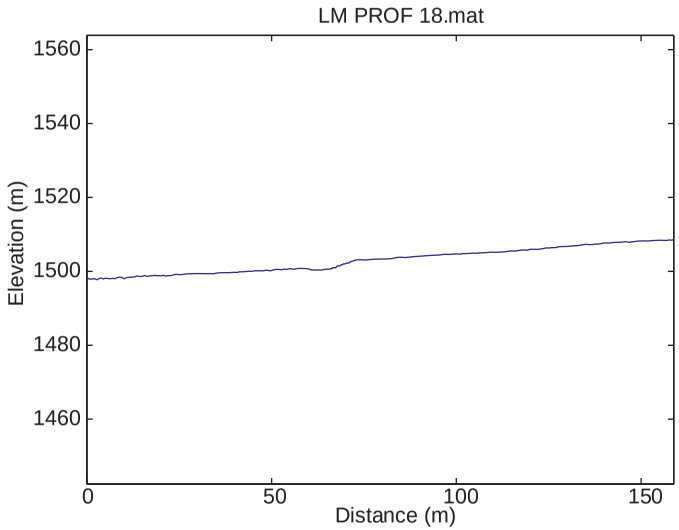
LM PROF 18.mat
Elevation (m)
1560
1540
1520
1500
1480
1460
0
50
100
150
Distance (m)

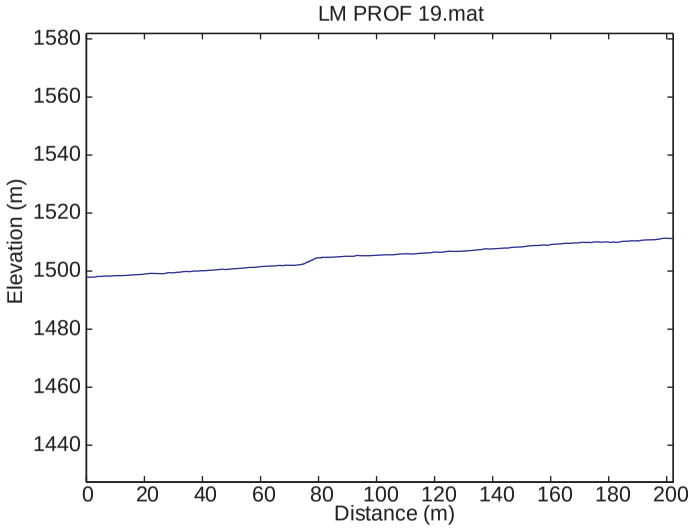
LM PROF 19.mat
Elevation (m)
1580
1560
1540
1520
1500
1480
1460
1440
0
20
40
60
80
100
120
140
160
180
200
Distance (m)

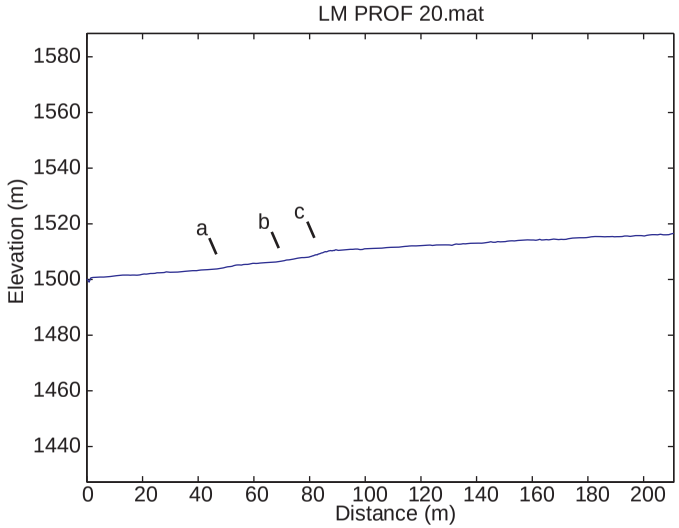
LM PROF 20.mat
Elevation (m)
1580
1560
1540
1520
1500
1480
1460
1440
a
b
c
0
20
40
60
80
100
120
140
160
180
200
Distance (m)

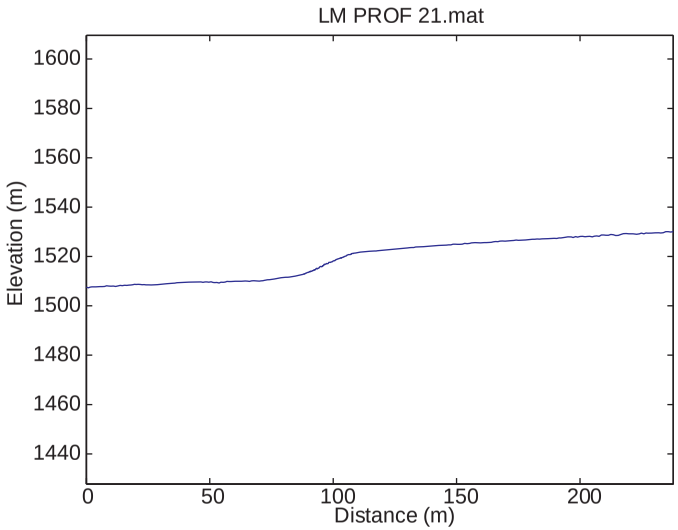
LM PROF 21.mat
Elevation (m)
1600
1580
1560
1540
1520
1500
1480
1460
1440
0
50
100
150
200
Distance (m)

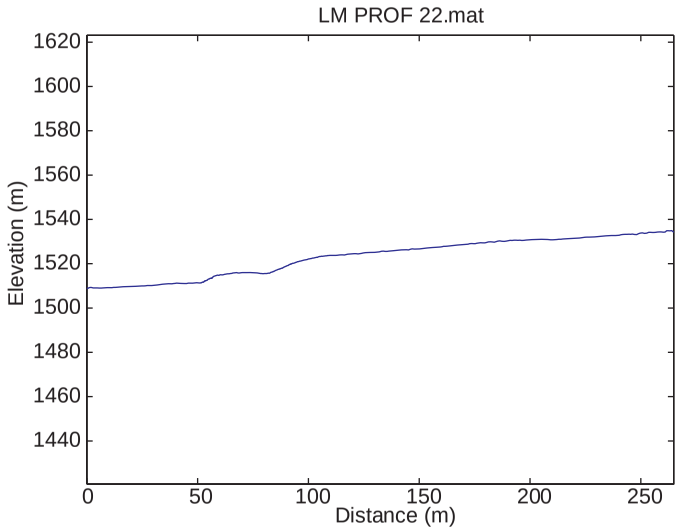
LM PROF 22.mat
Elevation (m)
1620
1600
1580
1560
1540
1520
1500
1480
1460
1440
0
50
100
150
200
250
Distance (m)

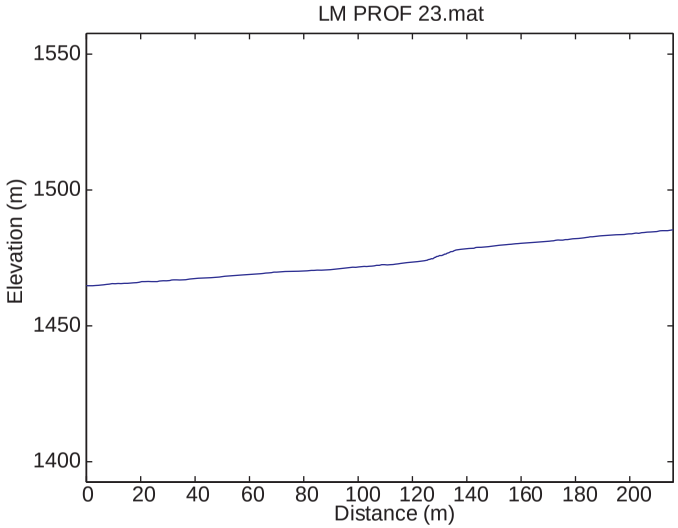
LM PROF 23.mat
Elevation (m)
1550
1500
1450
1400
0
20
40
60
80
100
120
140
160
180
200
Distance (m)

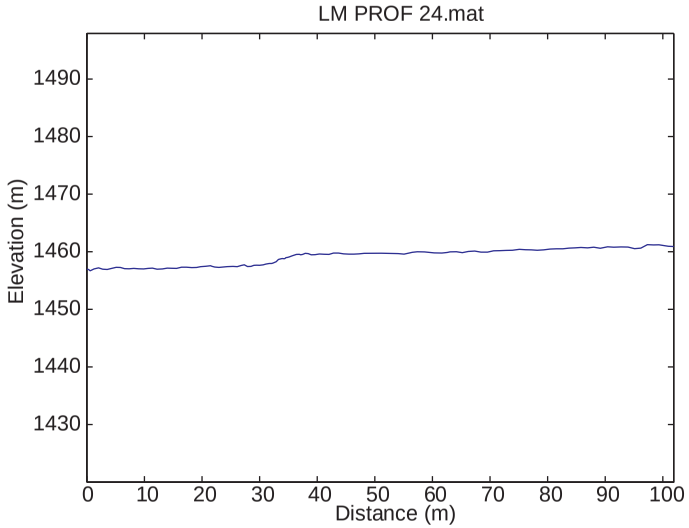
LM PROF 24.mat
Elevation (m)
1490
1480
1470
1460
1450
1440
1430
0
10
20
30
40
50
60
70
80
90
100
Distance (m)

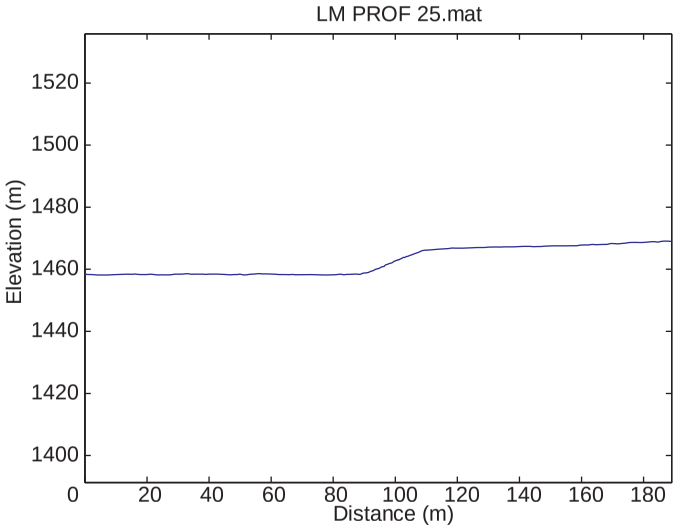
LM PROF 25.mat
Elevation (m)
1520
1500
1480
1460
1440
1420
1400
0
20
40
60
80
100
120
140
160
180
Distance (m)

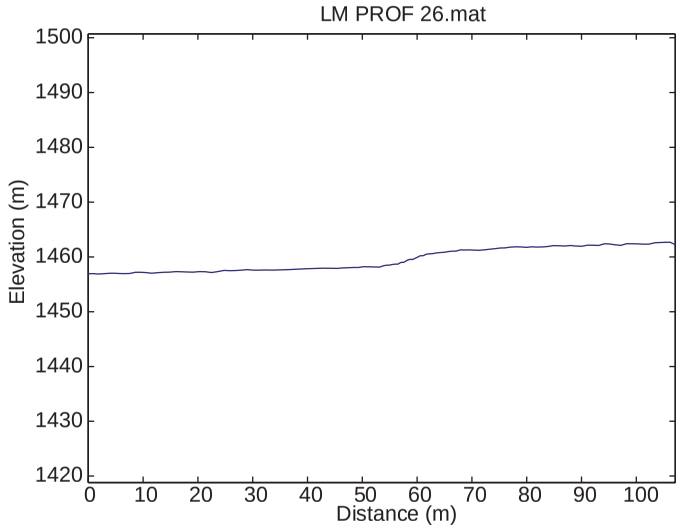
LM PROF 26.mat
Elevation (m)
1500
1490
1480
1470
1460
1450
1440
1430
1420
0
10
20
30
40
50
60
70
80
90
100
Distance (m)

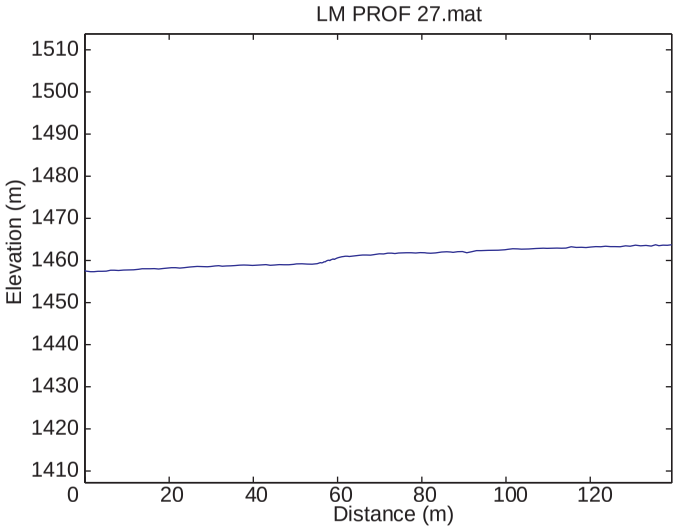
LM PROF 27.mat
Elevation (m)
1510
1500
1490
1480
1470
1460
1450
1440
1430
1420
1410
0
20
40
60
80
100
120
Distance (m)

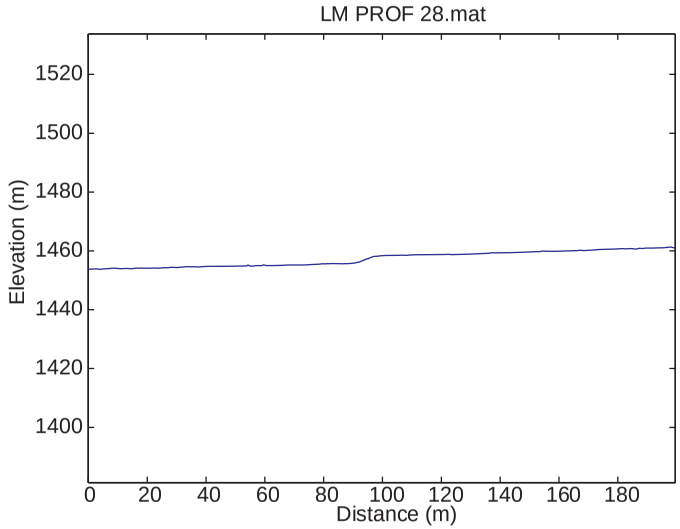
LM PROF 28.mat
Elevation (m)
1520
1500
1480
1460
1440
1420
1400
0
20
40
60
80
100
120
140
160
180
Distance (m)

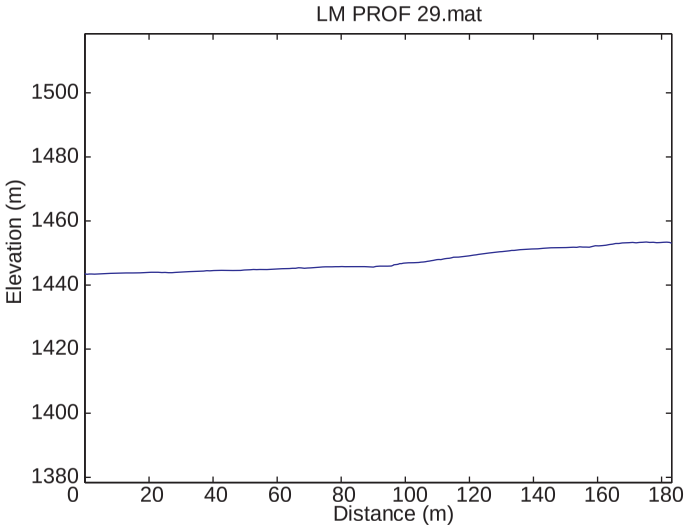
LM PROF 29.mat
Elevation (m)
1500
1480
1460
1440
1420
1400
1380
0
20
40
60
80
100
120
140
160
180
Distance (m)

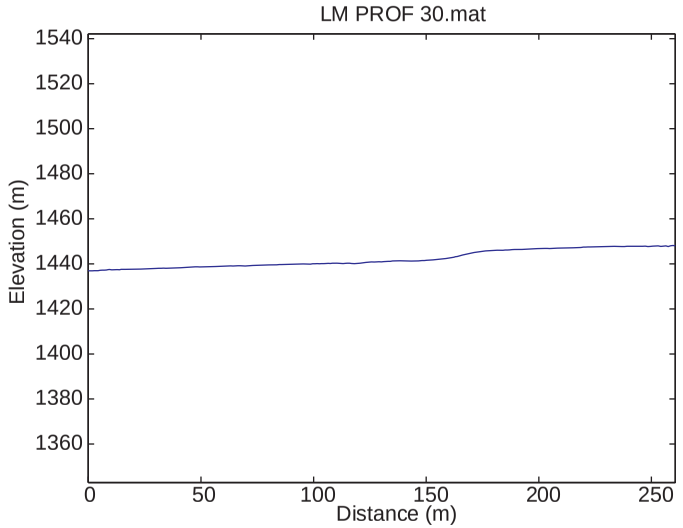
LM PROF 30.mat
Elevation (m)
1540
1520
1500
1480
1460
1440
1420
1400
1380
1360
0
50
100
150
200
250
Distance (m)

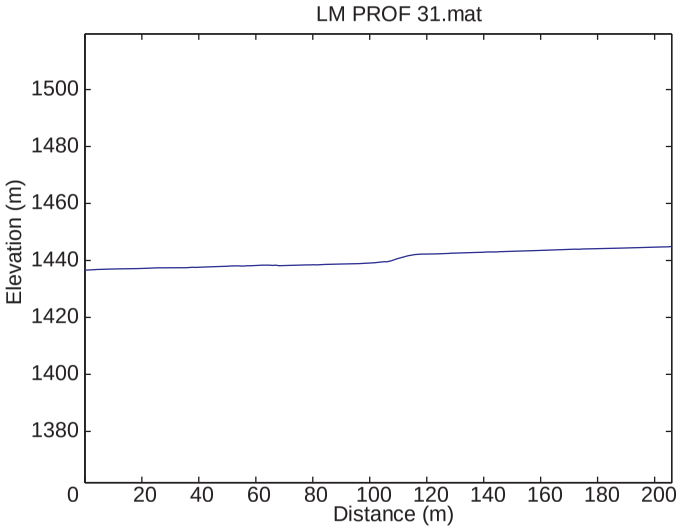
LM PROF 31.mat
Elevation (m)
1500
1480
1460
1440
1420
1400
1380
0
20
40
60
80
100
120
140
160
180
200
Distance (m)

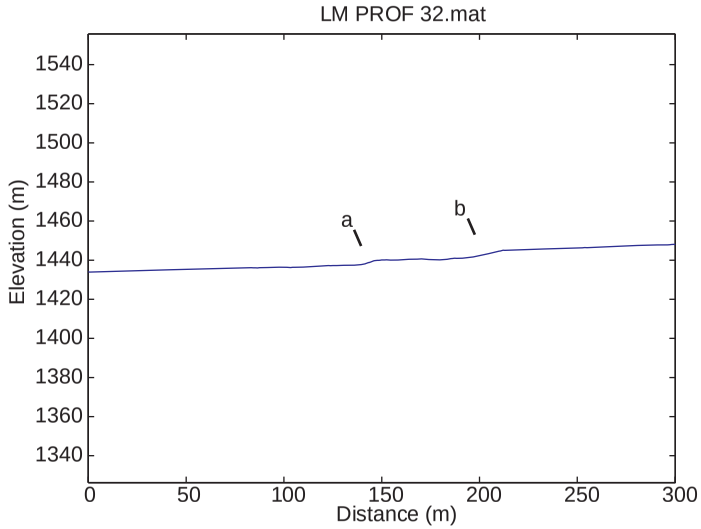
LM PROF 32.mat
Elevation (m)
1540
1520
1500
1480
1460
1440
1420
1400
1380
1360
1340
a
b
0
50
100
150
200
250
300
Distance (m)

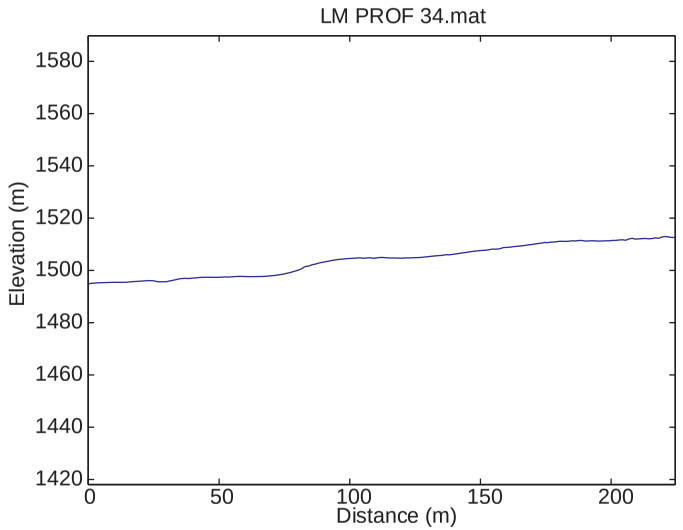
LM PROF 34.mat
Elevation (m)
1580
1560
1540
1520
1500
1480
1460
1440
1420
0
50
100
150
200
Distance (m)

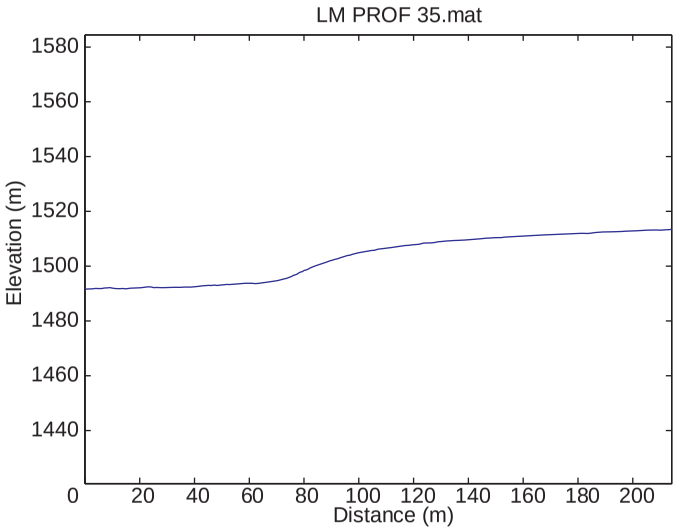
LM PROF 35.mat
Elevation (m)
1580
1560
1540
1520
1500
1480
1460
1440
0
20
40
60
80
100
120
140
160
180
200
Distance (m)

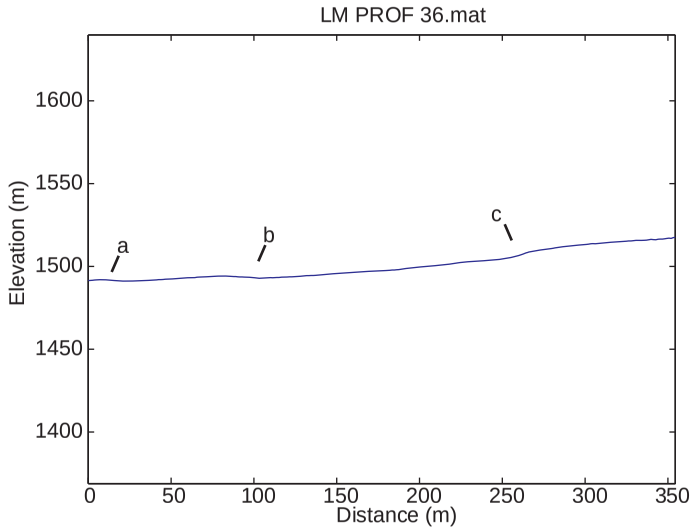
LM PROF 36.mat
Elevation (m)
1600
1550
1500
1450
1400
a
b
c
0
50
100
150
200
250
300
350
Distance (m)

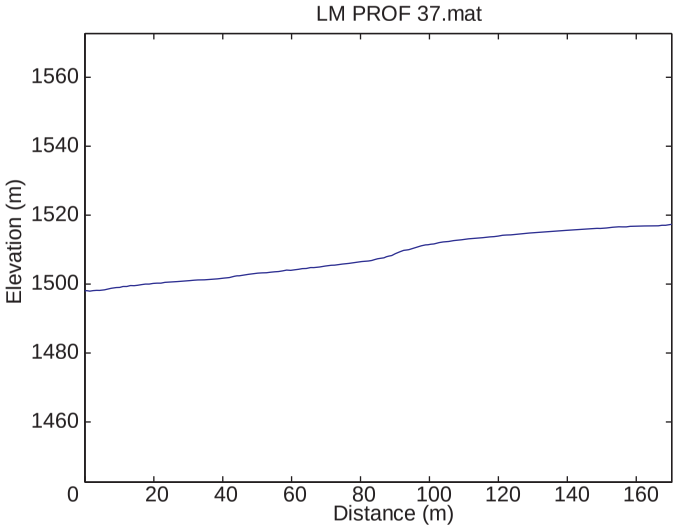
LM PROF 37.mat
Elevation (m)
Distance (m)
1560
1540
1520
1500
1480
1460
0
20
40
60
80
100
120
140
160

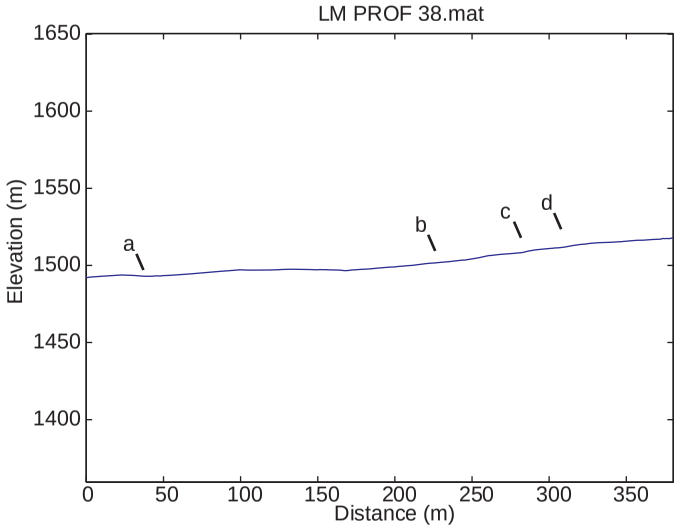
LM PROF 38.mat
Elevation (m)
Distance (m)
1650
1600
1550
1500
1450
1400
0
50
100
150
200
250
300
350
a
b
c
d

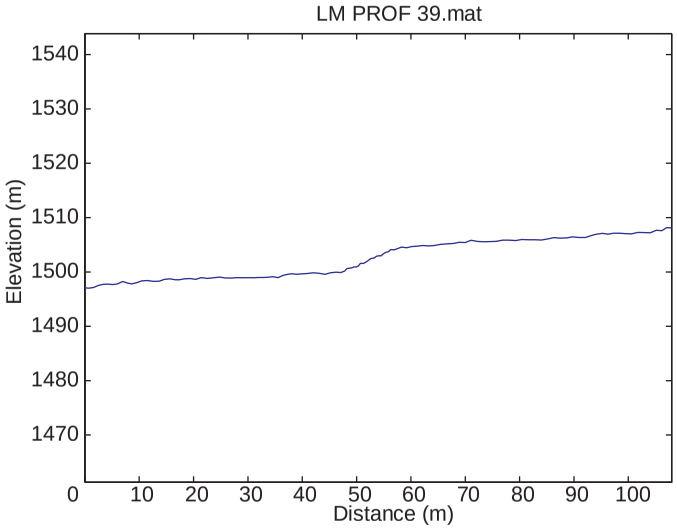
LM PROF 39.mat
Elevation (m)
Distance (m)
1540
1530
1520
1510
1500
1490
1480
1470
0
10
20
30
40
50
60
70
80
90
100

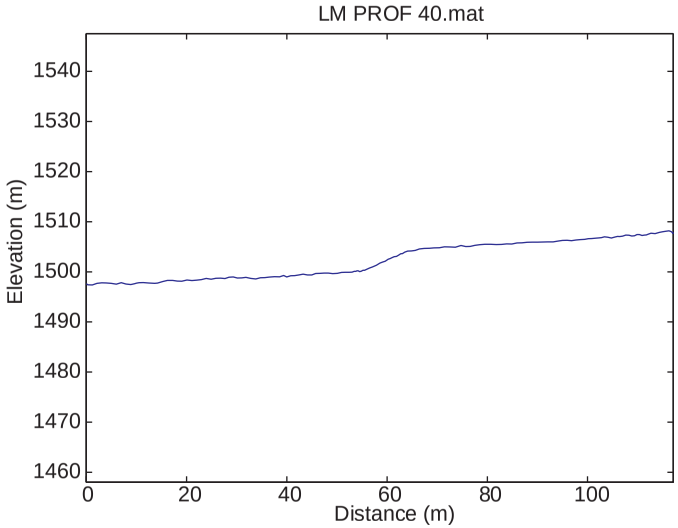
LM PROF 40.mat
Elevation (m)
Distance (m)
1540
1530
1520
1510
1500
1490
1480
1470
1460
0
20
40
60
80
100

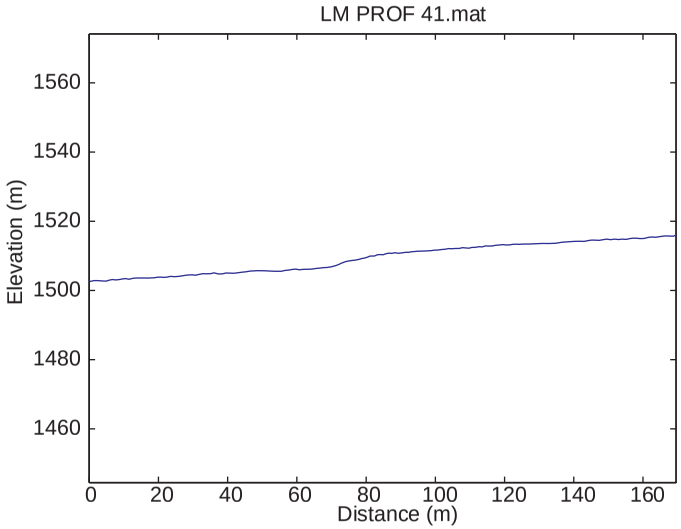
LM PROF 41.mat
Elevation (m)
1560
1540
1520
1500
1480
1460
0
20
40
60
80
100
120
140
160
Distance (m)

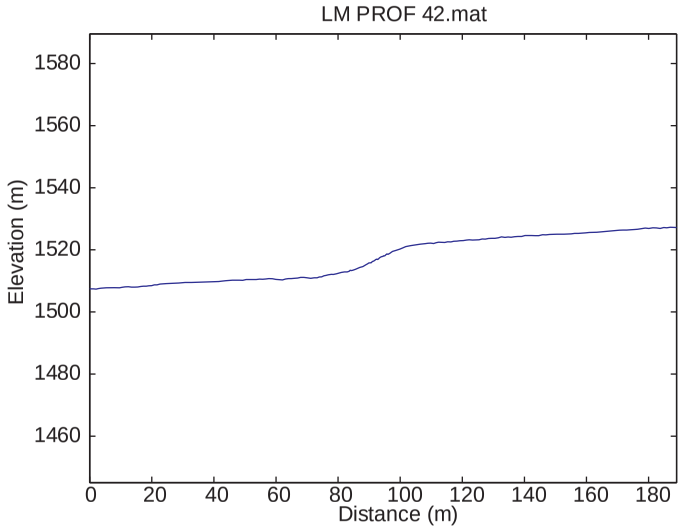
LM PROF 42.mat
Elevation (m)
1580
1560
1540
1520
1500
1480
1460
0
20
40
60
80
100
120
140
160
180
Distance (m)

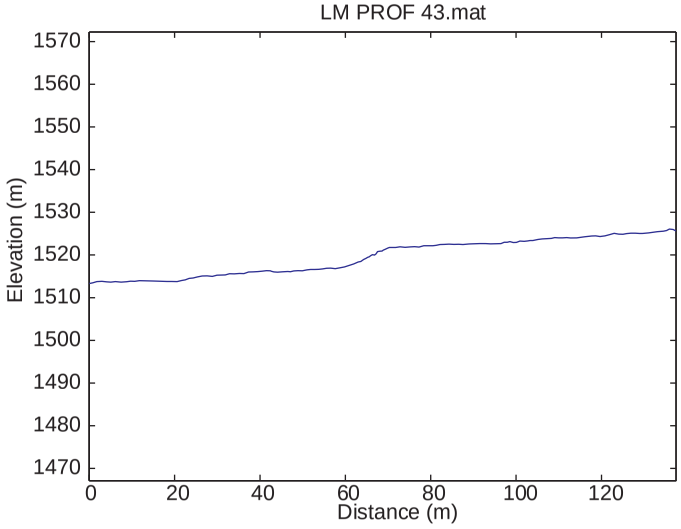
LM PROF 43.mat
Elevation (m)
1570
1560
1550
1540
1530
1520
1510
1500
1490
1480
1470
0
20
40
60
80
100
120
Distance (m)

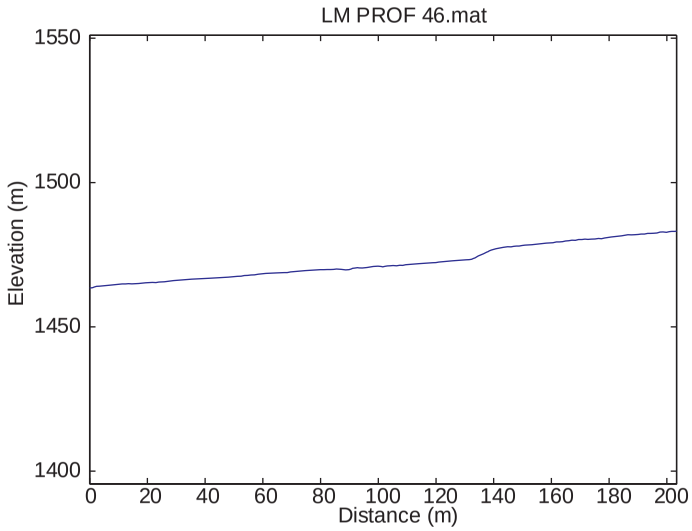
LM PROF 46.mat
Elevation (m)
Distance (m)
1550
1500
1450
1400
0
20
40
60
80
100
120
140
160
180
200

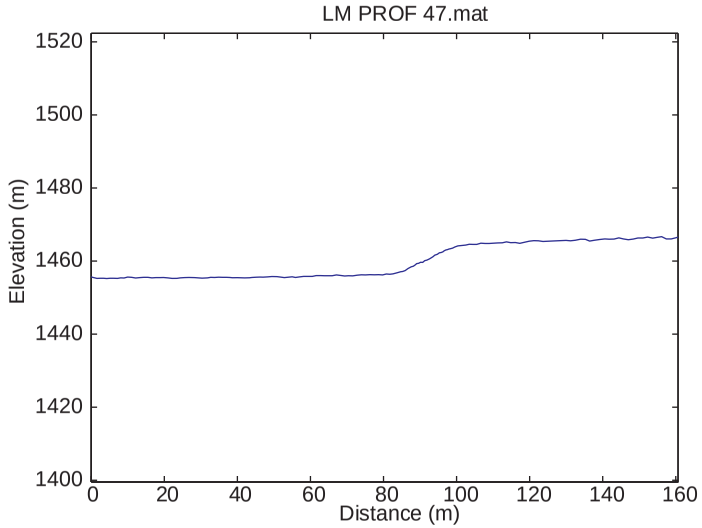
LM PROF 47.mat
Elevation (m)
Distance (m)
1520
1500
1480
1460
1440
1420
1400
0
20
40
60
80
100
120
140
160

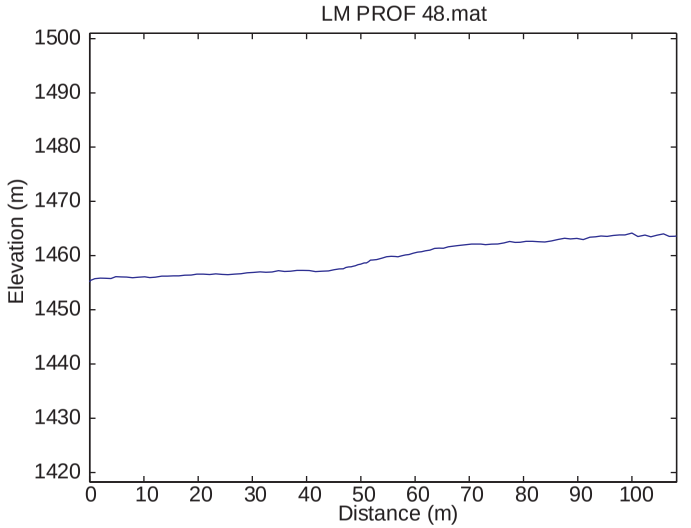
LM PROF 48.mat
Elevation (m)
Distance (m)
1500
1490
1480
1470
1460
1450
1440
1430
1420
0
10
20
30
40
50
60
70
80
90
100

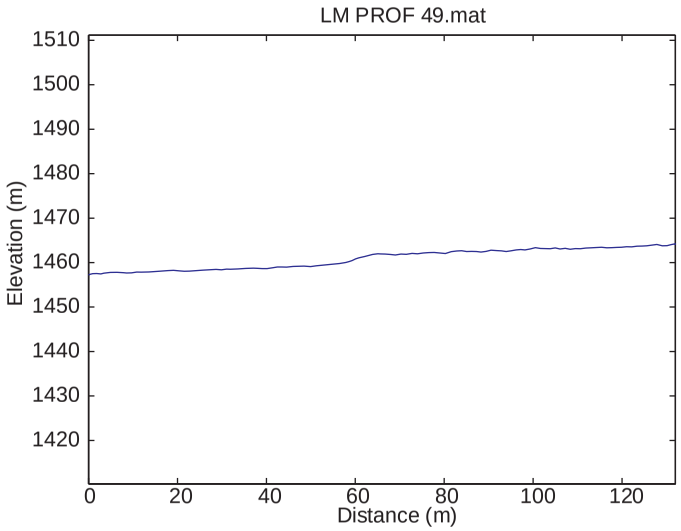
LM PROF 49.mat
Elevation (m)
Distance (m)
1510
1500
1490
1480
1470
1460
1450
1440
1430
1420
0
20
40
60
80
100
120

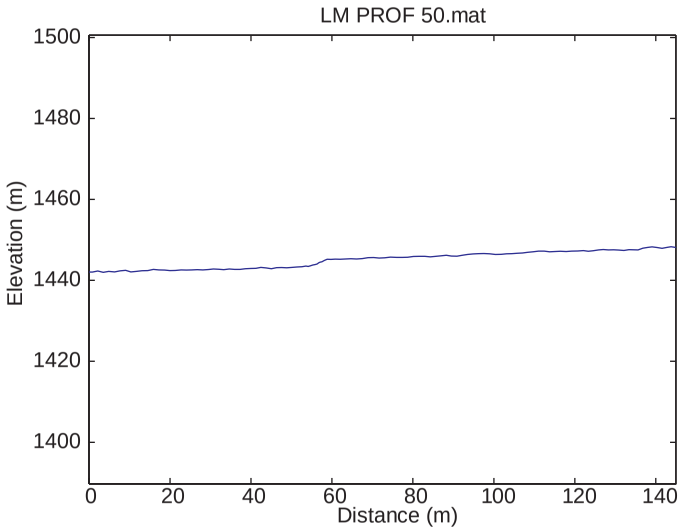
LM PROF 50.mat
Elevation (m)
Distance (m)
1500
1480
1460
1440
1420
1400
0
20
40
60
80
100
120
140

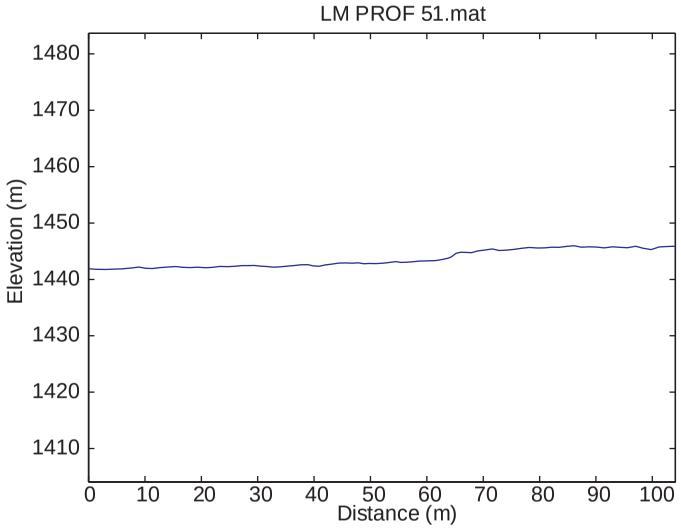
LM PROF 51.mat
Elevation (m)
Distance (m)
1480
1470
1460
1450
1440
1430
1420
1410
0
10
20
30
40
50
60
70
80
90
100

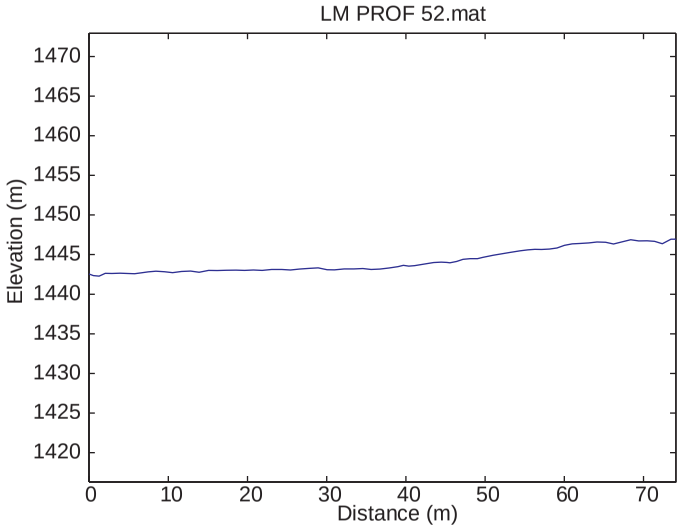
LM PROF 52.mat
Elevation (m)
Distance (m)
1470
1465
1460
1455
1450
1445
1440
1435
1430
1425
1420
0
10
20
30
40
50
60
70

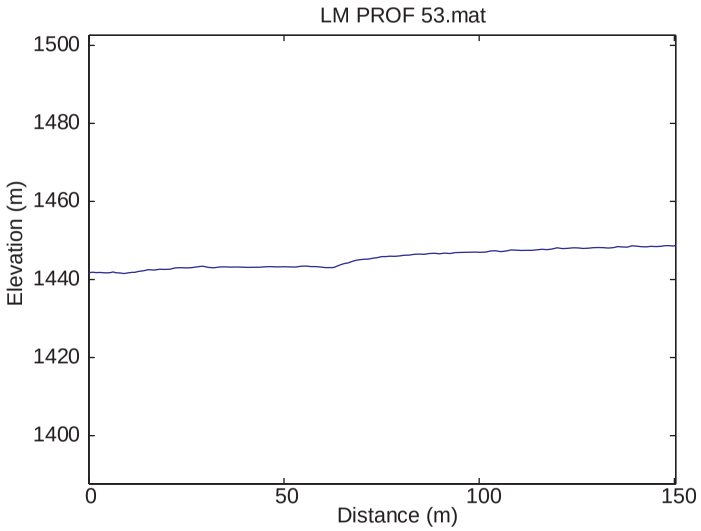
LM PROF 53.mat
Elevation (m)
Distance (m)
1500
1480
1460
1440
1420
1400
0
50
100
150

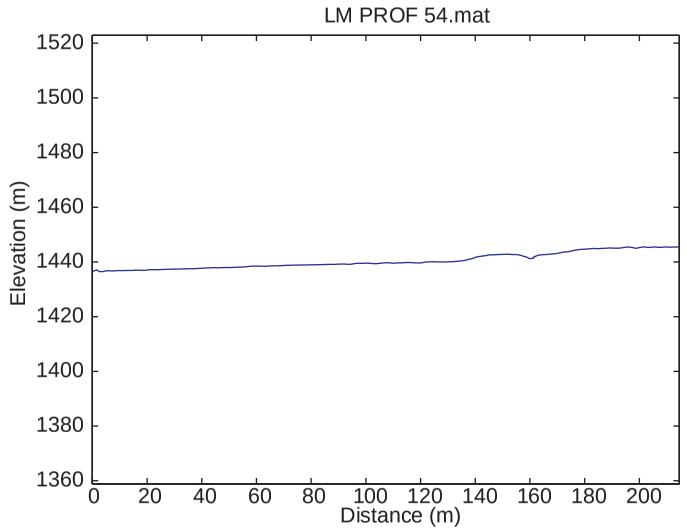
LM PROF 54.mat
Elevation (m)
Distance (m)
1520
1500
1480
1460
1440
1420
1400
1380
1360
0
20
40
60
80
100
120
140
160
180
200

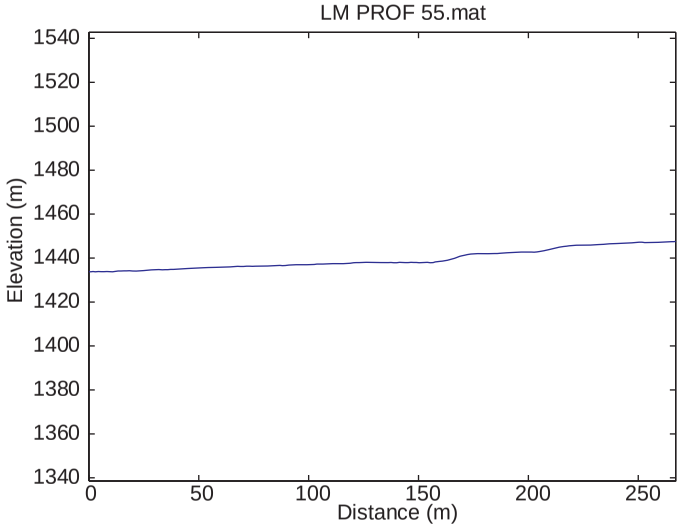
LM PROF 55.mat
Elevation (m)
Distance (m)
1540
1520
1500
1480
1460
1440
1420
1400
1380
1360
1340
0
50
100
150
200
250

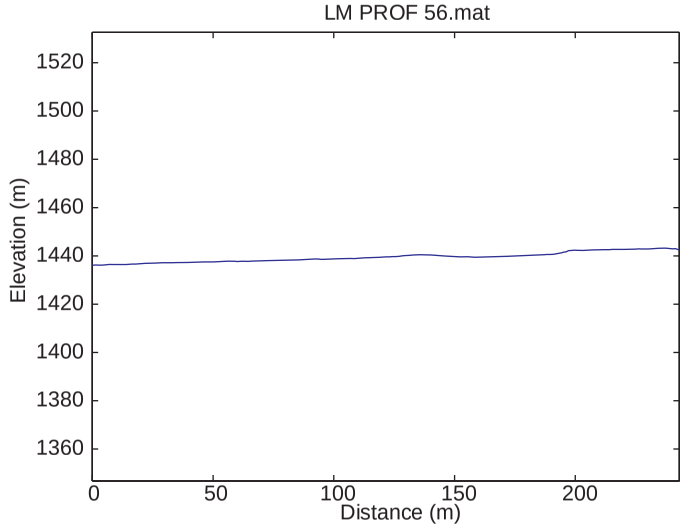
LM PROF 56.mat
Elevation (m)
Distance (m)
1520
1500
1480
1460
1440
1420
1400
1380
1360
0
50
100
150
200

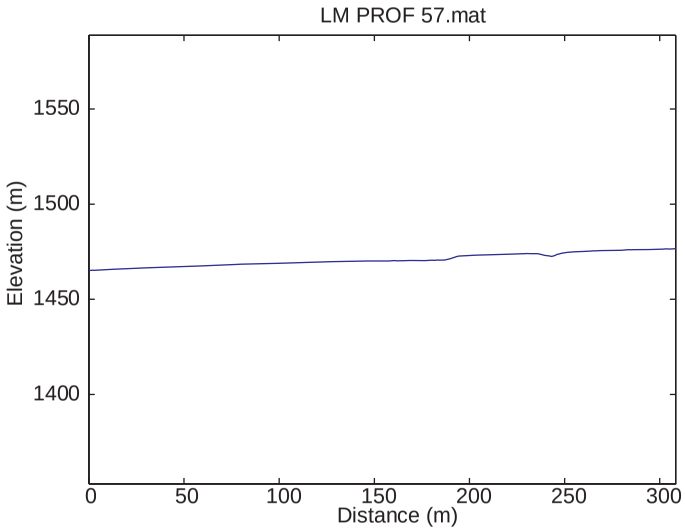
LM PROF 57.mat
Elevation (m)
1550
1500
1450
1400
0
50
100
150
200
250
300
Distance (m)

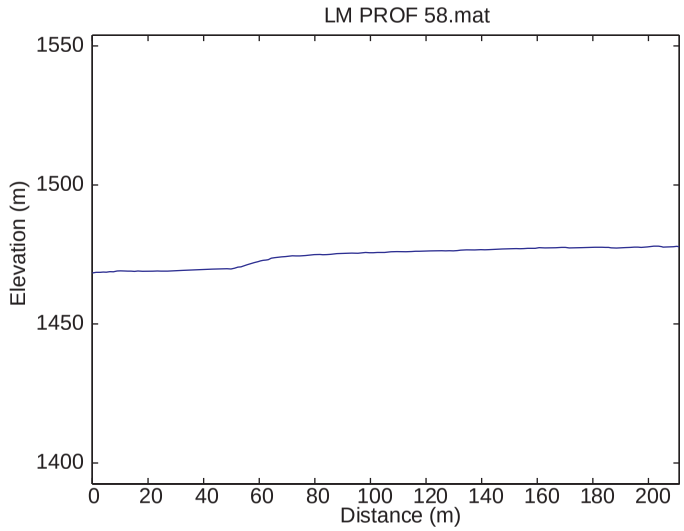
LM PROF 58.mat
Elevation (m)
1550
1500
1450
1400
0
20
40
60
80
100
120
140
160
180
200
Distance (m)

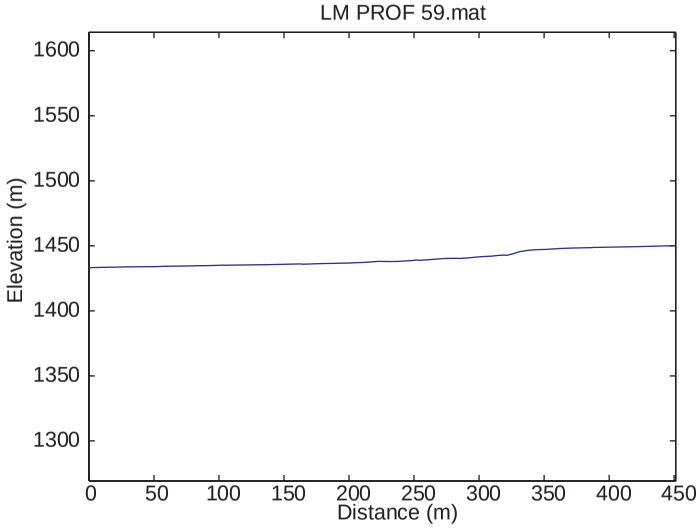
LM PROF 59.mat
Elevation (m)
1600
1550
1500
1450
1400
1350
1300
0
50
100
150
200
250
300
350
400
450
Distance (m)

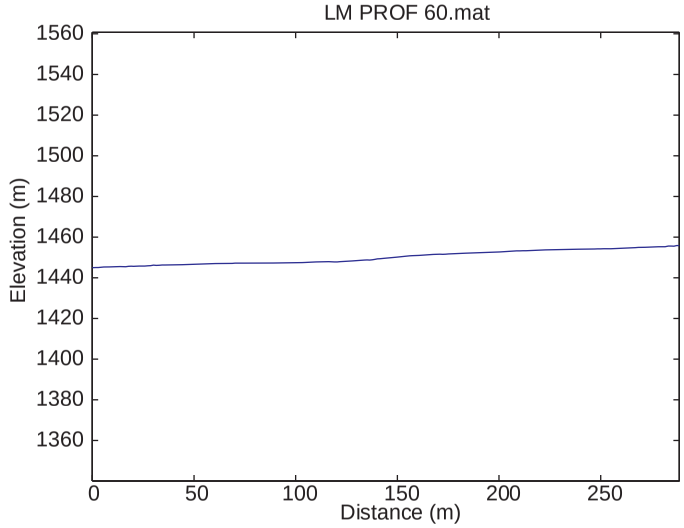
LM PROF 60.mat
Elevation (m)
1560
1540
1520
1500
1480
1460
1440
1420
1400
1380
1360
0
50
100
150
200
250
Distance (m)

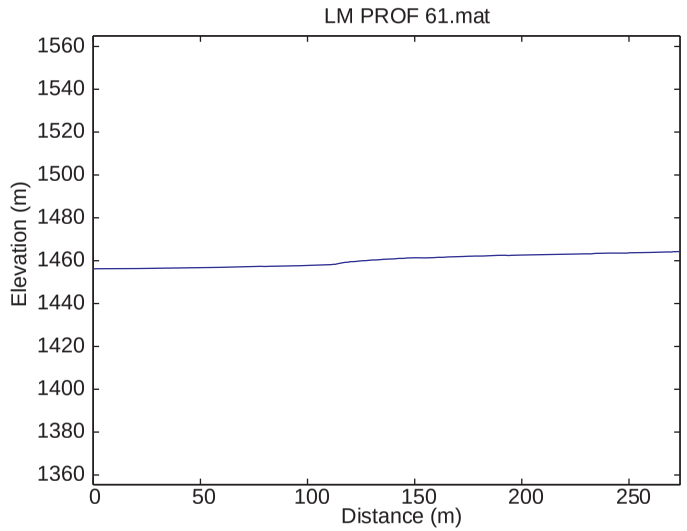
LM PROF 61.mat
Elevation (m)
Distance (m)
1560
1540
1520
1500
1480
1460
1440
1420
1400
1380
1360
0
50
100
150
200
250

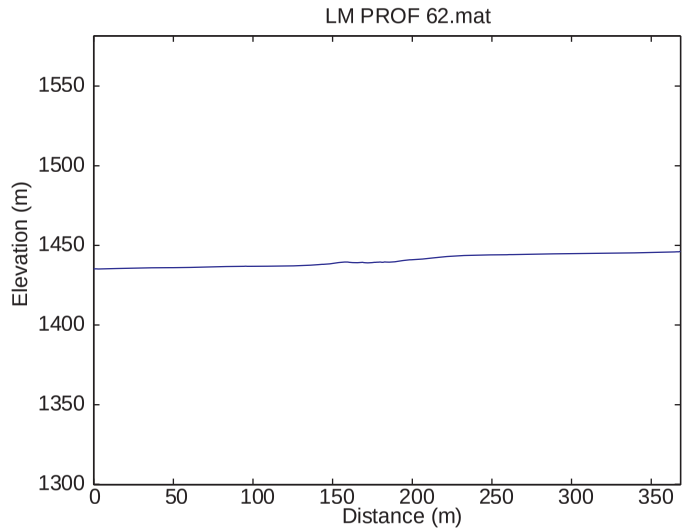
LM PROF 62.mat
Elevation (m)
Distance (m)
1550
1500
1450
1400
1350
1300
0
50
100
150
200
250
300
350

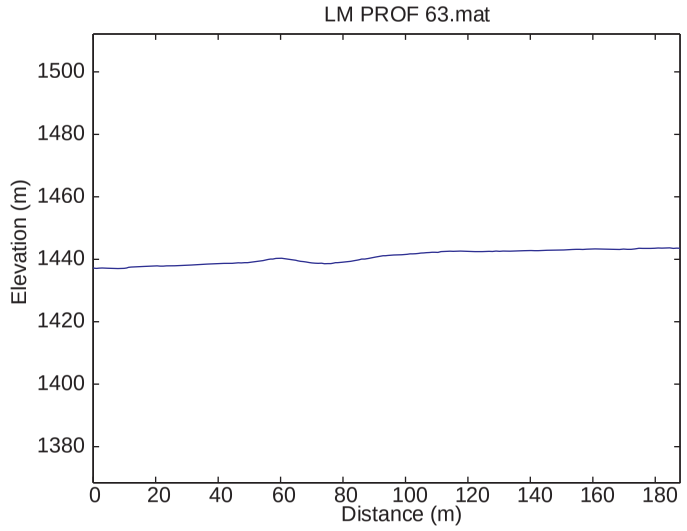
LM PROF 63.mat
Elevation (m)
Distance (m)
1500
1480
1460
1440
1420
1400
1380
0
20
40
60
80
100
120
140
160
180

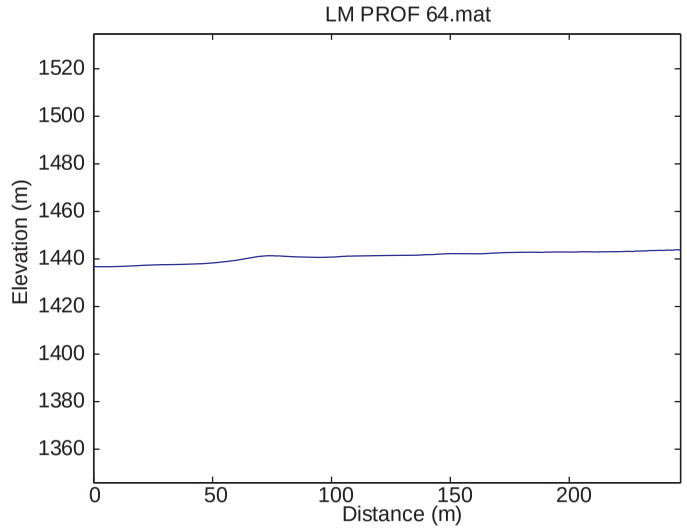
LM PROF 64.mat
Elevation (m)
Distance (m)
1520
1500
1480
1460
1440
1420
1400
1380
1360
0
50
100
150
200

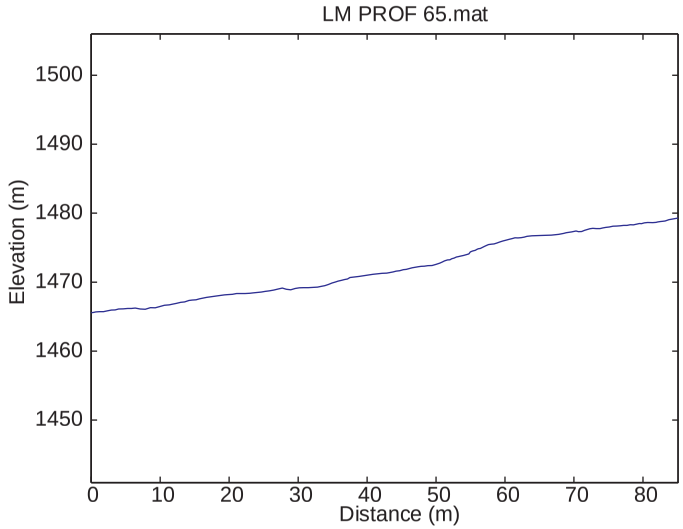
LM PROF 65.mat
Elevation (m)
1500
1490
1480
1470
1460
1450
0
10
20
30
40
50
60
70
80
Distance (m)

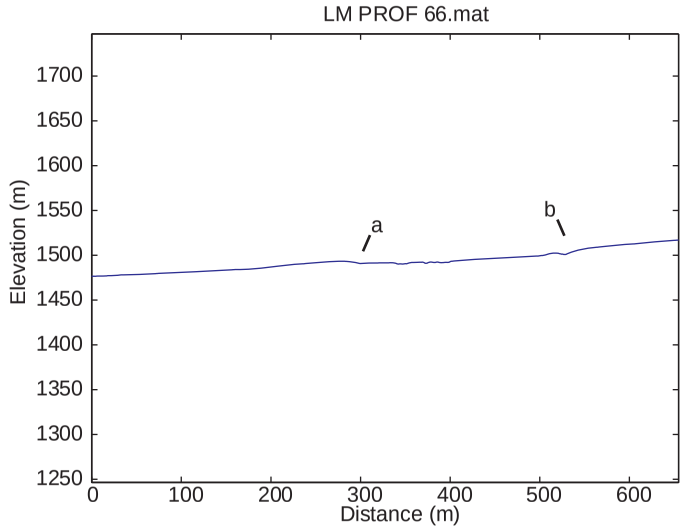
LM PROF 66.mat
Elevation (m)
1700
1650
1600
1550
1500
1450
1400
1350
1300
1250
a
b
0
100
200
300
400
500
600
Distance (m)

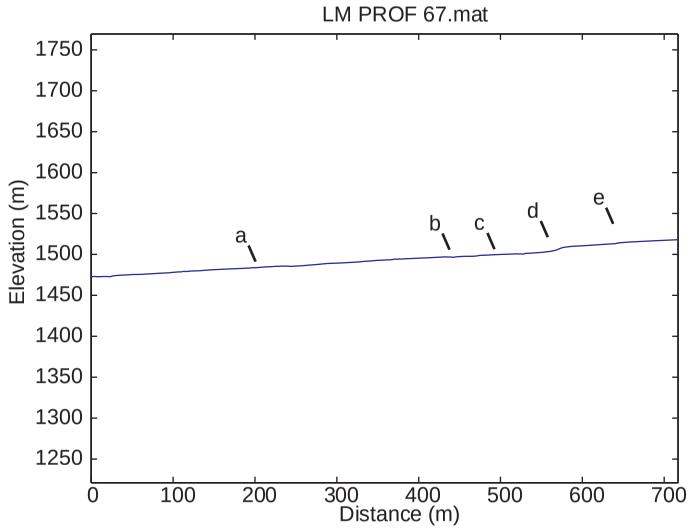
LM PROF 67.mat
Elevation (m)
1750
1700
1650
1600
1550
1500
1450
1400
1350
1300
1250
a
b
c
d
e
0
100
200
300
400
500
600
700
Distance (m)

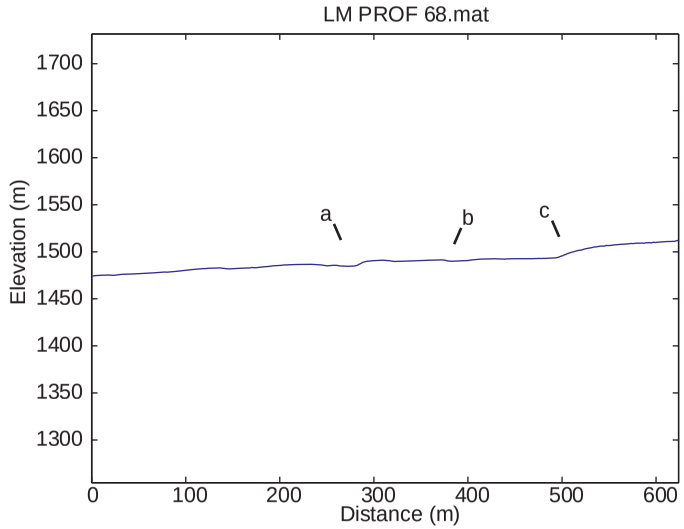
LM PROF 68.mat
Elevation (m)
1700
1650
1600
1550
1500
1450
1400
1350
1300
a
b
c
0
100
200
300
400
500
600
Distance (m)

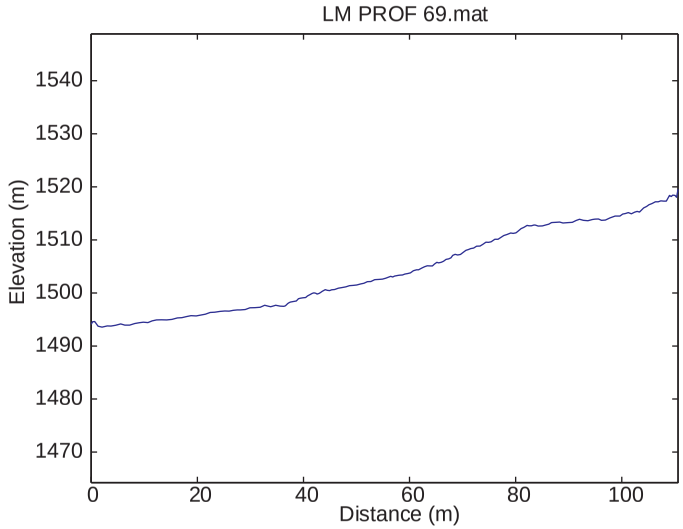
LM PROF 69.mat
Elevation (m)
1540
1530
1520
1510
1500
1490
1480
1470
0
20
40
60
80
100
Distance (m)

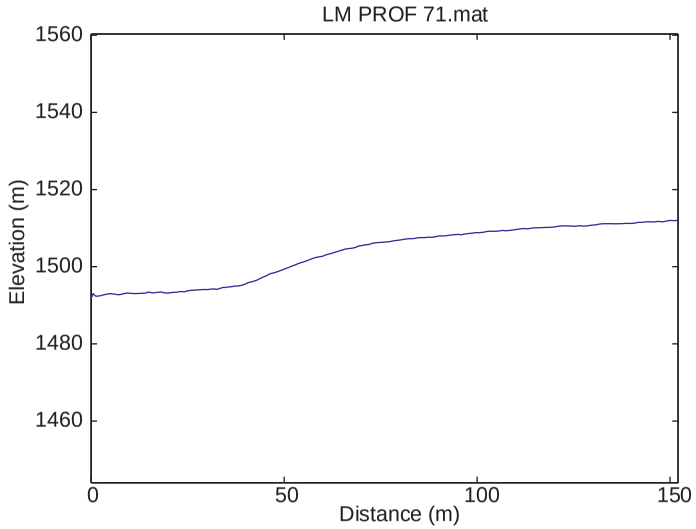
LM PROF 71.mat
Elevation (m)
1560
1540
1520
1500
1480
1460
0
50
100
150
Distance (m)

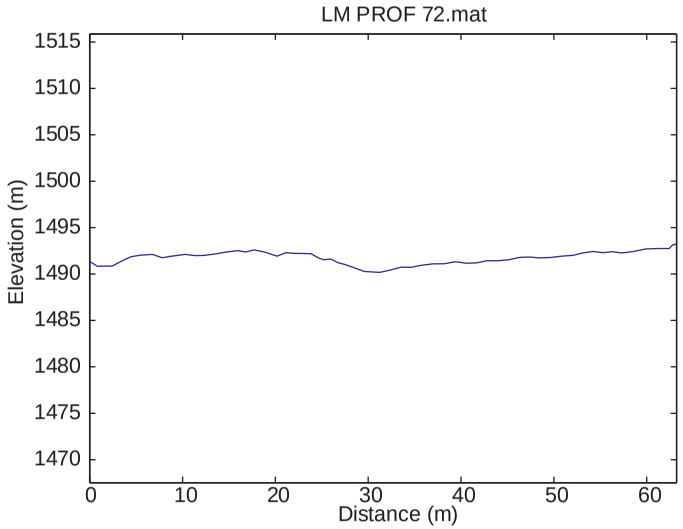
LM PROF 72.mat
Elevation (m)
1515
1510
1505
1500
1495
1490
1485
1480
1475
1470
0
10
20
30
40
50
60
Distance (m)

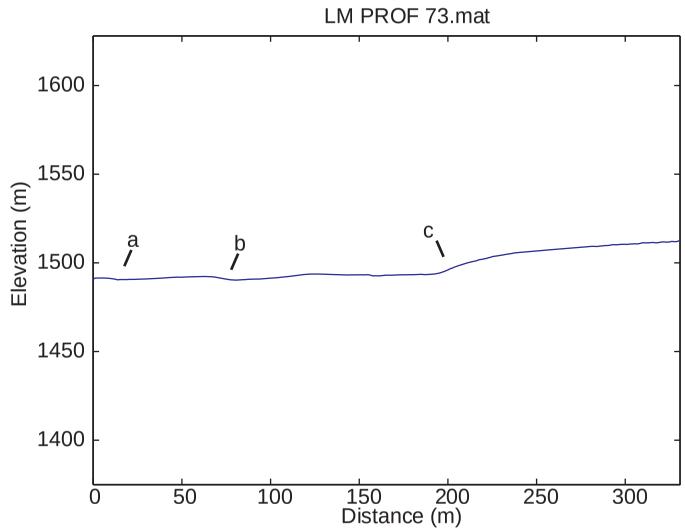
LM PROF 73.mat
Elevation (m)
Distance (m)
a
b
c

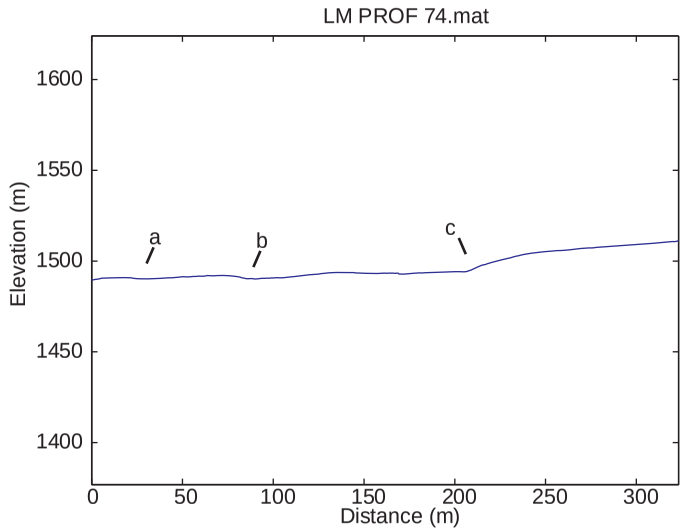
LM PROF 74.mat
Elevation (m)
Distance (m)
a
b
c

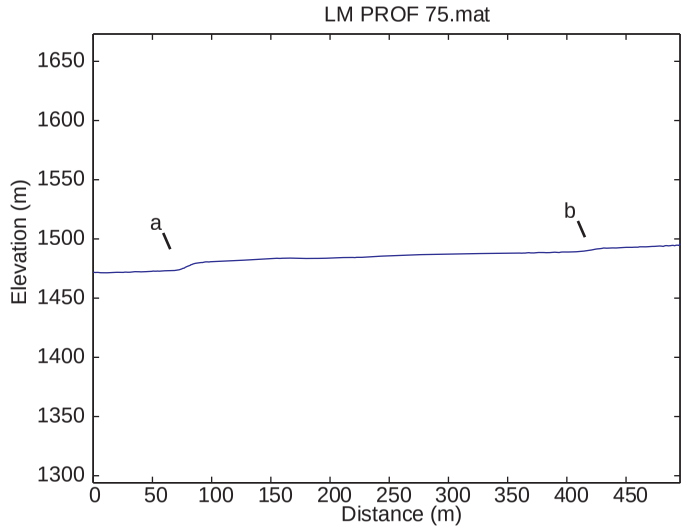
LM PROF 75.mat
Elevation (m)
Distance (m)
a
b

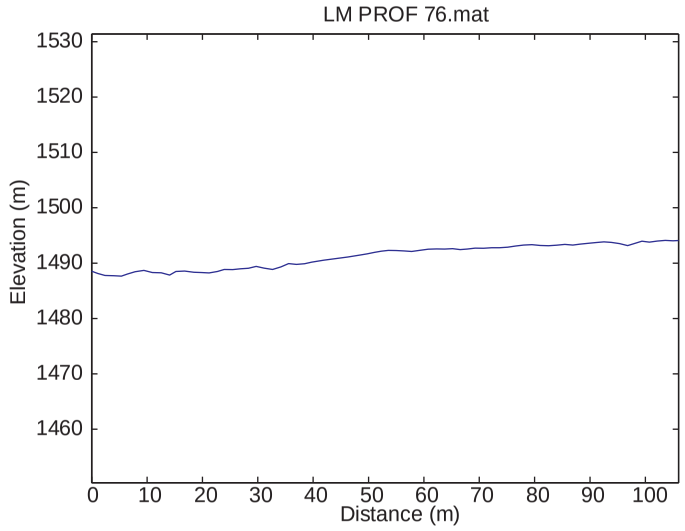
LM PROF 76.mat
Elevation (m)
Distance (m)

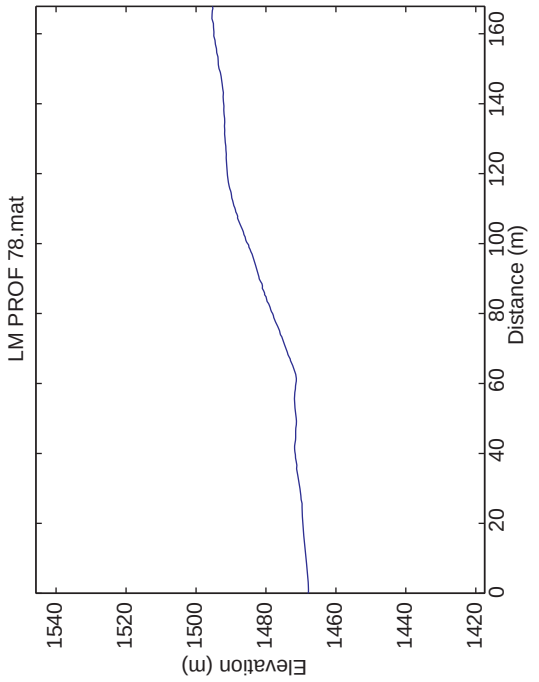
LM PROF 78.mat
Elevation (m)
Distance (m)
1540
1520
1500
1480
1460
1440
1420
0
20
40
60
80
100
120
140
160

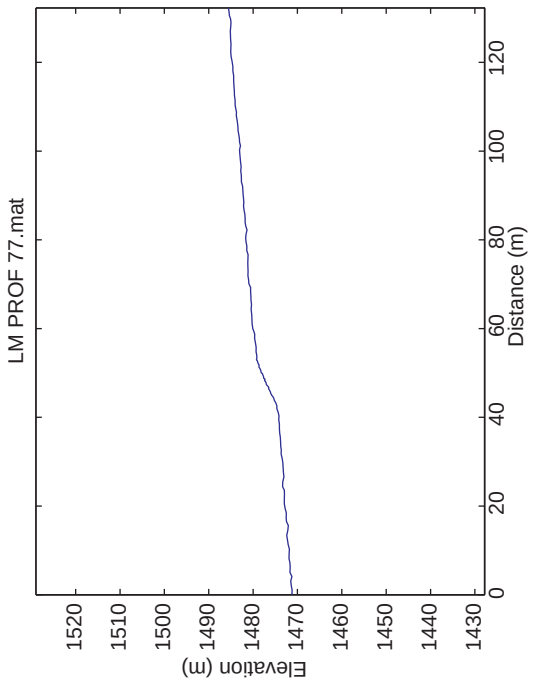
LM PROF 77.mat
Elevation (m)
Distance (m)
1520
1510
1500
1490
1480
1470
1460
1450
1440
1430
0
20
40
60
80
100
120

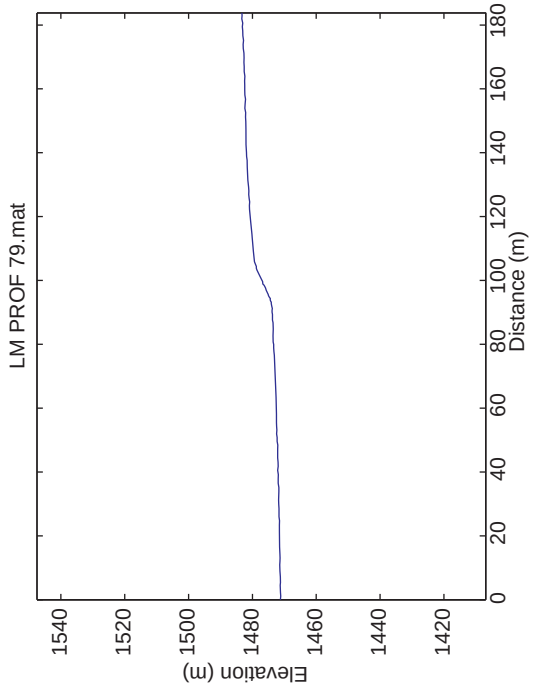
LM PROF 79.mat
Elevation (m)
Distance (m)
1540
1520
1500
1480
1460
1440
1420
0
20
40
60
80
100
120
140
160
180

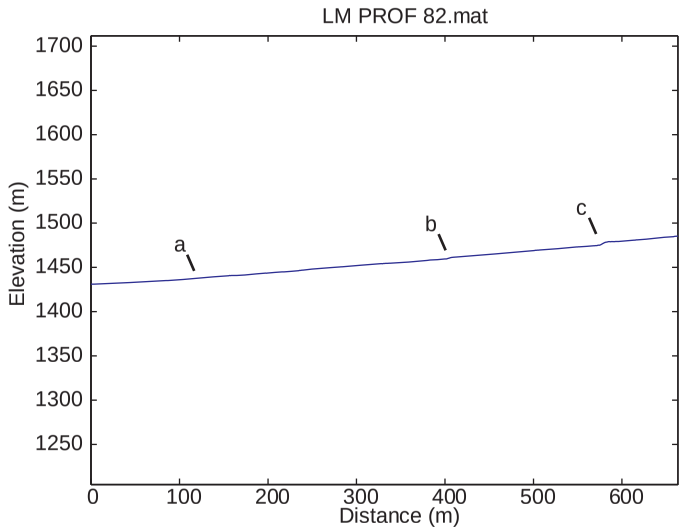
LM PROF 82.mat
Elevation (m)
Distance (m)
a
b
c

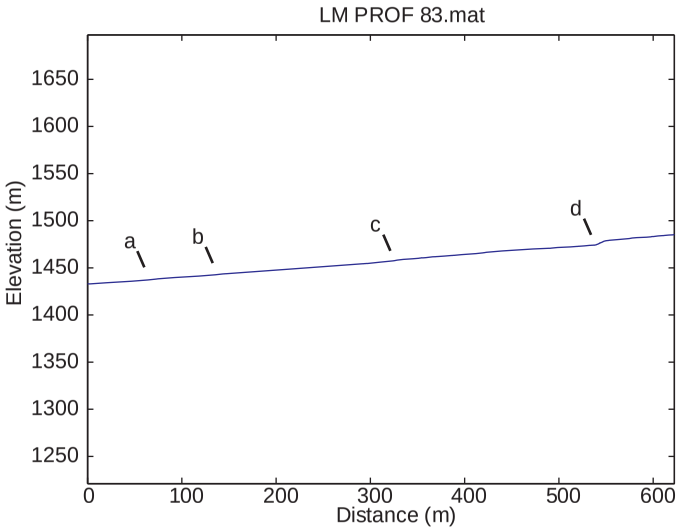
LM PROF 83.mat
Elevation (m)
Distance (m)
a
b
c
d

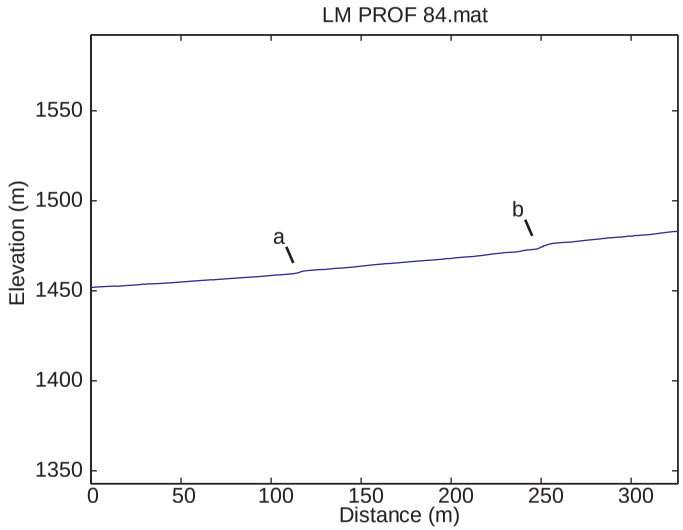
LM PROF 84.mat
Elevation (m)
Distance (m)
a
b

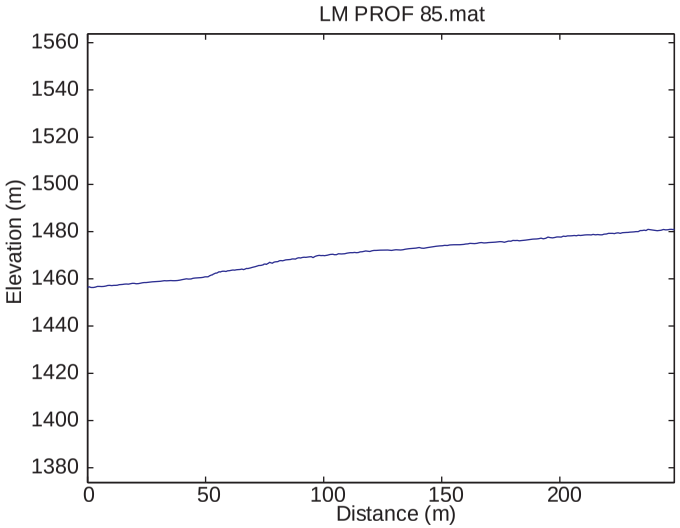
LM PROF 85.mat
Elevation (m)
Distance (m)
1560
1540
1520
1500
1480
1460
1440
1420
1400
1380
0
50
100
150
200

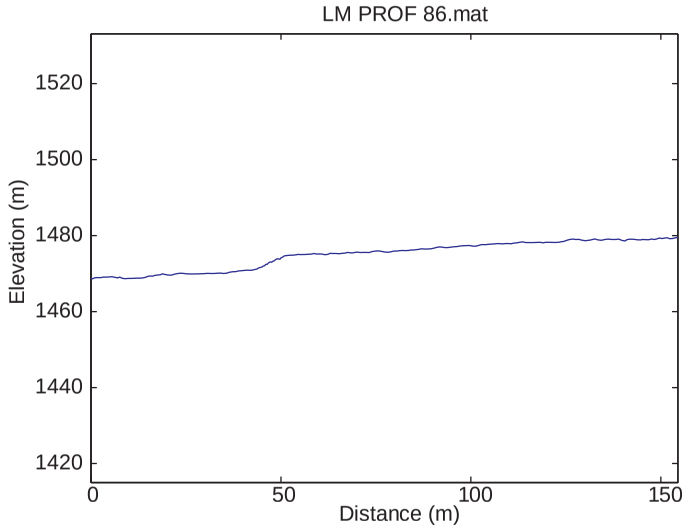
LM PROF 86.mat
Elevation (m)
Distance (m)
1520
1500
1480
1460
1440
1420
0
50
100
150

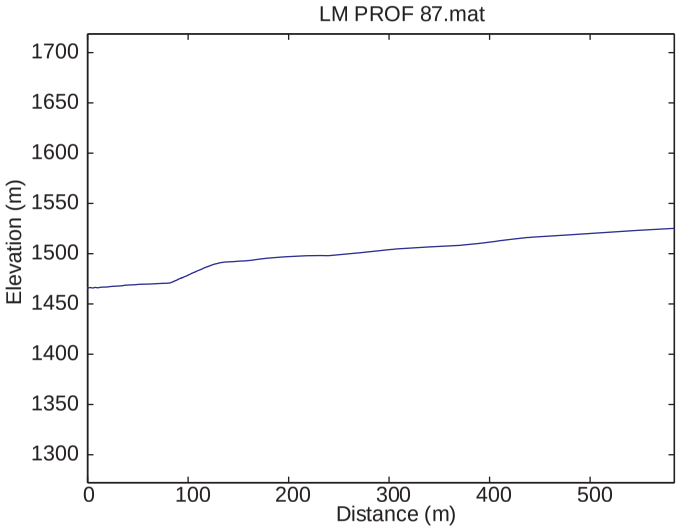
LM PROF 87.mat
Elevation (m)
Distance (m)
1700
1650
1600
1550
1500
1450
1400
1350
1300
0
100
200
300
400
500

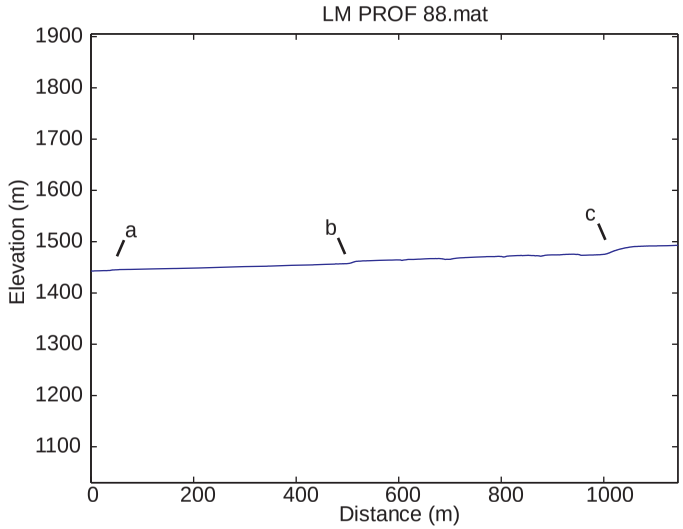
LM PROF 88.mat
Elevation (m)
Distance (m)
a
b
c
1900
1800
1700
1600
1500
1400
1300
1200
1100
0
200
400
600
800
1000

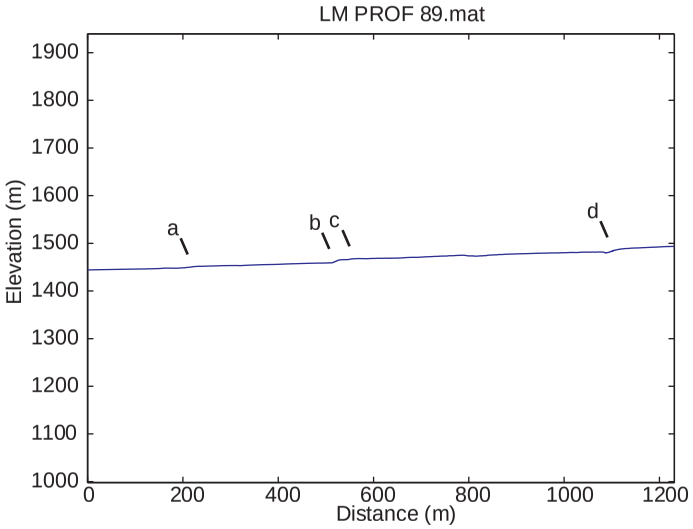
LM PROF 89.mat
Elevation (m)
1900
1800
1700
1600
1500
1400
1300
1200
1100
1000
0
200
400
600
800
1000
1200
Distance (m)
a
b
c
d

APPENDIX C

TOPOGRAPHIC PROFILE LOCATIONS AND SCARP ANALYSIS RESULTS

Appendix C. Topographic profile locations and scarp analysis results

Profile number	Scarp identifier	Northwest Longitude	Northwest Latitude	Southeast Longitude	Southeast Latitude	Elevation (m)	Distance from Southwest (km)[a]	Alluvial surface	Length of topographic profile (m)	Distance from end pt. to scarp (m)[b]	Assumed surface age (ka)[c]	kt (m^2)[d]	Scarp height (m)	Morphologic age (ka)[e]	Scarp angle (degrees)[f]	Comments
1	a	-117.625293	37.988742	-117.622493	37.987709	1450	11	Q2c	285	145	92	103	12	103	19	
2	a	-117.625517	37.987866	-117.623192	37.987389	1450	11	Q2c	215	129	92	71	9	71	17	
3	a	-117.627547	37.984393	-117.625502	37.983646	1454	10	Q2b	202	71	142	68	13.8	68	23	
4	a	-117.632628	37.979808	-117.631060	37.978297	1465	10	Q2c	218	34	92	6	2.2	6	22	
5	a	-117.626465	37.986228	-117.624411	37.985093	1456	11	Q2c	223	104	92	6	5.8	6	25	
6	a	-117.627739	37.983946	-117.625822	37.983067	1455	10	Q2b	198	65	142	77	7.6	77	22	
7	a	-117.676744	37.962335	-117.673281	37.959589	1437	5	Q2c	435	122	92		4		18	backfacing antithetic scarp
7	b						5	Q2c		357	92	26	3.5	26	12	
8	a	-117.674252	37.960933	-117.672584	37.959531	1442	5	Q2c	216	76	92	19	2.8	19	9	
9	a	-117.569519	38.046036	-117.569255	38.044689	1456	19	Q3b	157	69	17	3	1.3	3	22	
10	a	-117.578536	38.038900	-117.577837	38.038213	1469	17	Q3b	103	45	17	5	3.2	5	22	
11	a	-117.607571	38.018651	-117.601636	38.016702	1447	14	Q2c	569	62	92	26	1.2	26	18	
11	c						14	Q2c		500	92		1.3		18	backfacing antithetic scarp
11	b						14	Q2c		347	92	26	7	26	22	
12	a	-117.607484	38.021580	-117.600843	38.018015	1443	14	Q2c	732	107	92	19	1.6	19	8	
12	b						14	Q2c		518	92	19	7	19	26	
13	a	-117.598253	38.020108	-117.592653	38.017282	1470	15	Q2c	588	125	92	13	4	13	21	
13	b						15	Q2c		393	92	6	1	6	11	
14	a	-117.598705	38.021130	-117.592136	38.017586	1466	15	Q2c	718	230	92	42	7.2	42	18	
14	b						15	Q2c		574	92	13	1.9	13	13	
15	a	-117.586309	38.024268	-117.584102	38.023559	1498	16	Q2c	214	38	92		0.5		15	scarp difficult to see
15	b						16	Q2c		70	92		0.38		13	scarp difficult to see
15	c						16	Q2c		108	92	6	1.4	6	19	
15	d						16	Q2c		140	92	6	0.8	6	21	
16	a	-117.585708	38.024672	-117.583003	38.022996	1500	16	Q2c	311	38	92	13	3.6	13	20	
16	b						16	Q2c		117	92		0.52		23	not enough data points
17	a	-117.585785	38.025564	-117.584972	38.025086	1499	16	Q2c	94	26	92	6	1.8	6	19	
18	a	-117.586080	38.025884	-117.584382	38.025693	1498	16	Q2c	159	69	92	6	1.5	6	18	modified to take out drainage

Appendix C. Topographic profile locations and scarp analysis results

Profile number	Scarp identifier	Northwest Longitude	Northwest Latitude	Southeast Longitude	Southeast Latitude	Elevation (m)	Distance from Southwest (km)[a]	Alluvial surface	Length of topographic profile (m)	Distance from end pt. to scarp (m)[b]	Assumed surface age (ka)[c]	kt (m^2)[d]	Scarp height (m)	Morphologic age (ka)[e]	Scarp angle (degrees)[f]	Comments
19	a	-117.585858	38.026375	-117.583716	38.025847	1498	16	Q2c	202	77	92	6	2.1	6	26	modified to take out drainage
20	a	-117.583658	38.028641	-117.581396	38.028236	1500	16	Q2c	210	52	92	187	0.84	187	13	
20	b						16	Q2c		72	92	6	0.9	6	13	
20	c						16	Q2c		84	92	6	1.9	6	20	
21	a	-117.580760	38.030012	-117.578373	38.029254	1508	17	Q2c	237	89	92	26	8.6	26	23	
22	a	-117.578759	38.031886	-117.576522	38.030442	1509	17	Q2c	264	84	92	6	3.6	6	22	
23	a	-117.577290	38.042314	-117.575237	38.041331	1465	18	Q3b	216	123	17	6	3	6	19	
24	a	-117.606768	38.015443	-117.605957	38.014822	1457	14	Q2c	101	33	92		1.6		19	scarp difficult to see
25	a	-117.608435	38.014275	-117.606610	38.013431	1458	14	Q2c	188	87	92	19	8	19	22	
26	a	-117.612042	38.012166	-117.611062	38.011733	1457	13	Q2c	106	52	92	6	2.5	6	20	
27	a	-117.613826	38.009113	-117.612435	38.008564	1458	13	Q3b	138	57	17	3	1.6	3	15	
28	a	-117.616273	38.006986	-117.614323	38.006160	1454	13	Q2c	199	93	92	6	2.2	6	22	
29	a	-117.620889	38.005719	-117.619004	38.005055	1443	12	Q2c	182	95	92	142	4.8	142	15	
30	a	-117.622991	38.003288	-117.620127	38.002835	1437	12	Q2c	260	124	92	19	3.6	19	13	
31	a	-117.623971	37.999973	-117.621842	37.999383	1437	12	Q3b	205	108	17	6	2.5	6	18	
32	a	-117.625753	37.997360	-117.622698	37.996286	1434	11	Q2c	299	141	92	6	2.36	6	18	modified to take out drainage
32	b						11	Q2c		157	92	19	3.6	19	14	modified to take out drainage
34	a	-117.588401	38.021984	-117.586412	38.020745	1495	16	Q2c	224	81	92	52	5.6	52	19	
35	a	-117.587751	38.022715	-117.585916	38.021465	1492	16	Q2c	214	77	92	135	13.2	135	24	
36	a	-117.588558	38.023727	-117.584637	38.023095	1491	16	Q2c	353	33	92		1.8		12	back facing antithetic scarp
36	b						16	Q2c		100	92		2.6		7	back facing antithetic scarp
36	c						16	Q2c		266	92	110	6.5	110	19	
37	a	-117.586339	38.023744	-117.584565	38.023143	1498	16	Q2c	170	7	92	6	0.3	6	18	small scarp - difficult to see
37	b						16	Q2c		47	92	3	0.2	3	14	scarp difficult to see
37	c						16	Q2c		89	92	19	3.8	19	22	
38	a	-117.588226	38.024745	-117.584207	38.023590	1492	16	Q2c	379	42	92		1.86		14	back facing antithetic scarp
38	b						16	Q2c		245	92		1		11	
38	c						16	Q2c		280	92	6	0.96	6	16	
38	d						16	Q2c		313	92		0		17	scarp difficult to see

Appendix C. Topographic profile locations and scarp analysis results

Profile number	Scarp identifier	Northwest Longitude	Northwest Latitude	Southeast Longitude	Southeast Latitude	Elevation (m)	Distance from Southwest (km)[a]	Alluvial surface	Length of topographic profile (m)	Distance from end pt. to scarp (m)[b]	Assumed surface age (ka)[c]	kt (m^2)[d]	Scarp height (m)	Morphologic age (ka)[e]	Scarp angle (degrees)[f]	Comments
39	a	-117.585211	38.026904	-117.584261	38.026312	1497	16	Q2c	107	50	92	6	3.8	6	23	
40	a	-117.585230	38.027002	-117.584247	38.026306	1498	16	Q2c	117	58	92	6	3.6	6	25	
41	a	-117.582956	38.029141	-117.581474	38.028198	1503	16	Q2c	169	41	92	13	2.7	13	16	
42	a	-117.580954	38.029752	-117.579249	38.028750	1508	17	Q2c	188	88	92	26	9	26	26	
43	a	-117.579397	38.030902	-117.578317	38.030026	1513	17	Q2c	137	61	92	3	4.1	3	26	
46	a	-117.578126	38.041602	-117.576176	38.040651	1464	18	Q3b	203	130	17	3	3.2	3	26	
47	a	-117.608164	38.014907	-117.606809	38.014110	1456	14	Q2c	160	81	92	13	7.8	13	25	
48	a	-117.612490	38.011796	-117.611353	38.011488	1455	13	Q2c	108	50	92	32	4	32	14	
49	a	-117.613967	38.008669	-117.612584	38.008231	1457	13	Q3b	132	55	17	6	2	6	19	
50	a	-117.620269	38.008388	-117.618719	38.007964	1442	12	Q2c	145	58	92	3	1.6	3	30	
51	a	-117.620484	38.008004	-117.619458	38.007556	1442	12	Q2c	104	61	92	3	1.8	3	30	
52	a	-117.621180	38.004844	-117.620433	38.004569	1443	12	Q2c	74	45	92	23	2.4	23	17	scarp difficult to see
53	a	-117.621556	38.004637	-117.620025	38.004202	1442	12	Q2c	150	12	92		1		10	scarp difficult to see
53	b						12	Q2c		66	92	13	2.4	13	20	erratic point removed
54	a	-117.624528	37.999003	-117.622375	37.998155	1436	12	Q2c	213	141	92	6	2.2	6	12	
55	a	-117.626286	37.996409	-117.623597	37.995358	1434	11	Q2c	267	162	92	6	2.6	6	18	
56	a	-117.673307	37.967626	-117.671021	37.966526	1436	6	Q2c	243	195	92	6	1.5	6	15	
57	a	-117.635040	37.978564	-117.632099	37.977099	1465	9	Q2c	307	188	92	6	2.1	6	21	
58	a	-117.636784	37.976171	-117.635078	37.974865	1468	9	Q2c	210	55	92	13	4	13	15	
59	a	-117.658661	37.977658	-117.656577	37.973979	1433	8	Q2c	450	290	92	58	4	58	15	
60	a	-117.726669	37.934840	-117.725237	37.932541	1445	0	Q2b	287	138	142	84	2.4	84	6	
61	a	-117.645141	37.976776	-117.643632	37.974668	1456	9	Q2c	273	100	92	71	2.6	71	9	
62	a	-117.670239	37.971100	-117.667322	37.968799	1435	6	Q2c	367	145	92	58	2.5	58	10	modified to take out drainage
63	a	-117.680537	37.957958	-117.679109	37.956827	1437	5	Q2c	187		92					Not a scarp
64	a	-117.691982	37.949287	-117.689498	37.948370	1437	3	Q2c	246		92					Not a scarp
65	a	-117.544906	38.057294	-117.544305	38.056752	1466	21	Q3b	84	57	17	19	3	19	20	
66	a	-117.590617	38.025958	-117.584801	38.022340	1476	16	Q2c	654	300	92		0.42		12	backfacing antithetic scarp
66	b						16	Q2c		504	92		8		20	drainages interfere

Appendix C. Topographic profile locations and scarp analysis results

Profile number	Scarp identifier	Northwest Longitude	Northwest Latitude	Southeast Longitude	Southeast Latitude	Elevation (m)	Distance from Southwest (km)[a]	Alluvial surface	Length of topographic profile (m)	Distance from end pt. to scarp (m)[b]	Assumed surface age (ka)[c]	kt (m^2)[d]	Scarp height (m)	Morphologic age (ka)[e]	Scarp angle (degrees)[f]	Comments
67	a	-117.590992	38.026713	-117.584142	38.023570	1472	16	Q3b	717	202	17		0.6		8	backfacing antithetic scarp
67	b						16	Q3b		427	17		0.6		14	difficult to see scarp
67	c						16	Q3b		516	17	3	0.7	3	20	
67	d						16	Q2c		562	92	19	5	19	25	
67	e						16	Q2c		642	92	6	1	6	17	
68	a	-117.591066	38.025541	-117.586027	38.021651	1474	16	Q2c	623	327	92		0.6		28	backfacing antithetic scarp
68	b						16	Q2c		383	92		2.4		17	backfacing antithetic scarp
68	c						16	Q2c		498	92	142	11.8	142	21	
69	a	-117.539194	38.056383	-117.538571	38.055550	1494	21	Q3b	110	46	17	126	9	126	21	
71	a	-117.587476	38.022495	-117.586269	38.021612	1492	16	Q2c	152	42	92	71	10.2	71	21	
72	a	-117.588236	38.023296	-117.587718	38.022950	1491	16	Q2c	63	29	92		3		20	backfacing antithetic scarp
73	a	-117.588483	38.023763	-117.586043	38.021547	1491	16	Q2c	331	18	92		1.6		12	backfacing antithetic scarp
73	b						16	Q2c		76	92		3.1		20	backfacing antithetic scarp
73	c						16	Q2c		195	92	77	9	77	19	
74	a	-117.588634	38.023750	-117.586125	38.021734	1490	16	Q2c	323	28	92		1.6		8	scarp difficult to see
74	b						16	Q2c		85	92		2.8		14	backfacing antithetic scarp
74	c						16	Q2c		203	92	97	8.8	97	16	
75	a	-117.596972	38.020666	-117.592696	38.017959	1472	15	Q2c	495	75	92	13	5.9	13	25	
75	b						15	Q2c		414	92	13	2	13	10	
76	a	-117.593462	38.018710	-117.592636	38.018033	1489	15	Q2c	105	34	92	19	2.2	19	8	poor elevation control
77	a	-117.576371	38.042116	-117.575434	38.041208	1471	18	Q3b	132	42	17	6	4.2	6	24	
78	a	-117.578824	38.038708	-117.577692	38.037514	1468	17	Q2b	168	63	142	126	15	126	20	
79	a	-117.597569	38.020426	-117.595939	38.019450	1471	15	Q2c	183	98	92	13	5.8	13	24	
82	a	-117.579303	38.046355	-117.575214	38.041467	1431	18	Q3b	662	125	17		0.2		18	
82	b						18	Q3b		403	17	3	1.3	3	18	
82	c						18	Q3b		573	17	3	3.2	3	26	
83	a	-117.579191	38.045855	-117.575438	38.041266	1433	18	Q3b	623	68	17	6	0.5	6	9	
83	b						18	Q3b		130	17		0.64		9	poorly defined scarp
83	c						18	Q3b		323	17	12	0.9	12	14	

Appendix C. Topographic profile locations and scarp analysis results

Profile number	Scarp identifier	Northwest Longitude	Northwest Latitude	Southeast Longitude	Southeast Latitude	Elevation (m)	Distance from Southwest (km)[a]	Alluvial surface	Length of topographic profile (m)	Distance from end pt. to scarp (m)[b]	Assumed surface age (ka)[c]	kt (m^2)[d]	Scarp height (m)	Morphologic age (ka)[e]	Scarp angle (degrees)[f]	Comments
83	d						18	Q3b		541	17	6	4	6	24	
84	a	-117.575629	38.044791	-117.574059	38.042192	1452	18	Q3b	326	114	17	3	1.2	3	23	
84	b						18	Q3b		250	17	6	2.6	6	26	
85	a	-117.573971	38.044770	-117.572822	38.042784	1456	18	Q3b	248	50	17	12	2	12	24	
86	a	-117.578534	38.038902	-117.577499	38.037876	1469	17	Q3b	154	45	17	5	3.4	5	25	
87	a	-117.579217	38.038580	-117.574502	38.035041	1466	17	Q2b	583	84	142	106	17	106	22	
88	a	-117.605791	38.023850	-117.596245	38.017246	1443	15	Q2c	1144	42	92	19	1.2	19	15	
88	b						15	Q2c		504	92	13	4	13	19	
88	c						15	Q2c		1003	92	110	13.6	110	23	
89	a	-117.609761	38.017903	-117.596554	38.016094	1444	14	Q2c	1231	218	92	71	2.8	71	12	
89	b						14	Q2c		520	92	13	6.5	13	23	
89	c						14	Q2c		580	92	13	1.8	13	14	
89	d						14	Q2c		1105	92	123	8	123	22	

[a] Profile 60 is located at the southwest end of the field area - all distances are relative to this profile.
[b] Distance is measured from the lowest point in the scarp profile - generally the north west end.
[c] Assumed surface age is based on resluts of the ^{10}Be model ages for the Q3b, Q2c, and Q2b surfaces
[d] kt values were determined using the Hilley and Arrosmith (2002) matlab code.
[e] Morphologic age is based on a k value of 1.0, typical of arid environments.
[f] Scarp angle is measured from the horizontal as shown in Figure 6.

APPENDIX D

PHOTOGRAPHS OF TCN ^{10}Be SAMPLES

TCN ^{10}Be surface sample LM_0509_01. (a) Photograph of in-place sample. (b) View up-fan. (c) View down fan.

TCN sample LM_0509_02. (a) Photograph of in-place sample. (b) View up-fan. (c) View down fan.

TCN ^{10}Be surface sample LM_0509_04. (a) Photograph of in-place sample. (b) View up-fan. (c) View down fan.

TCN ^{10}Be surface sample LM_0509_05. (a) Photograph of in-place sample. (b) View up-fan. (c) View down fan.

TCN ^{10}Be surface sample LM_0509_06. (a) Photograph of in-place sample. (b) View up-fan. (c) View down fan.

TCN ^{10}Be surface sample LM_0509_07. (a) Photograph of in-place sample. (b) View up-fan. (c) View down fan.

TCN ^{10}Be surface sample LM_0509_08. (a) Photograph of in-place sample. (b) View up-fan. (c) View down fan.

TCN ^{10}Be surface sample LM_0509_10. (a) Photograph of in-place sample. (b) View up-fan. (c) View down fan.

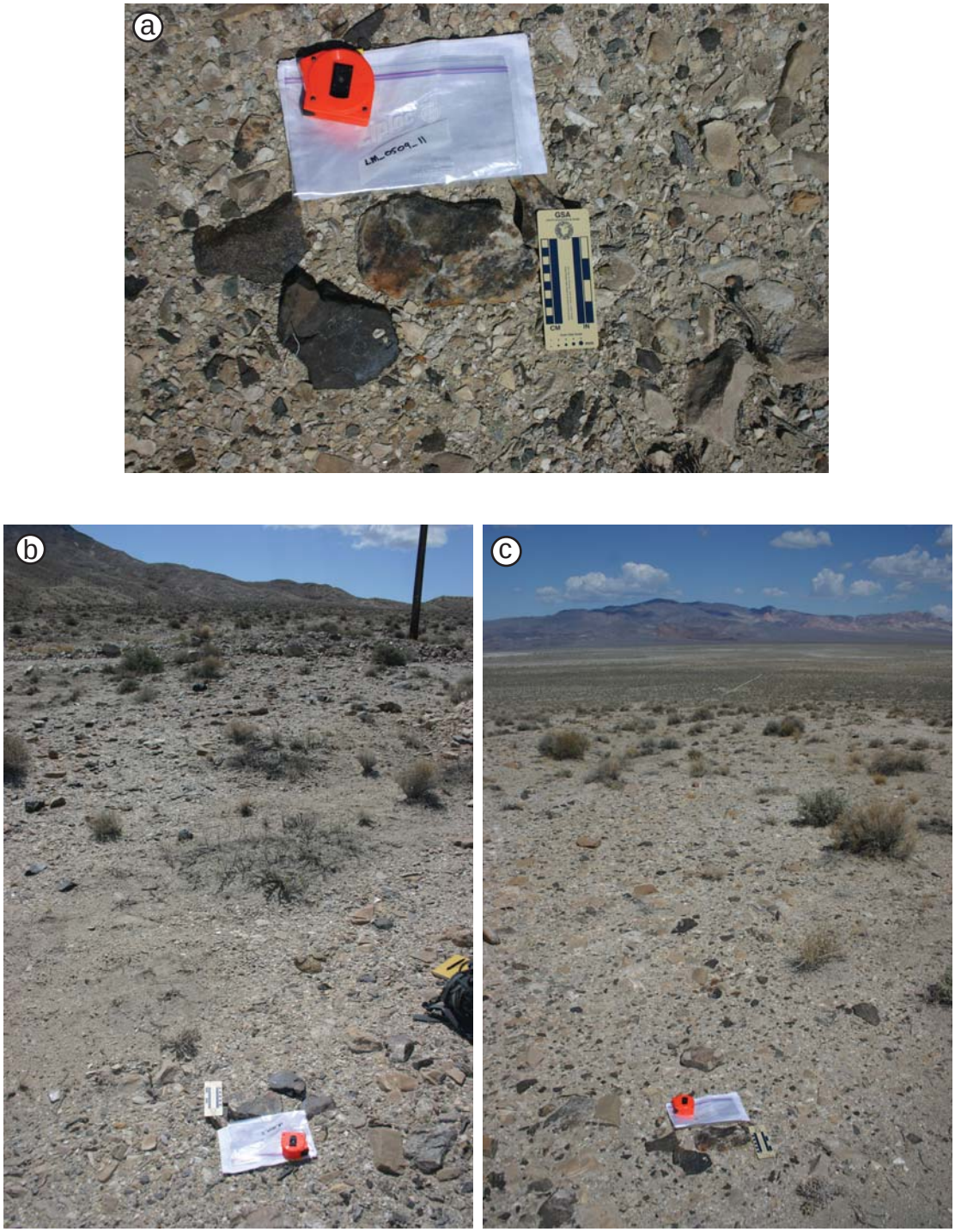

TCN ^{10}Be surface sample LM_0509_11. (a) Photograph of in-place sample. (b) View up-fan. (c) View down fan.

TCN ^{10}Be surface sample LM_0509_12. (a) Photograph of in-place sample. (b) View up-fan. (c) View down fan.

TCN ^{10}Be surface sample LM_0509_13. (a) Photograph of in-place sample. (b) View up-fan. (c) View down fan.

TCN ^{10}Be surface sample LM_0509_14. (a) Photograph of in-place sample. (b) View up-fan. (c) View down fan.

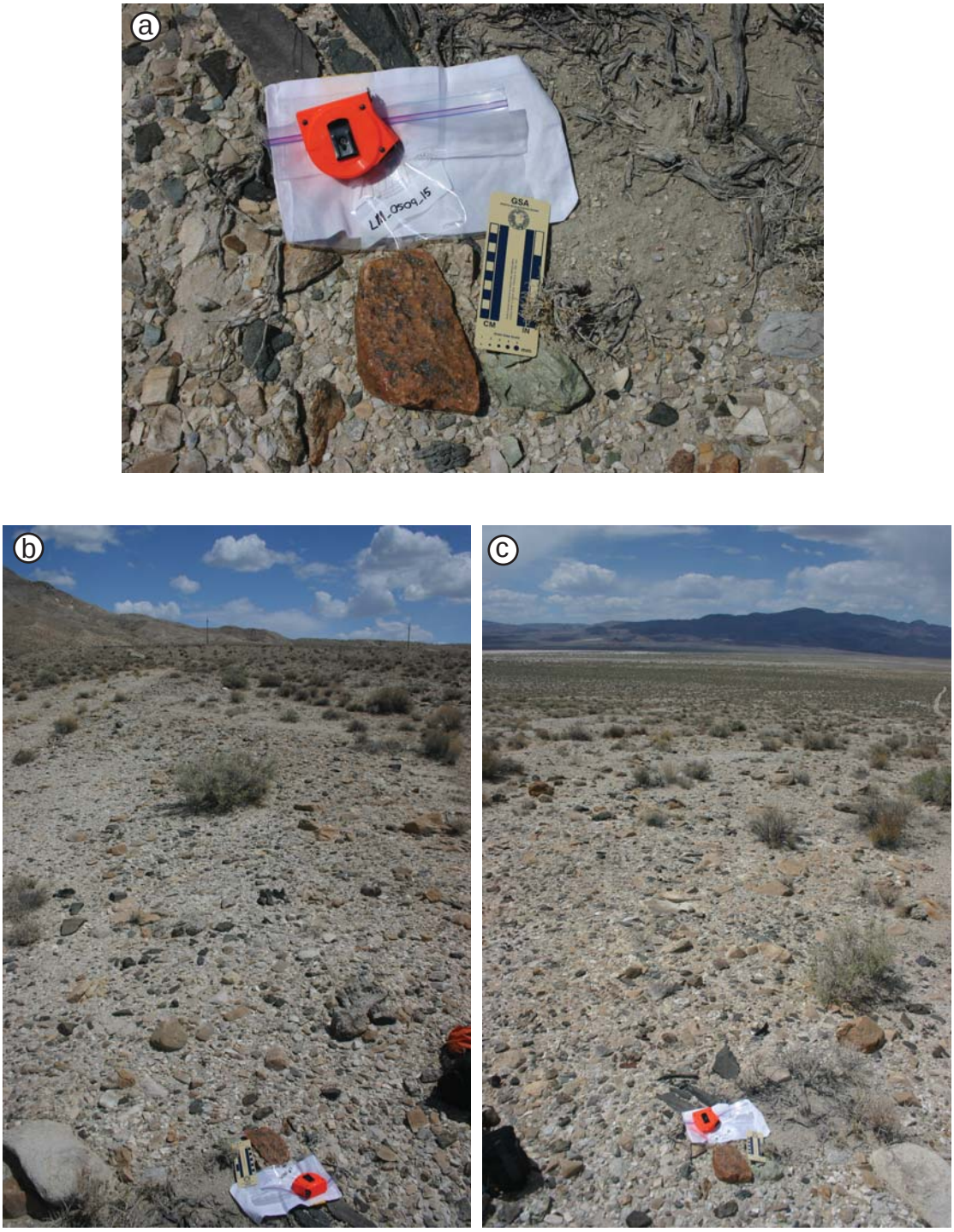

TCN ^{10}Be surface sample LM_0509_15. (a) Photograph of in-place sample. (b) View up-fan. (c) View down fan.

TCN ^{10}Be surface sample LM_0509_17. (a) Photograph of in-place sample. (b) View up-fan. (c) View down fan.

TCN ^{10}Be surface sample LM_0509_18. (a) Photograph of in-place sample. (b) View up-fan. (c) View down fan.

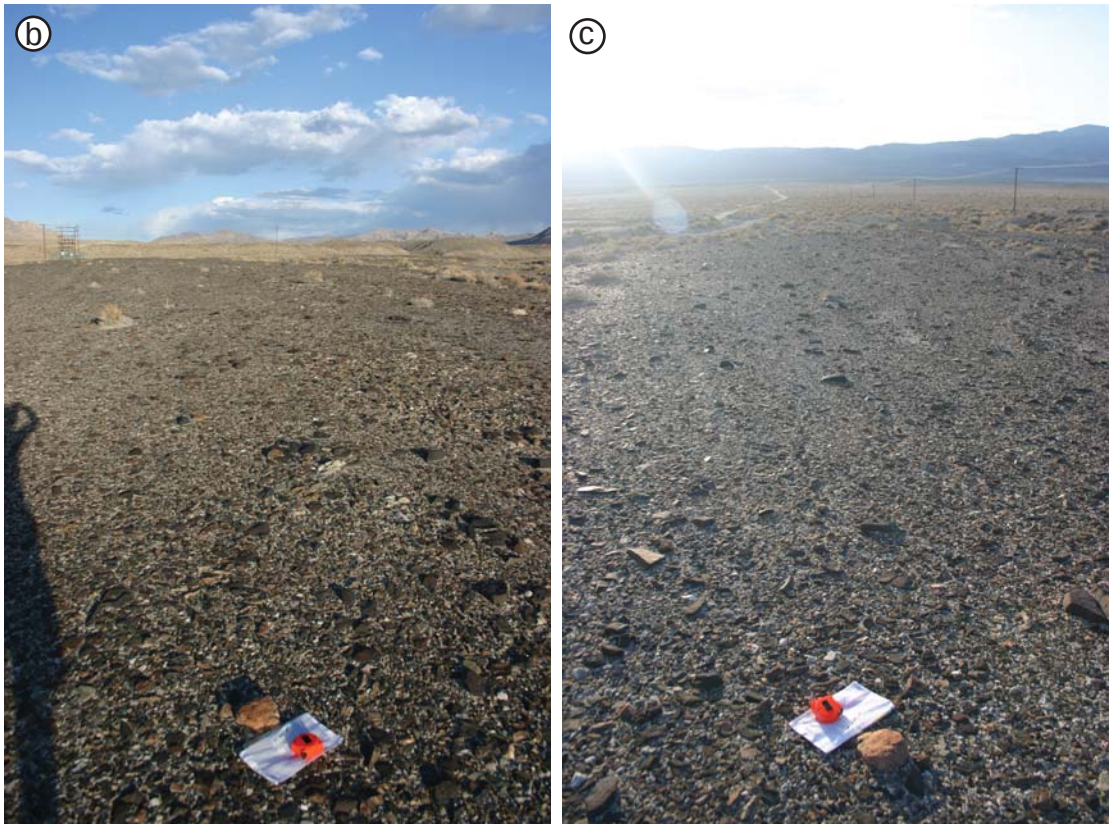

TCN ^{10}Be surface sample LM_0509_19. (a) Photograph of in-place sample. (b) View up-fan. (c) View down fan.

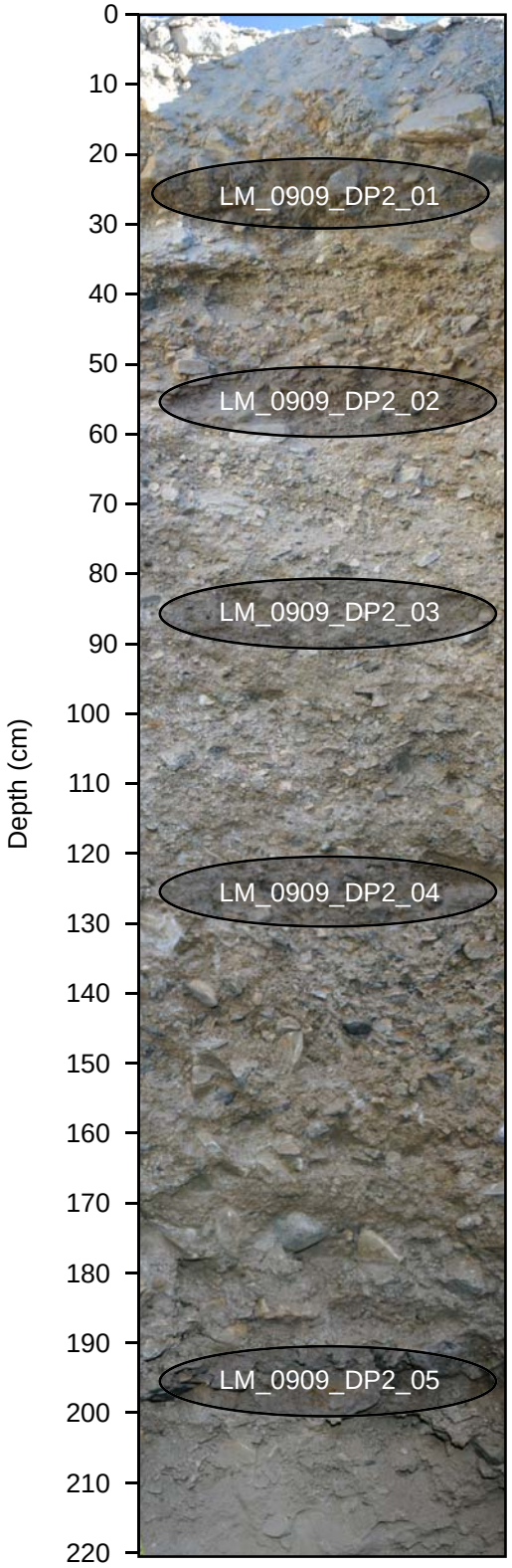

Compilation of merged photographs showing the depth profile from the Q2b alluvial fan. Cosmogenic radionuclide sample intervals are indicated with elipses.

APPENDIX E

COMPLETE TCN RESULTS INCLUDING TIME DEPENDENT AND TIME INDEPENDENT PRODUCTION RATES

Appendix E. Complete TCN results including time dependent and time independent production rates

					Scaling scheme for spallation: Lal(1991)/ Stone(2000)			Desilets and others (2003, 2006)		Dunai (2001)		Lifton and others (2005)		Time-dependent Lal (1991)/Stone (2000)		Time-idependent Lal (1991)/Stone (2000)	
Sample Name	Thickness scaling factor	Shielding factor	Production rate (muons) (atoms/g/yr)	Internal uncertainty (yr)	Exposure age (yr)	External uncertainty (yr)	Production rate (spallation) (atoms/g/yr)	Exposure age (yr)	External Uncertainty (yr)	Exposure age (yr)	External Uncertainty (yr)	Exposure age (yr)	External Uncertainty (yr)	Exposure age (yr)	External Uncertainty (yr)	Exposure age (yr)	External Uncertainty (yr)
Q3b																	
LM-0509-10	0.967	1	0.29	1371	54228	4969	12.89	52510	6414	51666	6282	50625	5214	50271	4475	54228	4969
LM-0509-11	0.959	1	0.29	1661	88097	8001	12.95	85585	10440	84058	10205	82904	8491	82258	7248	88097	8001
LM-0509-12	0.967	1	0.291	428	16717	1520	12.96	17338	2101	17133	2067	16978	1736	16500	1459	16717	1520
LM-0509-13	0.963	1	0.288	377	14724	1338	13.26	15397	1865	15236	1837	15090	1542	14606	1291	14724	1338
LM-0509-14	0.967	1	0.288	838	32718	2986	12.92	32632	3969	32125	3890	31829	3266	31279	2775	32718	2986
LM-0509-15	0.963	1	0.288	477	18737	1703	12.83	19359	2346	19102	2305	18947	1938	18418	1629	18737	1703
LM-0509-17	0.963	1	0.29	736	35411	3190	12.86	35055	4234	34521	4150	34176	3471	33682	2948	35411	3190
LM-0509-18	0.967	1	0.288	395	16967	1532	12.85	17613	2126	17398	2091	17248	1754	16740	1469	16967	1532
Q2c																	
LM-0509-01	0.967	1	0.29	4717	215483	20339	12.93	204306	25779	200776	25200	197012	20873	196676	17955	215483	20339
LM-0509-02	0.967	1	0.29	6850	311112	30075	12.95	295103	38105	289734	37196	284917	30860	284199	26514	311112	30075
LM-0509-04	0.959	1	0.291	6941	255179	24668	13.03	242609	31154	238038	30399	233611	25256	233187	21802	255179	24668
LM-0509-05	0.9731	1	0.293	2920	132171	12230	12.71	125258	15500	123338	15188	121042	12592	120884	10841	132171	12230
LM-0509-06	0.967	1	0.29	4933	219153	20735	12.71	207778	26262	204159	25668	200213	21255	199914	18294	219153	20735
LM-0509-07	0.959	1	0.289	3574	160662	14976	12.73	153004	19069	150374	18647	147544	15454	147091	13281	160662	14976
LM-0509-08	0.959	1	0.29	2298	89506	8280	12.9	87027	10728	85440	10483	84262	8757	83569	7508	89506	8280
LM-0509-19	0.959	1	0.289	2253	95448	8789	12.74	92688	11403	91067	11150	89883	9310	89144	7969	95448	8789

from: http://hess.ess.washington.edu/

REFERENCES

Andrew, J.E., and Walker, J.D., 2009, Reconstructing late Cenozoic deformation in central Panamint Valley, California: Evolution of slip partitioning in the Walker Lane: Geosphere, v. 5, p. 172-198.

Anderson, R.S., Repka, J.L., and Dick, G.S., 1996, Explicit treatment of inheritance in dating depositional surfaces using in situ 10Be and 26Al: Geology, v. 24, p. 47–51, doi: 10.1130/0091–7613(1996)024<0047:ETOIID>2.3.CO;2.

Armstrong, P., Perez, R., Owen, L.A., and Finkel, R.C. (2010) Timing and controls on late Quaternary landscape development along the eastern Sierra el Mayor, northern Baja California, Mexico. Geomorphology 114, 415-430.

Arrowsmith, J R., Rhodes, D. D., and Pollard, D. D., 1998, Morphologic dating of scarps formed by repeated slip events along the San Andreas Fault, Carrizo Plain, California, Journal of Geophysical Research, 103, B5, 10,141–10,160.

Atwater, T., 1970, Implications of plate tectonics for the Cenozoic evolution of western North America: Geological Society of America Bulletin, v. 81p. 3513-3536.

Atwater, Tanya, and P. Molnar, 1973, Relative motion of the Pacific and North American plates deduced from sea-floor spreading in the Atlantic, Indian and South Pacific Oceans. R. L. Kovach and A. Nur, eds., Proc. of the Conf. on Tectonic Problems of the San Andreas Fault, Geological Sciences, v. XIII, Stanford Univ., p. 136-148. •Reprinted in U.C.S.D., Scripps Inst. Oceanography., Contributions, Vol. 44, Part 2, p. 1362-1374.

Atwater, T., and Stock, J.M., 1998, Pacific–North America plate tectonics of the Neogene southwestern United States: An update: International Geology Review, v. 40p. 375-402.

Balco, G., Stone, J.O., Lifton, N.A., and Dunai, T.J., 2008, A complete and easily accessible means of calculating surface exposure ages or erosion rates from 10Be and 26Al measurements: Quaternary Geochronology, v. 3, p. 174-195.

Bartley, J.M., Glazner, A.F., Coleman, D.S., Kylander-Clark, A.R.C., Mapes, R., and Friedrich, A.M., 2008, Large Laramide dextral offset across Owens Valley, California, and its possible relation to tectonic unroofing of the southern Sierra Nevada, in Till, A.B., Roeske, S.M., Foster, D.A. and Sample, J.C., eds., Exhumation Processes along Major Continental Strike-slip Fault Systems: Geological Society of America Special Paper 434, p. 129–148, doi: 10.1130/2007.2343(07).

Bennett, R.A., Wernicke, B.P., Niemi, N.A., Friedrich, A.M., and Davis, J.L., 2003, Contemporary strain rates in the northern Basin and Range province from GPS data: Tectonics, v. 22, doi: 10.1029/2001TC001355.

Bierman, P.R., Caffee, M.W., Davis, P.T., Marsella, K., Pavich, M., Colgan, P., Mickelson, D., & Larsen, J., 2002. Rates and timing of earth surface processes from in-situ-produced cosmogenic Be-10, in Grew, E.S., ed., Beryllium: Mineralogy, Petrology, and Geochemistry, Reviews in Mineralogy and Geochemistry, 50, 148-205.

Bird, P., 2007, Uncertainties in long-term geologic offset rates of faults; General principles illustrated with data from California and other western states: Geosphere, v. 3, p. 577–595.

Bucknam, R.C., and Anderson, R.E., 1979, Estimation of fault scarp ages from a scarp height slope angle relationship: Geology, v. 7, p. 11-14.

Burchfiel, B.C., 1979, Geologic history of the central Western United States: Report - Nevada Bureau of Mines and Geology, , no. 33, p. 1-11.

Bull, W.B., 1968. Alluvial fans. Journal of Geological Education 16, 101–106.

Bull, W.B. 1991. Geomorphic Responses to Climatic Change, 326 pp., Oxford Univ. Press, New York.

Cashman, P. H., and Fontaine, S.A., 2000, Strain partitioning in the northern Walker Lane, western Nevada and northeastern California: Tectonophysics, v. 326, p. 111 – 130.

dePolo, C.M., 2008, Quaternary faults in Nevada: Nevada Bureau of Mines and Geology Map 167, scale 1:1,000,000.

Desilets, D., and Zreda, M., 2003. Spatial and temporal distribution of secondary cosmic-ray nucleon intensities and applications to in-situ cosmogenic dating: Earth and Planetary Science Letters, v. 206, p. 21–42.

Desilets, D., Zreda, M., and Prabu, T., 2006. Extended scaling factors for in situ cosmogenic nuclides: New measurements at low latitude. Earth and Planetary Science Letters, v. 246, p. 265–276.

Dixon, T. H., Robaudo, S., Lee, J., and Reheis, M.C., 1995, Constraints on present-day Basin and Range deformation from space geodesy: Tectonics, v. 14, p. 755–772.

Dixon, T.H., Miller, M., Farina, F., Wang, H., and Johnson, D., 2000, Present-day motion of the Sierra Nevada block and some tectonic implications for the basin and Range province, North American Cordillera: Tectonics, v. 19, p. 1-24.

Dixon, T.H., Norabuena, E., and Hotaling, L., 2003, Paleoseismology and Global Positioning System: Earthquake-cycle effects and geodetic versus geologic fault slip rates in the Eastern California shear zone: Geology, v. 31, 55-58.

Dokka, R.K., 1983. Displacements on late Cenozoic strike-slip faults of the central Mojave Desert, California: Geology, v. 11, p. 305–308.

Dokka, R.K., and Travis, C.J., 1990, Late Cenozoic strike-slip faulting in the Mojave Desert, California: Tectonics, v. 9, p. 311–340.

Dokka, R.K., and Travis, C.J., 1990, Role of the eastern California shear zone in accommodating Pacific-North American plate motion: Geophysical Research Letters, v. 17, p. 1323-1326.

Dohrenwend, J.C., Schell, B.A., McKittrick, M.A., and Moring, B.C. , 1992, Reconnaissance

photogeologic map of young faults in the Goldfield 1º x 2º quadrangle, Nevada and California, U.S. Geological Survey Miscellaneous Field Studies Map MF-2183, scale 1:250,000.

Dunai, T., 2001. Influence of secular variation of the magnetic field on production rates of in situ produced cosmogenic nuclides: Earth and Planetary Science Letters, v. 193, p. 197–212.

Faulds, J.E., Henry, C.D., and Heinz, N.H., 2005, Kinematics of the northern Walker Lane: An incipient transform fault along the Pacific-North America plate boundary: Geology, v. 33, p. 505-508.

Frankel, K.L., Brantley, K.S., Dolan, J.F., Finkel, R.C., Klinger, R.E., Knott, J.R., Machette, M.N., Owen, L.A., Phillips, F.M., Slate, J.L., and Wernicke, B.P., 2007a, Cosmogenic Be-10 and Cl-36 geochronology of offset alluvial fans along the northern Death Valley fault zone: Implications for transient strain in the eastern California shear zone: Journal of Geophysical Research- Solid Earth, v. 112, doi: 10.1029/2006JB004350.

Frankel, K.L., Dolan, J.F., Finkel, R.F., Owen, L.A., and Hoeft, J.S., 2007b, Spatial variations in slip rates along the Death Valley-Fish Lake Valley fault system determined from LiDAR topographic data and cosmogenic 10Be geochronology: Geophysical Research Letters, v. 34, doi: 1029/2007GL030549.

Frankel, K.L., and 17 others, 2008, Active tectonics of the eastern California shear zone, in Duebendorfer, E.M., and E.I. Smith, eds., Field Guide to Plutons, Volcanoes, Reefs, Dinosaurs, and Possible Glaciation in Selected Areas of Arizona, California, and Nevada: Geological Society of America Field Guide, v. 11, p. 43-81, doi:10.1130/2008.fld011(03).

Frankel, K.L., and Dolan, J.F., 2007, Characterizing arid region alluvial fan surface roughness with airborne laser swath mapping digital topographic data: Journal of Geophysical Research, v. 112, no. F2.

Frankel, K.L., Owen, L.A., Dolan, J.F., Ganev, P., and Finkel, R.C., in review, Spatial and temporal constancy of seismic strain release along an evolving segment of the Pacific-North America plate boundary: Earth and Planetary Science Letters.

Ganev, P.N., Dolan, J.F., Frankel, K.L., and Finkel, R.C., 2010, Rates of extension along the Fish Lake Valley fault and transtensional deformation in the eastern California shear zone-Walker Lane: Lithosphere, v. 2, p. 33-49, doi:10.1130/L51.1.

Gosse, J.C., and Phillips, F.M., 2001, Terrestrial in situ cosmogenic nuclides: theory and application: Quaternary Scientific Review, v. 20, p. 1475-1560.

Hancock, G.S., Anderson, G.S., Chadwick, O.A., and Finkel, R.C., 1999, Dating fluvial terraces with 10Be and 26Al profiles: application to the Wind River, Wyoming: Geomorphology, v. 27, p. 41-60.

Hanks, T.C., Bucknam, R.C., Lajoie, K.R., and Wallace, R.E., 1984, Modification of wave-cut and fault controlled landforms: Journal of Geophysical Research, v. 89, p. 5771-5790.

Hearn, E.H., and Humphreys, E.D., 1998, Kinematics of the southern Walker Lane belt and motion of the Sierra Nevada block, California: Journal of Geophysical Research, v. 103, p. 27,033-27,049, doi: 10.1029/98JB01390.

Hilley, G.E., Arrowsmith, J.R., 2002, Diffusion Scarp Dater, Matlab code.

Humphreys, E.D., and Weldon, R.J., 1994, Deformation across the western United States: A local estimate of Pacific-North America transform deformation: Journal of Geophysical Research, v. 99, p. 19,975-20,010.

Heisinger, B., Lal, D., Jull, A.J.T., Kubik, P., Ivy-Ochs, S., Knie, K., and Nolte, E., 2002a, Production of selected cosmogenic radionuclides by muons; 2, Capture of negative muons: Earth and Planetary Science Letters, v. 200, no. 3-4, p. 357-369.

Heisinger, B., Lal, D., Jull, A.J.T., Kubik, P., Ivy-Ochs, S., Neumaier, S., Knie, K., Lazarev, V., and Nolte, E., 2002b, Production of selected cosmogenic radionuclides by muons; 1, Fast muons: Earth and Planetary Science Letters, v. 200, no. 3-4, p. 345-355.

Kirby, E., Anandakrishnan, S., Phillips, F., and Marrero, S., 2008, Millennial scale slip rate along the Owens Valley fault, eastern California: Geophysical Research Letters, v. 35, L01304, doi:10.1029/2007GL031970.

Kirby, E., Burbank, D.W., Reheis, M., and Phillips, F., 2006, Temporal variations in slip rate of the White Mountain Fault Zone, Eastern California: Earth and Planetary Science Letters, v. 248, p. 153-170, doi:10.1016/j.epsl.2006.05.026.

Kirsch, S.A., 1971, Chaos structure and turtleback dome, Mineral Ridge, Esmeralda County, Nevada: Geological Society of America Bulletin, v. 82, p. 3169–3176, doi: 10.1130/0016-7606(1971)82[3169:CSATDM] 2.0.CO;2.

Kohl, C.P., and Nishiizumi, K., 1992, Chemical isolation of quartz for measurement of in-situ-produced cosmogenic nuclides: Geochimica et Cosmochimica Acta, v. 56, p. 3583-3587.

Kylander-Clark, A.R.C., Coleman, D.S., Glazner, A.F., and Bartley, J.M., 2005, Evidence for 65 km of dextral slip across Owens Valley, California since 83 Ma: Geological Society of America Bulletin, v. 117, p. 962–968, doi:10.1130/B25624.1.

Lal, D., 1991, Cosmic ray labeling of erosion surfaces: In situ nuclide production rates and erosion models: Earth and Planetary Science Letters, v. 104, p. 424-439.

Le, K., Lee, J., Owen, L.A., and Finkel, R., 2006, Late Quaternary slip rates along the Sierra Nevada frontal fault zone, California: Slip partitioning across the western margin of the eastern California shear zone- Basin and Range province: Geological Society of America Bulletin, doi: 10.1130/B25960.1.

Lee, J., Spencer, J., and Owen, L., 2001, Holocene slip rates along the Owens Valley fault, California: Implications for the recent evolution of the eastern California shear zone: Geology, v. 29, p. 819-822.

Lee, J., Stockli, D., Schroeder, J., Tincher, C., Bradley, D., Owen, L., Gosse, J., Finkel, R., and Garwood, J., 2006, Fault slip transfer in the Eastern California Shear Zone–Walker Lane Belt: Geological Society of America Penrose Conference Field Trip Guide, v. 26, doi:10.1130/2006.FSTITE.PFG.

Lee, J., Garwood, J., Stockli, D.E., and Gosse, J., 2009a, Quaternary faulting in Queen Valley,California-Nevada: Implications for kinematics of fault-slip transfer in the eastern California shear zone-Walker Lane belt: Geological Society of America Bulletin, doi: 10.1130/B26352.1.

Lee, J., Stockli, D.F., Owen, L.A., Finkel, R.C., and Kislitsyn, R., 2009b, Exhumation of the Inyo Mountains, California: Implications for the timing of extension along the western boundary of the Basin and Range Province and distribution of dextral fault slip rates across the eastern California shear zone: Tectonics, v. 28, doi:10.1029/2008TC002295.

Lifton, N., Bieber, J., Clem, J., Duldig, M., Evenson, P., Humble, J., Pyle, R., 2005, Addressing solar modulation and long-term uncertainties in scaling secondary cosmic rays for in situ cosmogenic nuclide applications. Earth and Planetary Science Letters, v. 239, p. 140-161.

Machette, M.N., Slate, J.L., and Phillips, F.M., 2008, Terrestrial cosmogenic-nuclide dating of alluvial fans in Death Valley, California: U.S. Geological Survey Professional Paper 1755, 44 p.

McClusky, S.C., Bjornstad, S.C., Hager, B.H., King, R.W., Meade, B.J., Miller, M.M., Monastero, F.C., and Souter, B.J., 2001, Present day kinematics of the Eastern California Shear Zone from a geodetically constrained block model: Geophysical Research Letters, v. 28, p. 3369-3372.

McGill, S.F., Wells, S.G., Fortner, S.K., Kuzma, H.A., and McGill, J.D., 2009, Slip rate of the western Garlock fault, at Clark Wash, near Lone Tree Canyon, Mojave Desert, California, Geological Society of America Bulletin, v. 121, doi:10.1130/B26123.1.

Miller, M.M., Johnson, D.J., Dixon, T.H., and Dokka, R.K., 2001, Refined kinematics of the eastern California shear zone from GPS observations, 1993-1994: Journal of Geophysical Research, v. 106, p. 2245-2263.

Nielsen, R.L., 1965, Right-lateral strike-slip faulting in the Walker Lane, west-central Nevada: Geological Society of America Bulletin, v. 76, p. 1301-1308.

Nishiizumi, K., Imamura, M., Caffee, M.W., Southon, J.R., Finkel, R.C., and McAninch, J., 2007, Absolute calibration of 10Be AMS standards: Nuclear Instruments and Methods in Physics Research B, v. 258, p. 403-413.

Oldow, J.S., Aiken, C.L.V., Hare, J.L., Ferguson, J.F., and Hardyman, R.F., 2001, Active displacement transfer and differential block motion within the central Walker Lane, western Great Basin: Geology, v. 29, p. 19-22.

Oldow, J.S., Kohler, G., and Donelick, R.A., 1994, Late Cenozoic extensional transfer in the Walker Lane strike-slip belt, Nevada: Geology, v. 22, p. 637-640.

Oldow, J.S., 2003, Active transtensional boundary zone between the western Great Basin and Sierra Nevada block, western U.S. Cordillera: Geology, v. 31, p. 1033-1036.

Oldow, J.S., Aiken, C.L.V., Ferguson, J.F., Hare, J.L., and Hardyman, R.F., 2001, Active displacement transfer and differential motion between tectonic blocks with the central Walker Lane, western Great Basin: Geology, v. 29, p. 19-22.

Oldow, J.S., Bally, A.W., Ave Lallemant, H.G., and Leeman, W.P., 1989, Phanerozoic evolution of the North American Cordillera (United States and Canada), in Bally, A.W., and A.R. Palmer, eds., The Geology of North America: An Overview, Geological Society of America, Geology of North America, v. A, p. 139-232.

Oldow, J.S., Elias, E.A., Ferranti, L., McClelland, W.C., and McIntosh, W.C., 2009, Late Miocene to Pliocene synextensional deposition in fault-bounded basins within the upper plate of the western Silver Peak–Lone Mountain extensional complex, west-central Nevada, in Oldow, J.S., and Cashman, P.H., eds., Late Cenozoic Structure and Evolution of the Great Basin–Sierra Nevada Transition: Geological Society of America Special Paper 447, p. 275–312, doi: 10.1130/2009.2447(14).

Oldow, J.S., Geissman, J.W., and Stockli, D.F., 2008, Evolution and strain reorganization within late Neogene structural stepovers linking the central Walker Lane and northern Eastern California shear zone, western Great Basin: International Geology Review, v. 50, p. 1–21, doi: 10.2747/0020-6814.50.3.

Oskin, M., and A. Iriondo, 2004, Large-magnitude transient strain accumulation on the Blackwater fault, eastern California shear zone, Geology, 32, 313– 316.

Oskin, M., Perg, L., Blumentritt, D., Mukhopadhyay, S., and Iriondo, A., 2007, Slip rate of the Calico fault: Implications for geologic versus geodetic rate discrepancy in the eastern California shear zone: Journal of Geophysical Research, v. 112, doi:10.1029/2006JB004451.

Oskin, M., Perg, L., Shelef, E., Strane, M., Gurney, E., Singer, B., and Zhang, X., 2008, Elevated shear zone loading rate during an earthquake cluster in eastern California: Geology, v. 36, n. 6, p. 507-510, doi: 10.1130/G24814A.1.

Owen, L.A., Frankel, K.L., Knott, J.R., Reynhout, S., Finkel, R.C., Dolan, J.F., and Lee, J., in review, Beryllium-10 terrestrial cosmogenic nuclide surface exposure dating of Quaternary landforms in Death Valley: Geomorphology.

Peltzer, G., Crampe, F., Hensley, S., and Rosen, P., 2001, Transient strain accumulation and fault interaction in the eastern California shear zone: Geology, v. 29, p. 975–978, doi: 10.1130/0091-7613(2001)029<0975: TSAAFI>2.0.CO;2.

Petronis, M.S., Geissman, J.W., Oldow, J.S., and McIntosh, W.C., 2002, Paleomagnetic and 40Ar/39Ar geochronologic data bearing on the structural evolution of the Silver Peak extensional complex, west-central Nevada: Geological Society of America Bulletin, v. 114, p. 1108-1130.

Petronis, M.S., Geissman, J.W., Oldow, J.S., and McIntosh, W.C., 2007, Tectonism of the southern Silver Peak Range: Paleomagnetic and geochronologic data bearing on the Neogene development of a regional extensional complex, central Walker Lane, Nevada: Geological Society of America Special Paper 434, p. 81–106, doi: 10.1130/2007.2434(05).

Petronis, M.S., Geissman, J.W., Oldow, J.S., and McIntosh, W.C., 2009, Late Miocene to Pliocene vertical-axis rotation attending development of the Silver Peak–Lone Mountain displacement transfer zone, west-central Nevada, in Oldow, J.S., and Cashman, P.H., eds., Late Cenozoic Structure and Evolution of the Great Basin–Sierra Nevada Transition, Geological Society of America Special Paper 447, p. 215–253, doi: 10.1130/2009.2447(12).

Pigati, J.S., Lifton, N.A., 2004. Geomagnetic effects on time-integrated cosmogenic nuclide production with emphasis on in situ 14C and 10Be. Earth and Planetary Science Letters 226, 193–205.

Reheis, M.C. and Sawyer, T.L., 1997, Late Cenozoic history and slip rates of the Fish Lake Valley, Emigrant Peak, and Deep Springs fault zones, Nevada and California: Geological Society of America Bulletin, v. 109, p. 280-299.

Ritter, J.B., Miller, J.R., Enzel, Y., Howes, S.D., Nadon, G., Grubb, M.D., Hoover, K.A., Olsen, T., Reneau, S.L., Sack, D., Summa, C.L., Taylor, I., Touysinhthiphonexay, K.C.N., Yodis, E.G., Schneider, N.P., et al., 1993, Quaternary evolution of Cedar Creek alluvial fan, Montana: Geomorphology, v. 8, no. 4, p. 287-304.

Savage, J.C., Gan, W., and Svarc, J.L., 2001, Strain accumulation and rotation in the eastern California shear zone: Journal of Geophysical Research, v. 106(B10), p. 21,995-22,007.

Sauber, J., Thatcher, W., Solomon, S.C., and Lisowski, M., 1994, Geodetic slip rate for the eastern California shear zone and the recurrence time of Mojave Desert earthquakes: Nature, v. 367, p. 264–266, doi: 10.1038/367264a0

Snyder, W.S., Dickinson, W.R., and Silberman, M.L., 1976, Tectonic implications of space-time patterns of Cenozoic magmatism in the western United States: Earth and Planetary Science Letters, v. 32, no. 1, p. 91-106.

Sohn, M.F., Mahan, S.A., Knott, J.R., Bowman, D.D., 2007. Luminescence ages for alluvial-fan deposits in Southern Death Valley: Implications for climate-driven sedimentation along a tectonically active mountain front. Quaternary International 166, 49-60.

Staiger, J., Gosse, J., Toracinta, R., Oglesby, B., Fastook, J., Johnson, J.V., 2007. Atmospheric scaling of cosmogenic nuclide production: climate effect. Journal of Geophysical Research 112, B02205, doi:10.1029/2005JB003811.

Stewart, J.H., 1988, Tectonics of the Walker Lane belt, western Great Basin: Mesozoic and Cenozoic deformation in a zone of shear, in Ernst, W.G., ed., Metamorphism and crustal evolution of the western United States, Rubey v. 7, p. 683-713, Prentice Hall, Englewood Cliffs.

Stewart, J.H., 1985, East-trending dextral faults in the western Great Basin; an explanation for anomalous trends of pre-Cenozoic strata and Cenozoic faults: Tectonics, v. 4, p. 547-564.

Stockli, D.F., Dumitru, T.A., McWilliams, M.O., and Farley, K.A., 2003, Cenozoic tectonic evolution of the White Mountains, California and Nevada: Geological Society of America Bulletin, v. 115, p. 788-816, doi:10.1130/00167606(2003)115<0788:CTEOTW>2.0.CO;2.

Stone, J.O., 2000, Air pressure and cosmogenic isotope production: Journal of Geophysical Research, v. 105, p. 23,753-23,759.

Twiss, R.J. and Moores, E.M., 2007, Structural Geology, 2nd Edition, W.H. Freeman and Company, New York

Walker, J.D., Kirby, E., and Andrew, J.E., 2005, Strain transfer and partitioning between the Panamint Valley, Searles Valley, and Ash Hill fault zones, California: Geosphere, v. 1, p. 111-118.

Wallace, R.E., 1977, Profiles and ages of young fault scarps, North-central Nevada: Geological Society of America Bulletin, v. 88, no. 9, p. 1267-1281.

Wesnousky, S.G., 2005a, Active Faulting in the Walker Lane: Tectonics, v. 24, doi:10.1029/2004TC001645.

Wesnousky, S.G., 2005b, The San Andreas and Walker Lane fault systems, western North America: transpression, transtension, cumulative slip and the structural evolution of a major transform plate boundary: Journal of Structural Geology, v. 27, p. 1505-1512.

Zechar, J.D., and Frankel, K.L., 2009, Incorporating and reporting uncertainties in fault slip rates: Journal of Geophysical Research - Solid Earth, v. 114, doi:10.1029/2009JB006325.